energies

MDPI

Review

Recent Progress on Emerging Applications of Hydrochar

Md Tahmid Islam [1], Al Ibtida Sultana [1], Cadianne Chambers [1], Swarna Saha [1], Nepu Saha [2], Kawnish Kirtania [3] and M. Toufiq Reza [1,*]

[1] Department of Biomedical and Chemical Engineering and Sciences, Florida Institute of Technology, 150 W University Boulevard, Melbourne, FL 32901, USA
[2] Energy and Environmental Science & Technology, Idaho National Laboratory, 750 MK Simpson Boulevard, Idaho Falls, ID 83402, USA
[3] Department of Chemical Engineering, Bangladesh University of Engineering and Technology, Dhaka 1000, Bangladesh
* Correspondence: treza@fit.edu; Tel.: +1-321-674-8578

Abstract: Hydrothermal carbonization (HTC) is a prominent thermochemical technology that can convert high-moisture waste into a valuable product (called hydrochar) at a relatively mild treatment condition (180–260 °C and 2–10 MPa). With rapidly growing research on HTC and hydrochar in recent years, review articles addressing the current and future direction of this research are scarce. Hence, this article aims to review various emerging applications of hydrochars, e.g., from solid fuel to soil amendment, from electron storage to hydrogen storage, from dye adsorption, toxin adsorption, heavy metal adsorption to nutrient recovery, and from carbon capture to carbon sequestration, etc. This article further provides an insight in the hydrochar's working mechanism for various applications and how the applications can be improved through chemical modification of the hydrochar. Finally, new perspectives with appropriate recommendations have been made to further unveil potential applications and its improvement through hydrochar and its modified version.

Keywords: hydrothermal carbonization; hydrochar; biomass; fuel; gas adsorption; water purification

Citation: Islam, M.T.; Sultana, A.I.; Chambers, C.; Saha, S.; Saha, N.; Kirtania, K.; Reza, M.T. Recent Progress on Emerging Applications of Hydrochar. *Energies* **2022**, *15*, 9340. https://doi.org/10.3390/en15249340

Academic Editor: Albert Ratner

Received: 25 October 2022
Accepted: 3 December 2022
Published: 9 December 2022

1. Introduction

The United States produces >12% of the world's wastes alone although it is home to only 4% of world's total population [1]. These wastes contain significant carbon material, which has become the center of active research since conversion of such waste carbon material can synthesize value-added product [2,3]. Of several established conversion technologies, hydrothermal carbonization (HTC) has become the center of interest because it can transform wet feedstock (as high as 70–90% moisture) without pre-drying/pretreatment and the solid hydrochar yield can be as high as 35–65%, while the rest of them are liquid and gas [4,5]. As evident in Figure 1, the research on HTC and hydrochar has increased by more than 2–3 times in 2021 since 2017. Hence, it has become equally important to understand the recent progress on emerging scenarios of HTC and hydrochars.

The HTC process employs elevated subcritical temperature (180–350 °C) and autogenous pressure [6,7], which disintegrate organic wastes [6,8]. As the temperature increases in HTC, the biopolymer bonds break [9,10] while the water molecules easily penetrate through the porous structure of the solid and decompose the biomass by dissolution and pyrolysis reactions [6,7,11]. Therefore, the modification of solid waste through HTC and varying HTC condition synthesizes hydrochar equipped with the number of useful applications, e.g., solid fuel [12,13], hydrogen energy storage [14,15], water purification [16,17], soil amendment [18], toxin adsorption [19], electrochemical device [20], catalyst support [21], and carbon sequestration [22], etc. Although hydrochars have been attempted as higher-value applications such as water purification, carbon capture, energy storage, and electron storage, concern remain about their efficacy since they do not consist of the high porosity

or surface area that are important for higher-value applications [23–28]. Chemical modification of hydrochars has been revealed as valuable since it could overcome the structural limitation and enhance the efficacy of various applications.

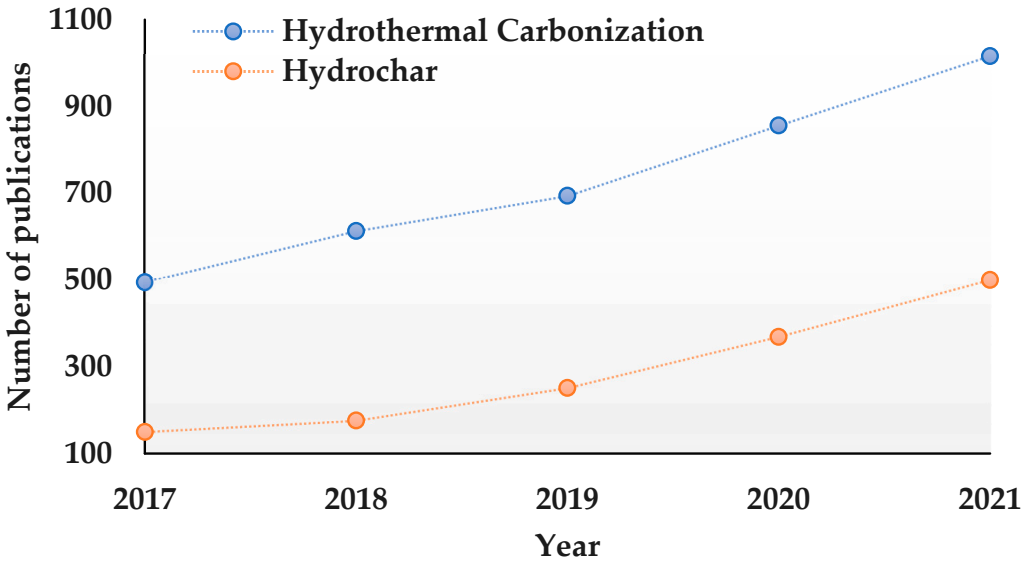

Figure 1. Number of publications including HTC and hydrochar on the title in last five years [29].

This review article discusses the current applications of hydrochar and modified hydrochar, working mechanisms, and the impact of varying HTC conditions and hydrochar modification conditions on the efficiency. This review gives a broad perspective on HTC, hydrochar, and modified hydrochar and narrows down to a fundamental understanding of their application. Finally, the emerging applications to date have been presented which would provide an important future direction of hydrochar study.

2. Role of Hydrochar for Multipurpose Applications

2.1. Solid Fuel and Combustion Properties of Hydrochar

Table 1 shows the fuel and combustion properties of select waste biomass-derived hydrochars at different HTC conditions. The HTC conditions are varied from 180–300 °C, 5 min–24 h, and 1:5–1:25 (solid: water *w*/*w* ratio) to synthesize energy-dense fuel [6,30,31]. The 0.5 h reaction time is reported as sufficient since the greatest extent of HTC reaction occurs within that specific period of time [32]. The elemental hydrogen-to-carbon ratio (H/C) and elemental oxygen-to-carbon ratio (O/C) of raw feedstocks vary between 0.12–2.11 and 0.73–0.88 for lignocellulose, and 0.12–2.10 and 0.38–0.90 for non-lignocellulose, respectively. It is observed that the H/C and O/C ratios for hydrochars vary between 0.80–1.58 and 0.19–0.75 for lignocellulose, 0.94–1.77 and 0.15–0.81 for non-lignocellulose, and 0.82–1.54 and 0.12–0.72 for combined lignocellulose:non-lignocellulose, respectively. The HTC decreases the H/C and O/C ratios for both lignocellulosic and non-lignocellulosic hydrochars; however, the reduction is more prominent for the combined lignocellulosic:non-lignocellulosic hydrochars. This is expected since HTC for a single feedstock creates an acidic environment through dehydration (formation of H_2O) and decarboxylation reactions (formation of CO_2 or carbonyl or carboxylic acids) [33–36] and thereby, the H/C and O/C ratios drop. However, in case of combined lignocellulose:non-lignocellulose HTC (also known as Co-HTC), one feedstock can act as a nucleation site for another, as found by Saba et al. [37] for coal–miscanthus blend HTC, which further augments condensation and polymerization of carbon-dense organics from process liquid to the hydrochar's surface [36,38]. Xu et al. [39], on the other hand, showed that in the case of Co-HTC of polyvynyl chloride (PVC) and cotton textile waste, the surface –OH and C=O groups of hydrochar propagate C-Cl bonds and promote HTC through dehydration/aromatization

reactions. In response, the solid hydrochar shows relatively higher carbon composition than hydrogen or oxygen. It was also observed that increasing HTC temperature increases the O/C and H/C ratios more, since the dehydration and decarboxylation reactions improve at a higher extent [6]. The lower H/C ratio also indicates higher aromatic compounds in hydrochar [40]. As suggested by the Van Krevelen diagram [41,42], the fuel quality of any solid is better if the fuel consists of lower H/C and O/C ratios. For example, walnut shell showed the lowest H/C ratio while tobacco stalk showed the lowest O/C ratio suggesting higher dehydration/demethylation reactions and decarboxylation/dehydration reactions, respectively [37]. In case of non-lignocellulose, the waste textile showed the lowest H/C while straw powder showed the lowest O/C. The HHVs reported in Table 1 also support the trend of O/C and H/C ratios for all types of feedstocks. For example, the HHV shows the lignocellulosic, non-lignocellulosic, and combined lignocellulosic:non-lignocellulosic hydrochars culminate to as high as 28.2, 27.0, and 27.6 MJ/kg, respectively, approaching the fuel quality of coal [43]. Orange peel shows the highest heating value, while sewage sludge shows the poorest heating value [44,45]. This is expected since sewage sludge experiences significant accumulation of ash at the expense of high volatiles after HTC, whereas orange peel experiences significant volatile loss which compliments to a significant increase in fixed carbon [44,45]. Since ash is an inorganic substance, it does not burn but, in fact, reduces the burning capacity, resulting in an overall drop in HHV [46].

The fuel ratio in Table 1 varied between 0.18–1.72 for lignocellulose, 0.09–1.03 for non-lignocellulose, and 0.22–1.22 for combined lignocellulose:non-lignocellulose. This gives an indication on the relative combustion behavior of the biomass. Table 1 shows that the ignition and burnout temperatures for lignocellulose reach as high as 371.3 °C and 750 °C, 388.8 and 832.9 °C for non-lignocellulose, and 354.9 °C and 585.3 °C for combined lignocellulose:non-lignocellulose, respectively. However, the raw feedstocks show 287.1 °C and 329.9 °C for lignocellulose and non-lignocellulose, respectively. In case of the combustibility index, the lignocellulose shows 12.3; however, the non-lignocellulose shows as high as 337. For Co-HTC, it shows 9.3 as the maximum combustibility index. It has been found that volatiles in the biomass first convert into pyrolysis gas as soon as those get exposed to the heat flux, which then react with surrounding oxygen and this phenomenon continues as the surface gets exposed more and more to the heat flux [47]. Liu et al. [48] also supported that lower volatiles in hydrochars make those more stable (supported by lower ignition and burnout temperature), and therefore, they show a less vigorous reaction (as the lower combustion index suggests in Table 1) than raw biomass. Lower volatiles also suggest less of a fire hazard risk than raw biomass [48,49]. In the case of Co-HTC, it is possible that both feedstocks show a synergistic effect on synthesizing stable fixed carbon that augments the thermal stability of the hydrochars. As an example (in Table 1), orange peel shows higher thermal stability than any other lignocellulose, whereas corn stover shows a longer burning time with a higher burnout temperature. Orange peel also shows >44% fixed carbon [45]; however, corn stover shows up to 32% only [50]. However, in the case of Co-HTC, Lin et al. [51] showed that increasing the composition of waste wood, waste paper, and waste food relative to waste textiles decreases the ignition temperature but increases the burnout temperature, resulting in an increased thermal stability and combustion, possibly due to increasing fuel ratio and ash composition. Overall, it has been found that the investigation of Co-HTC has increased by 3.6 times from 2017 to 2021 [29], which could be an emerging future study in upcoming years.

2.2. Water Purification Using Hydrochar and Modified Hydrochar

Figure 2 shows an overview of hydrochar in the application of dye, heavy metal, and toxin removal from water. Therefore, a review of recent advances on these applications is warranted and further discussed below.

Table 1. Fuel and combustion properties of hydrochar.

Feedstock	Reaction Temperature; Time; Solid:Water Ratio	H/C; O/C	Fuel Ratio	HHV (MJ/kg)	Ignition Temperature, T_i (°C)	Burnout Temperature, T_b (°C)	Combustibility Index, $S_i \times 10^{-7}$ (%^{2}/ °C^3.min^2)	References
Walnut shell	180–300 °C; 1–6 h; 1:6–1:5–1:10	0.12–1.51 *; 0.73–0.84 * 0.89–1.58; 0.26–0.75	0.33 * 1.58–1.72	12.7–18.9 * 12.7–28.0				[52,53]
Peanut shell	220 °C; 12 h; 1:7.5	1.58 *; 0.75 * 0.99; 0.27	0.36 * 0.76	12.6 * 28.1	249.7 * 362.7	485.8 * 550.9	2.7 * 1.1	[45]
Orange peel	220 °C; 12 h; 1:7.5	1.76 *; 0.86 * 1.02; 0.27	0.23 * 0.83	12.1 * 28.2	197.0 * 371.3	492.9 * 539.9	3.4 * 1.3	[45]
Rice straw	220 °C; 12 h; 1:7.5	1.74 *; 0.86 * 1.11; 0.28	0.22 * 0.22	16.9 * 20.6	243.6 * 369.1	461.9 * 524.9	3.1 * 0.8	[45]
Corn stover	200–260 °C;0.5–1 h; 1:7.5–1:10	1.40 *; 0.83 * 1.30–0.80; 0.68–0.35	0.22 * 0.18–0.67	16.8–22.4 * 19.2–22.8	198.8–275.0 * 228.9–300.0	492.7–535.0 * 603.2–750.0	6.90–12.3 * 1.20–6.6	[50,54]
Corn stalk	190–240 °C; 0.5–10 h; 1:6–1:10	1.63–1.72 *; 0.75–0.80 * 1.10–1.38; 0.32–0.55	0.09 * 0.33	17.2–17.6 * 19.7–24.7	248 * 295–309	536 * 561–629	6.24 * 1.71–8.0	[55,56]
Grape marc	180–260 °C; 0.5–8 h; 1:3–1:7.5	- 1.36–1.50; 0.53–0.60		20.6–21.6 * 20.9–26.3	215.3 * 233.5	517.7 * 531.0	4.5 * 4.2	[54,57,58]
Straw powder	240 °C; 1.5 h; 1:25	1.51 *; 0.61 * 1.17; 0.36		17.5 * 22.2				[59]
Wood	180–260 °C; 0.5–1.5 h; 1:10–1:12	0.12–2.11 *; 0.73–0.88 * 0.95–1.35; 0.36–0.58	0.24–0.40 * 0.27–1.53	18.0–19.0 * 19.5–24.0	279.0 * 278.9	617.0 * 636.5		[9,51]
Tobacco stalk	180–260 °C; 2–12 h; 1:20	1.57 *; 0.70 * 1.51–0.97; 0.19–0.68	0.20 * 0.21–1.15	18.8 * 18.7–27.2	287.1 * 294.4–342.8	541.0 * 529.4–558.5		[60]
Saw dust	220 °C; 10 h; 1:6	1.67 *; 0.75 * 1.25; 0.42	0.08 * 0.33	18.7 * 24.4				[56]
Sewage sludge	180–280 °C; 2–12 h; 1:7.5–1:9	2.07 *; 0.52 * 1.77; 0.36	0.12 * 0.22	9.3 * 6.0	212.1–228.3 * 193.6–243.5	499.5–839.1 * 408.2–832.9	0.4–337 * 0.1–131	[44,45]
Urban waste/yard waste	160–260 °C; 2–24 h; 1:10	1.46 *; 0.84 * 1.02–1.37; 0.40–0.81		15.4 * 15.7–24.6	272.3 * 312.1–320.5			[61]
Polyvinyl chloride	240 °C; 1.5 h; 1:25	- 1.05; 0.15		22.5 * 25.9				[59]
Cow manure	180–260 °C; 0.083–1 h; 1:5	1.28 *; 0.58 * 1.10–1.22; 0.32–0.55	0.13 * 0.11–0.28	16.7–19.1 * 18.8–22.1	- 179.6	- 588.8	- 7.8	[54]
Sweet potato waste	180–300 °C;0.5 h; 1:5	1.45 *; 0.53 * 0.94–1.35; 0.22–0.48	0.26 * 0.33–1.03	21.2 * 21.7–27.0	316.9 * 309.0–388.8	529.4 * 524.7–550.2	9.9 * 3.82–9.90	[62]

Table 1. *Cont.*

Feedstock	Reaction Temperature; Time; Solid:Water Ratio	H/C; O/C	Fuel Ratio	HHV (MJ/kg)	Ignition Temperature, T_i (°C)	Burnout Temperature, T_b (°C)	Combustibility Index, $S_i \times 10^{-7}$ ($\%^2/°C^3.min^2$)	References
Paper sludge	180–240 °C;0–2 h; 1:1	1.80 *; 0.68 * 1.60–1.40; 0.65–0.48	0.06 * 0.09–0.14					[63]
Swine manure	220 °C; 10 h; 1:6	1.85 *; 0.57 * 1.46; 0.26	0.01 * 0.15	18.1 * 23.1				[56]
Waste textile	240 °C; 1.5 h; 1:12	0.12 *; 0.77 * -	0.20 * 0.29	19.2 * -	329.9 * 332.3	578.1 * 587.0		[51]
Waste paper	240 °C; 1.5 h; 1:12	2.10 *; 0.90 * -	0.16 * 0.53	14.3 * -	314.2 * 332.8	760.5 * 783.5		[51]
Waste food	240 °C; 1.5 h; 1:12	0.19–0.72 * -	0.18 * 0.94	21.3 * -	288.1 * 210.4	716.1 * 719.2		[51]
Polyurethane	200–260 °C; 0.5 h; 1:10	1.35 *; 0.38 * -	0.03 * -	34.1 * -	315.0 -	712.0 * -	6.90 * -	[50]
Straw powder and polyvinyl chloride	240 °C; 0–2 h; 1:25	- 1.01–1.27; 0.12–0.21		- 24.5–27.6				[59]
Corn stover and cow manure (3:1–1:3)	220 °C; 1 h; 1:5			- 19.5–21.2	- 178.2–196.2	- 480.7–530.5	- 8.7–9.3	[54]
Grape marc and cow manure (3:1–1:3)	220 °C; 1 h; 1:5			- 21.1–23.1	- 200.9–354.9	- 492.7–585.3	- 4.7–7.6	[54]
Sewage sludge + Rice straw (3:1–1:3)	220 °C; 12 h; 1:7.5	- 1.17–1.49; 0.35–0.36	- 0.29–0.55	- 8.8–16.8	- 269.3–336.7	- 461.4–525.2	- 0.2–0.3	[45]
Sewage sludge + Orange peel (3:1–1:3)	220 °C; 12 h; 1:7.5	- 1.15–1.54; 0.21–0.29	- 0.34–0.63	- 10.1–21.0	- 266.2–338.8	- 479.2–508.3	- 0.2–0.6	[45]
Sewage sludge + Peanut shell (3:1–1:3)	220 °C; 12 h; 1:7.5	- 1.13–1.51; 0.28–0.34	- 0.39–0.79	- 10.4–21.7	- 276.2–349.2	- 467.5–525.2	- 0.3–0.6	[45]
Swine manure + sawdust (3:1–1:3)	220 °C; 10 h; 1:6	- 1.28–1.41; 0.31–0.37	- 0.24–0.36	- 23.2–24.1				[56]
Swine manure + corn stalk (3:1–1:3)	220 °C; 10 h; 1:6	- 1.30–1.45; 0.28–0.36	- 0.25–0.33	- 23.6–24.2				[56]

Table 1. *Cont.*

Feedstock	Reaction Temperature; Time; Solid:Water Ratio	H/C; O/C	Fuel Ratio	HHV (MJ/kg)	Ignition Temperature, T_i (°C)	Burnout Temperature, T_b (°C)	Combustibility Index, $S_i \times 10^{-7}$ ($\%^2/°C^3.min^2$)	References
Waste textile + waste wood (3:1–1:3)	240 °C; 1.5 h; 1:12	- 0.90–1.20; 0.30–0.35	- 0.60–1.22	- 22.3–25.1				[51]
Waste textile + waste paper (3:1–1:3)	240 °C; 1.5 h; 1:12	- 0.95–1.20; 0.30–0.36	- 0.39–0.56	- 22.7–25.5				[51]
Waste textile + waste food (3:1–1:3)	240 °C; 1.5 h; 1:12	- 1.00–1.40; 0.20–0.40	- 0.54–0.85	- 22.0–26.9				[51]
Corn stover + polyurethane (5.7:1–19.0:1)	200–260 °C; 0.5 h; 1:10	- 0.82–1.38; 0.36–0.72	- 0.22–0.64	- 18.1–22.5	- 325.0	- 626.0–662.0	- 2.03–4.60	[50]

* indicates values for raw.

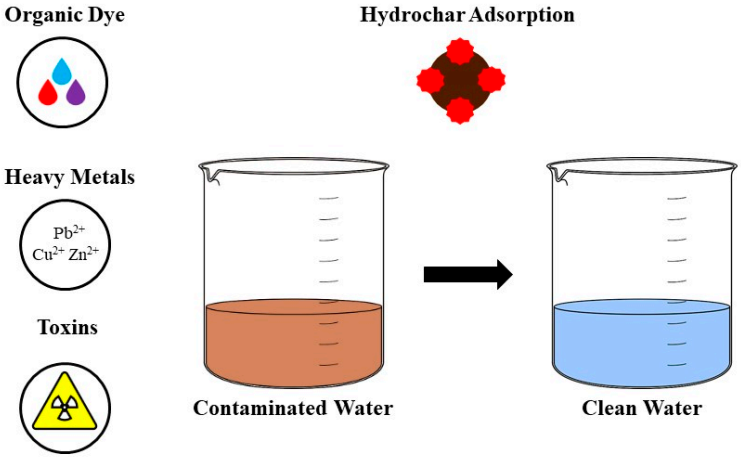

Figure 2. Contaminant removal from water by hydrochar.

2.2.1. Recent Advances on Dye Adsorption by Hydrochar

Hydrochar as an adsorbent material for the treatment of dye-contaminated water has proven to be an efficient and economical viable resource [64]. As such, studies have shown the adsorption performance of hydrochar with various dye types (cationic/anionic), with most in favor of cationic dyes (methylene blue, rhodamine b, methyl green) rather than anionic dyes (methyl orange, acid red 1) [65].

Table 2 shows the research findings of the adsorption performance, isotherm, and mechanisms of hydrochar derived from various feedstocks for treating different dye-contaminated solutions under similar batch sorption conditions. Table 2 introduces hydrochar adsorbent with low surface porosity (S_{BET}: 5–50 m^2/g) reporting relatively low maximum adsorption capacity (Q_{max}) between 30 and 71 mg/g [16,65–67]. It is observed that the adsorption mechanisms for the mentioned hydrochars were similar with chemical interactions between the char surface and dye molecules due to surface functionality being the dominating influence for the removal. Thus, as hydrochar presents minimal surface porosity, adsorption is compensated for based on the surface oxygen containing functional groups. However, studies have discovered ways to improve the dye Q_{max} by performing post-modification of hydrochar and altering the physico-chemical properties [68]. From Table 2, some post-modifications presented are acid etching, chemical activation, one-pot synthesis, Co-HTC, ozone treatment, magnetic modification, and functionality doping (amine, carboxylate, nitrogen, polyamine carboxylate) which significantly improved the Q_{max} (47–5181 mg/g) [24–26,69–88]. As presented in Table 2, Tran et al. [65] performed a study on glucose-activated hydrochar derived from spherical hydrochar functionalized with triethylenetetramine for adsorption application where spherical hydrochar was used as the control. Consequently, with further modifications of the spherical hydrochar, ~1200% and ~640% increases in Q_{max} were reported for methyl green 5 and acid red 1 removal, respectively. Similarly, Ferrentino et al. [67] investigated sewage sludge hydrochar as an option for methylene blue contaminated wastewater treatment in which comparative analysis between hydrochar and chemically activated hydrochar was performed. The study showed that by mixing the sewage sludge-derived hydrochar with KOH, about a 250% increase in Q_{max} could be observed due to the enhanced surface functionality.

As varying post-modification treatments increase the adsorption capacity of hydrochar, diverse possible adsorption mechanisms conceivably explain the dye uptake such as pore filling due to specific surface area, mesoporosity, pore volume, electrostatic attraction/hydrogen bonding due to charged attraction between the adsorbate and adsorbent, oxygen containing functional groups, π-π interactions, and ion exchange [24–26,69–88]. Table 2 shows the different adsorption mechanisms for the various hydrochars, and importantly, how adsorption is governed by one dominant mechanism and/or a complex of different mechanisms. For the studies reported in Table 2, the pore-filling mechanisms showed an adsorption capacity of 85.8 and 200.0 mg/g due to the active binding sites made

available based on specific surface area, 513.0 and 876.1 m^2/g, respectively [25,85]. The studies which observe electrostatic interactions as the dominant mechanisms recorded adsorption capacity ranging from 208.6 to 909.1 mg/g [73,79,81,86], based on the type of charged attraction between the hydrochar and dye molecule (negative hydrochar surface attracts positive cationic dye and vice versa). In Table 2, research presented adsorption capacity stretching from 47.3 to 357.4 mg/g [71,76,80] owing to the surface functional groups being the dominant factor after modification. However, popular studies reported that more complex adsorption mechanisms can show more than one dominating factor for adsorption ranging from 78 to 5181 mg/g [24,26,69,70,72,74,75,77,78,82–84,87,88].

Apart from the adsorption mechanisms, the articles reported in Table 2 also detail the adsorption isotherm which depicts the behavior of the adsorbate onto the hydrochar. Here, mostly the monolayer adsorption (Langmuir) mechanism is observed [24–26,64–68,71,72,74–78,81–83,86]. However multilayer adsorption such as Freundlich [73,84,85] and Langmuir–Freundlich [16] is also described, revealing this change in adsorption behavior to be dependent on the different type of feedstock, and hydrochar modification. Thus, dye removal via hydrochar adsorption has been proven to be vastly effective with superior performance being allotted to hydrochar with post-modifications.

In summary, it is observed that for hydrochar, the dominant adsorption mechanisms are chemical interactions, as active binding sites are made available through the HTC process. As for the modified hydrochar, complex adsorption mechanisms are present such as pore filling, electrostatic attraction, and chemical interactions, playing dominant roles, driving the higher uptake of dye.

2.2.2. Heavy Metals Removal from Water by Hydrochar and Activated Hydrochar

The Table 3 shows the heavy metal adsorption performance by various hydrochars and activated hydrochars derived from different lignocellulosic and non-lignocellulosic feedstocks at different HTC and modification conditions. Our review has narrowed down to most common heavy metals, e.g., Pb^{2+}, Cu^{2+}, Zn^{2+}, Cd^{2+}, and Ni^{2+}, where Pb^{2+} stood out as the most toxic metal, as per the World Health Organization [89]. Hence, removal of these heavy metals from water in an eco-friendly way is warranted and treatment by hydrochar is considered a sustainable solution [90]. The HTC is performed at 200–300 °C, 0.5–24 h, and 1.5:1–1:10 solid–water ratio to synthesize hydrochar [82,91–95]. The hydrochars possess a high BET surface area which plays a role in heavy metal adsorption. For example, avocado seed hydrochar having a 40.5 m^2/g BET surface area shows 9.4–24.9 mg/g for Ni^{2+}, $Cu^{2+,}$ and Pb^{2+} ions at 25 °C and it further increases by as high as 2 times with increasing adsorption temperature [90]. It is also hypothesized that surface functional groups (phenolic and carboxylic) interact with multiple metallic ions at once, while Van der Waals and physical attraction are responsible for endothermic monolayer adsorption [90]. Rice straw hydrochars show 16 times more Cu^{2+} adsorption capacity than avocado seed due to high oxygen containing functional groups, rough surface, and higher pore volume, although having 60.5% lower BET surface area [91].

However, further modification of hydrochar could also be a potential route for better heavy metal removal. In an effort by Nadarajah et al. [96], rice straw hydrochar modified by $FeCl_3$ showed 11% higher BET surface area and 4% higher Pb^{2+} and Cu^{2+} removal, possibly due to a change in band intensities of oxygen-containing functional groups that contribute to surface complexation and spontaneous endothermic adsorption. In another study, the hydrochar produced via the HTC process of peanut hull feedstock with water at 300 °C and 5 h showed 16 times increased lead ion adsorption capacity where the isotherm diverted from Freundlich to Langmuir after modification with 10% H_2O_2 solution indicating the introduction of homogeneity in the surface [92]. Xue et al. [92] reported a significant rise in the carboxyl functional group after modification, which adsorbed the metal ions through a surface exchange reaction like surface complexation. The modified hydrochar was further used for a multi-metal adsorption test in the presence of Pb^{2+}, Cd^{2+}, Cu^{2+}, Ni^{2+} ions where its removal ability showed a trend of $Pb^{2+} > Cu^{2+} > Cd^{2+} \sim Ni^{2+}$ [92].

Table 2. Dye adsorption by hydrochars and activated hydrochars.

Feedstock	Dye	HTC (Ratio/Temperature/Time)	Modification/Production Temperature/Time	S_{BET} (m^2/g)	Q_{max} (mg/g)	Adsorption Isotherm & Mechanisms	Ref.
Glucose	MG5, AR1	Triethylenetetramine (TETA) powders, 190 °C, 48 h *	- NaOH was firstly impregnated then pyrolyzed at 800 °C and 3 h **	- 233 **	13.9, 21.2 175 **, 156 **	Langmuir For the glucose-activated carbon (GAC), ion exchange between the adsorbent and the MG5 played a key role in adsorption. As for AR1, the hydrogen bonding interactions between the nitrogen- and oxygen-containing functional groups on the dye and the GAC was responsible for the adsorption.	[65]
Corn Stover	RhB	DW 230 °C, 30 min	-	6.00	30.70	Langmuir–Freundlich Surface pH, higher pore volume, and functional groups density influenced adsorption capacity compared to the control material.	[16]
Orange Peel; Grape Skin	MB	DW 180–250 °C, 30 min	-	46.16	51.02	Langmuir The adsorption mechanism was owed to the density of the functional groups as it provided more active sites to adsorb dye molecules.	[66]
Sewage Sludge	MB	Palatable Sludge + Digestate 190–250 °C, 3 h	- KOH ** Room temperature and 1 h **	31.00 0.29 **	70.51 247.06 **	Langmuir Surface active sites, chemical interactions, and acid-base or redox equilibria between the MB molecules and the sewage sludge hydrochar.	[67]
Bamboo Shoot Shell	RhB	DW 200 °C *, 5 h *	Pyrolysis treatment at 300, 600, 800 °C, 24 h **	513	85.8	Freundlich More amounts of RhB are absorbed due to larger surface area and pore volume with smaller resistance for adsorbates diffusion into inner pores.	[85]
Coconut Shell	MB	DW 200 °C, 2 h	NaOH (2:1) 600 °C, 1 h	876.14	200.01	Langmuir The optimum MB removal performance was owed to the mesoporosity, pore volume, and surface area present in the COSHTC (coconut shell HTC and NaOH chemical activation)	[25]
PVC + Bamboo	MB	DW 200, 215, 230 °C, 24 h	-	4.08	208.62	- Electrostatic attraction by -$N(CH_3)^+_2$ of MB and carboxylate of hydrochar and hydrogen bonding interactions via N atom of phenothiazine in MB and C-OH of hydrochar.	[79]

Table 2. *Cont.*

Feedstock	Dye	HTC (Ratio/Temperature/Time)	Modification/Production Temperature/Time	S_{BET} (m^2/g)	Q_{max} (mg/g)	Adsorption Isotherm & Mechanisms	Ref.
Betel Nut Husk (BNH)	MB	DW 200 °C, 1 h	NaOH 500 °C, 1 h	517.6	429.6	Freundlich Electrostatic Forces of attraction proven to be one of the driving forces of MB adsorption due to the negatively charged surface on the activated BNH hydrochar (BNH-HAC). However, using the Boyd Model, the Film diffusion model was confirmed for the adsorption mechanism.	[73]
Waste Shrimp Shell	MO	DW (180 °C, 12 h)	Acetic Acid for Acid etching (Room Temperature, 1.5 h)	12.65	755.08	Langmuir Adsorption performance of waste shrimp shell (WSS) hydrochar was mainly attributed to electrostatic interactions.	[86]
Bamboo	MO	HCl 200 °C, 24 h	Epichlorohydrin for etherification (80 °C, 4 h) DW and Diethylenetriamine for amination (60 °C, 4 h) HCl for protonated reaction (Room temperature, 1 h)	11.756	909.09	Langmuir For the protonated amine-modified hydrochar (PAMH), electrostatic interaction played a key role on the sorption of MO.	[81]
Bamboo Sawdust	MB	$ZnCl_2$ with HCl (acid washing) One-Pot (200 °C, 7 h) One-Pot + Acid Rinse (200 °C, 7 h)	-	29.6	47.3	- High Oxygen functional group content, aromaticity, and surface area led to an increase in adsorption ability of MB onto the modified hydrochar.	[80]
Pinewood	MB	DW 300 °C, 4 h	Oxone + NaCl (catalyst) Room temperature, 24 h	7.662	86.7	Langmuir Chemical interaction between adsorbent carboxylate anion and cationic adsorbates with minor physical interactions.	[76]
Coffee Husk	MB	DW 180 °C, 6 h	KOH 700 °C, 4 h	703.9	357.38	Langmuir High uptake of MB dye was observed for coffee-derived activated carbon with high amount of oxygen-containing functional groups.	[71]
Coffee Husk	MB	DW 220 °C 6 h	$FeCl_3 \cdot 6H_2O + FeSO_4 \cdot 7H_2O$ Ammonia Solution Co-precipitation: (80 °C, 30 min)	-	78	Freundlich Thermodynamic properties indicated the adsorption mechanism for MB removal to be a physical process between the magnetic composite of coffee husk hydrochar-Fe_3O_4 (MCHH) and MB.	[84]

Table 2. *Cont.*

Feedstock	Dye	HTC (Ratio/Temperature/Time)	Modification/Production Temperature/Time	S_{BET} (m^2/g)	Q_{max} (mg/g)	Adsorption Isotherm & Mechanisms	Ref.
Olive Oil Cake	MB	DW 150–300 °C, 2–8 h	KOH, NaOH, H_2O_2, or NH_2CONH_2 Room temperature, 1 h	7.11	270.3	Temkin Hydrogen bonding, electrostatic, and coordinate interactions were the dominant factors influencing the adsorption of MB onto the olive oil derived activated carbon.	[88]
Distillers Grains	MB	Ultrapure Water with Attapulgite/Vermiculite 180 °C, 6 h	-	-	340.3	- Electrostatic attraction, ion exchange, complexation, and physical adsorption controlled the adsorption process for the derived hydrochar-clay composites.	[70]
Sugar Cane Bagasse	MB	H_3PO_4 240 °C, 10 h	NaOH Ambient temperature, 2 h	15.34	357.14	- MB uptake was mainly attributed to the electrostatic attraction, hydrogen bonding, π-π interaction, and intra-particle diffusion due to the functional groups and porous structure present in AHC (activated hydrochar).	[69]
Golden shower	MG5	190 °C, 24 h	Pyrolysis (800 °C, 4 h) K_2CO_3 was used for activation (80 °C, 24 h)	903	531	Langmuir Adsorption process was dominated by the π-π interactions and pore filling mechanisms.	[72]
Teak Sawdust	MB	DW 190 °C, 24 h	$K_2CO_3/ZnCl_2$ 800 °C, 4 h	1757	614	- Electrostatic force is the primary adsorption mechanism for the MB removal with an increasing amount of oxygen-containing functional groups also playing an important role in capture.	[87]
Bamboo Sawdust/Powder	MB	DW [81]; Acrylic Acid + Ammonium Persulphate + DW [80] 200 °C, 24 h [80,81]	NaOH Room temperature, 1 h [81]; 2 h [80]	26.249; 5.03	655.76; 717.78	Langmuir [80,81] Due to the large surface area, pore volume, and increased amount of oxygen-containing functional groups, high MB adsorption was achieved for the derived modified bamboo hydrochar [81]. Electrostatic interaction presented as the main factor for MB adsorption [80].	[74,77]
Rice Straw	MO	Ferric Sulfate, Ferric Chloride, DW, NaOH 180 °C, 6 h	Epchlorohydrin + DMF for etherification (100 °C, 1 h) Pyridine (1 h) and Trimethylamine (3 h) for amination	-	849	Langmuir For MO removal, primarily electrostatic attraction and ion exchange influenced the adsorption mechanism between the dye and the quaternary ammonium-functionalized rice straw hydrochar.	[75]

Table 2. *Cont.*

Feedstock	Dye	HTC (Ratio/Temperature/Time)	Modification/Production Temperature/Time	S_{BET} (m^2/g)	Q_{max} (mg/g)	Adsorption Isotherm & Mechanisms	Ref.
Bamboo Powder	MB + MO [69] MB [72,87]	HCl [69,72,87] 200 °C, 24 h [69,72]	Epichlorohydrin for Etherification (80 °C, 4 h) [69,87] Water/Diethylenetriamine for Amination (60 °C, 4 h) [69,87] $FeCl_3 \cdot 6H_2O$ + $FeSO_4 \cdot 7H_2O$ for Chemical Coprecipitation (Room temperature, overnight) [69] NaOH + Water + Ethanol for Carboxylated Reaction (60 °C, 4 h) [87] Maleic Anhydride + $NaHCO_3$ 140 °C, 6 h [72]	26.94; 28.189; -	148.84; 1155.57; 1238.66	Langmuir [69,72,87] Selective removal of MB onto Fe_3O_4-loaded PAMH (Fe_3O_4-PAMH) due to electrostatic interaction at acidic/alkaline conditions [69]. π -π interaction, electrostatic attraction, and hydrogen bonding between MB and the carboxylate-functionalized hydrochar (CFHC) were the main mechanisms for MB removal [72]. ΠΙ-π interaction, hydrogen bonding, and electrostatic attraction dominated MB capture between the polyaminocarboxylated modified hydrochar (ACHC) with MB [87].	[24,82,83]
Bamboo Shoot Shell	RhB	1 wt% H_2SO_4 200 °C, 24 h	Melamine for pre-carbonization (600 °C 4 h) KOH for chemical activation (600–800 °C, 1 h)	3250	3860	Langmuir Adsorption was governed by synergistic effects of large surface areas, hierarchical architecture, and partial N-species for pyrrolic-N coordination.	[78]
Glucose (10 wt% glucose water)	RhB	190 °C, 18 h	Air oxidation for oxidation (300 °C) then mixed with Urea KOH for chemical activation (600–800 °C, 1 h)	3282	5181	Langmuir For the N-doped hierarchical carbons, the adsorption performance was credited to the synergistic effects of high surface areas, hierarchical pores and pyrrolic N in the structure.	[26]

* HTC; ** activation; DW—DI water; MB—Methylene Blue; MO—Methyl Orange; MG5—Methyl Green 5; AR1—Acid Red 1.

Modified and activated bamboo powder hydrochar shows the Langmuir isotherm for Cu^{2+} removal and supports spontaneous endothermic adsorption via electrostatic attraction, ion exchange, and chelation attraction of metal ions with surface oxygen-containing functional groups [82,83]. Li et al. [82] further showed that a 20 °C increase in the adsorption temperature can improve the adsorption capacity of Cu^{2+} by up to 3%. Corn cob hydrochar, if modified by acidic and alkaline treatment followed by polyethyleneimine, can uptake up to 2–10 times more Cu^{2+}, Zn^{2+}, and Pb^{2+} [93,97,98]. Although corn cob does not show a satisfactory BET surface area, researchers agreed that the possible reason for enhanced adsorption could be: (1) –N–Zn/Cu (II) complex formation and electrostatic interaction of $–NH_3^+$ & $–NO_3^-$ ions with metals; (2) oxygen (carboxyl and hydroxyl groups) and nitrogen-containing functional groups promoting ion exchange and hydrogen bonding. Alkali treatment was also found to remove blocked pores and improve surface area for Cr^{6+} ion adsorption by corn cob, corn straw, and eucalyptus sawdust [98]. Modification with nitrates and urea influenced the co-ordination effect induced by N_2 in the surface, surface co-precipitation, and electrostatic interaction in Pb^{2+} adsorption by sewage sludge, although rigorous studies are yet to be conducted because of its significant variability in heterogeneity and moisture content [95]. A case of mixed feedstocks, e.g., straw and poultry litter, was reported by Ghanim et al. [94], which reported acid modification can yield a similar adsorption capacity for Cr^{6+} like Khushk et al. [98] but the mechanism is driven by redox reactions, ion exchange, and electrostatic interactions with Cr^{6+} [94].

Table 3. Heavy metal adsorption by hydrochars.

Feedstock	Metal	HTC Condition and Chemical Modification	Adsorption Condition	BET (m^2/g)	Q_e (mg/g)	Adsorption Isotherm, Thermodynamics and Mechanism	Ref.
Avocado Seed	Ni^{2+} Cu^{2+} Pb^{2+}	S/W = 1.5 * 250 °C, 12 h *	120 rpm 24 h 25–40 °C	40.54	9.39–20.54 8.89–13.98 24.86–49.72	- Endothermic Surface functional groups (phenolic and carboxylic) interaction with several metallic ions (multiionic process), Van der Waals force, and electrostatic interaction.	[90]
Rice Straw	Cu^{2+} Zn^{2+}	S/W = (1:10) * 200 °C, 70 min *	170 rpm, 25 °C, 8 h	16.03	144.9 112.8	Langmuir Spontaneous and Exothermic Presence of oxygen containing functional groups, higher pore volume, and rough surface	[91]
Rice Straw	Pb^{2+}, Cu^{2+}	$FeCl_3$ (1: 3) ** 200 °C, 3 h * 200 °C, 3 h **	150 rmp, 25 h 30 °C	39.9 44.3	6.75 4.0	Langmuir Spontaneous and Endothermic Surface complexation with surface functional groups (carbonyl, carboxyl, and anhydride)	[96]
Peanut Hull	Pb^{2+} Cd^{2+} Cu^{2+} Ni^{2+}	S/W = 3:20 * 10% H_2O_2 solution ** 300 °C, 5 h * 22 ± 0.5 °C, 2 h **	24 h, 22 ± 0.5 °C	1.3 1.4	1.40 0.07–22.84	Freundlich - Langmuir - High carboxyl surface functional groups Surface exchange reaction like complexation mechanism	[92]

Table 3. *Cont.*

Feedstock	Metal	HTC Condition and Chemical Modification	Adsorption Condition	BET (m^2/g)	Q_e (mg/g)	Adsorption Isotherm, Thermodynamics and Mechanism	Ref.
Corn cob straw	Cu^{2+} Zn^{2+}	S/W = (1:6) * 200 mL HCl(1N)/NaOH(3N), PEI/methanol solution (10% (*w*/*v*) ** 200 °C, 0.5 h * 160 rpm, 30 °C, 24 h **	180 rpm, 4 h, 25 °C	2.09 Acid-PEI-HC: 2.10 Alkali-PEI-HC: 3.98	47.0–56.1 152.2–207.6	Freundlich - –N–Zn/Cu (II) complex formation and electrostatic interaction of $–NH_3^+$ & $–NO_3^-$ ions with metals contributed to ion adsorption Metal ions were adsorbed by acid-PEI-HC, and nitrogen chelation was primarily in control. However, the adsorption process for alkali-PEI-HC also involved groups that contained oxygen.	[93]
Poultry Litter with straw	Cr^{6+}	DI water * H_2SO_4 * 250 °C, 2 h * 250 °C, 2 h **	24 h 20 °C	7.1 3.5	26.2	Langmuir Spontaneous and Endothermic The elimination mechanism may be influenced by redox reactions, ion exchange, and electrostatic interactions.	[94]
Bamboo powder	Cu^{2+}	HCl * NaOH ** Epichlorohydrin, water/ diethylenetriamine solution NaOH, DI water, ethanol, monochloroacetic acid ** 200 °C, 24 h * 80 °C, 4 h ** 60 °C, 4 h **	110 rpm, 30–50 °C, 12 h	-	139.60–143.96	Langmuir Endothermic, Spontaneous. Electrostatic attraction and chelation attraction of metal ions with surface functionalities contributed to the adsorption process.	[82]
Sewage Sludge	Pb^{2+}	$Mg(NO_3)_2.6H_2O$, urea $Al(NO_3)_3.9H_2O$, DI water ** 120 °C, 24 h * Centrifugal washing **	150 rpm, 25 °C, 24 h	-	85.78	Langmuir - Contribution of physical (Van der Waals) and chemical adsorption (functional groups). Coordination effect induced by N_2 in the surface, surface coprecipitation, and electrostatic interaction played a major role in lead adsorption.	[95]
Bamboo powder	Cd^{2+}	HCl * Maleic anhydride (1:2), $NaHCO_3$ ** 200 °C, 24 h * 140 °C, 6 h **	110 rpm, 30 °C, 24 h	45.795 28.189	90.74	Langmuir Spontaneous and Endothermic Surface complexation between Cd^{2+} and surface oxygen functional groups along with ion exchange between K^+ and Cd^{2+} had a significant role in adsorption.	[83]
Eucalyptus sawdust, Corn straw, Corn cob	Cr^{6+}	S/W = (1:8) * KOH (1:50)(*w*/*v*) ** 220 °C, 0.5 h * 30 °C, 1 h **	180 rpm, 25 °C, 8 h	17.48 16.08 15.80	29.46–34.07	- - Alkali modification improved the blocked pores which resulted in higher adsorption.	[98]

Table 3. *Cont.*

Feedstock	Metal	HTC Condition and Chemical Modification	Adsorption Condition	BET (m^2/g)	Q_e (mg/g)	Adsorption Isotherm, Thermodynamics and Mechanism	Ref.
Pinewood sawdust	Pb^{2+}	S/W = 1:6 * 20% H_2O_2 solution ** 260 °C, 2 h * 300 rpm, 30 °C, 6 h **	200 rpm, 25 °C, 24 h	—	92.80	Freundlich - Functional group (carboxyl and hydroxyl) complexation and π-interaction contributed to metal ion adsorption.	[99]
Corn straw	Pb^{2+}	25%(v/v) H_3PO_4, PEI-Methanol (1:10) solution ** 240 °C, 2 h * 200 rpm, 30 °C, 12 h **	150 rpm, 25 °C, 12 h	11.3 7.2 22.5	32.67 214.0 353.4	- - Oxygen-rich functional group, Carboxyl and hydroxyl groups, along with nitrogen-rich functional groups, contribute to adsorption process through ion exchange, hydrogen bonding.	[97]

* HTC; ** activation; S/W = solid-to-water ratio.

It can be concluded that hydrochars found from HTC are good for heavy metal removal from water [90,91]. However, further modification of the hydrochars with acids, alkaline, and oxidizers improve the heavy metal removal efficiency by increasing oxygen-containing functionalities [96,99]. The oxygen-containing functionalities are important because they drive the surface complexation reaction with the heavy metal ions and eliminate them from water [96,99]. It is also observed that not only surface complexation but also physical attraction via Van der Waals and electrostatic force may influence the adsorption [90,95].

2.2.3. Toxin Removal from Water by Hydrochars and Activated Hydrochars

Table 4 shows the adsorption of pharmaceuticals and organic toxic compounds by hydrochars and modified hydrochars. With the increasing population resulting in greater emission of organic components from personal care products to pharmaceuticals, the ineffective removal record by conventional wastewater depuration treatments has raised serious concerns for the environment and human health subsequently [100,101]. Therefore, this review on toxin removal attempts to summarize the effectiveness of using low-cost hydrochar and its modified version. The most common toxin used in pharmaceutical and personal care products is narrowed down to paracetamol, triclosan, ibuprofen, diclofenac, tetracycline, and bisphenol, etc. Diclofenac stood out first as it is a non-steroidal anti-inflammatory medicine used as a painkiller, an anti-arthritic, a treatment for women's menstruation pain all over the world, and readily passes through the nanofiltration equipment in the water treatment plant due to its negative charge [102]. Table 4 suggests most of the studies focused on lignocellulosic feedstocks possibly due to their homogeneity, readily availability, and higher capacity for toxin adsorption [103,104]. For example, the olive mill hydrochar shows a 2% increase in the BET surface area with increasing temperature that plays a role in toxin removal [105]; however, <43% removal was obtained for ibuprofen and >98% removal was obtained for ibuprofen triclosan, possibly due to the higher water solubility of ibuprofen and higher hydrophobicity of triclosan, which occupies most of the adsorption site and limits site for other toxins [105]. Qureshi et al. [106] showed the highest adsorption for diclofenac, having a BET surface area of 1160 m^2/g of hydrochar from the fruit powder of *Zizipus mautitian*, and hypothesized that the removal of the toxins shows physical attraction via the pore-filling mechanism in a monolayer & multilayer adsorption and fits well with the Dubinin–Raduskevich isotherm. In another study, hydrocar from olive stones shows efficient removal for diclofenac via film diffusion and intraparticle diffusion of the toxin molecules [104]. Pauletto et al. [107] showed that avocado seed hydrochar removes 2-Nitrophenol (562.37 mg/g) via a greater surface cavity and electrostatic interaction, even though it has a relatively lower BET surface area. Hydrochar from *Saccarum*

ravnnae removes 2 times more diclofenac, 2.5 times more ibuprofen, and 3 times more naproxen than the hydrochar from *Saccarum officinarum* [108], indicating rapid hydrogen bonding, π-π interaction, and electrostatic interactions [108]. As reported by Liu et al. [109], hydrochar from watermelon peel shows up to 2 times more 2,4-dichlorophenoxy adsorption with increasing temperature, whereas lettuce and taro hydrochar's toxin removal efficiency drop by 13% and 168%, respectively. The adsorption for these hydrochars is mostly driven by chemisorption and partitioning where the mesoporous structure of the adsorbent and C-O surface functional group plays a significant role [109]. In another study, tomato and olive press waste, rice husk, and horse manure hydrochars adsorbed 10 different toxins found in wastewater, where horse manure and rice husk chars showed 100% removal of diclofenac and bisphenol, possibly due to higher surface area along with the hydrophobic, electrostatic, and polar attraction with hydrophobic, hydrophilic, and polar toxins [110].

It is evident that hydrochar acts as effective adsorbent material via physical adsorption; however, incorporating chemisorption through electrostatic interaction, π-π interaction, and oxygen-rich functionalities may be improved by advanced treatment like activation, post treatment, etc. For example, nitrogen-activated palm kernel shell hydrochar results in 6 times greater BET surface area with diclofenac uptake of 13.16 mg/g where an increase in the carboxyl functional group accelerated the removal of a toxin by forming a hydrogen bond and π-π interaction with aromatic rings [102]. A similar trend was reported by Mestre et al. [103], where the BET surface area of sucrose hydrochar after activation in steam, K_2CO_3, and KOH improves by 69–200% [103]. Further research on KOH and K_2CO_3-activated hydrochar revealed that KOH-activated hydrochar removes 1.1- and 5.6-times more paracetamol and iopamidol, respectively, than K_2CO_3-activated hydrochar due to its greater surface area and micropore volume [103]. Pine fruit shell after being activated with NaOH shows up to a 24% increase in the BET surface area and up to 5–14% higher bisphenol adsorption than lower-temperature HTC hydrochar [111]. Adsorption isotherm is best fitted for the Liu model, indicating that the toxin is adsorbed at several active sites with diverse energies by physical adsorption, H-bonding, electrostatic attraction, and π-π interaction [111]. Poplar sawdust hydrochar after activation via air and N_2 (300–700 °C) to adsorb tetracycline reports a 42-fold increase in BET surface area for N_2 activation at 500 °C and an 82-fold increase for O_2 activation at 500 °C but a decrease of up to 10% for O_2 activation at 700 °C, as the micropore might shift to mesopore [112]. O_2-activated hydrochar at 500 °C with the highest surface area shows the highest uptake of tetracycline (32 times greater than hydrochar and 9 times greater than N_2 activated at 700 °C) through micropore filling, π-π interaction, electrostatic interaction, and hydrogen bonding [112]. As reported by de Araújo et al. [113], adsorption of acetaminophen on KOH-activated Brewer's spent grain has an around 156-times higher surface area with higher micropores than hydrochar that accelerates the toxin uptake quality via hydrogen bond interaction between -O-H of activated hydrochar and N-H groups of acetaminophens, π–π interaction between aromatic rings of adsorbent and toxin [113]. Rice husk hydrochar with alkaline and acidic activation to adsorb berberine chloride and tetracycline shows a higher surface area for HNO_3-activated hydrochar and higher removal of toxins by homogenous distribution of oxygen-rich functional groups after modification [114]. Electrostatic attraction is one of the possible mechanisms for greater removal of tetracycline by H_3PO_4-treated hydrochars with a negative surface, and three factors of surface area, functional groups, and surface charge might work together to provide the maximum adsorption capability of berberine chloride on KOH-treated hydrochar [114]. In another study of carbamazepine adsorption on steam-activated flax shives and oat hull, hydrochar produced in acidic and alkaline solution shows 600–2800 times greater BET surface area than raw flax shives and oat hull, which after H_3PO_4 activation, eventually results in a higher removal of both toxins through increasing hydroxyl and carboxyl functional groups and interconnections between π-electron donors and acceptors [115]. In an experimental finding reported by Fernandez et al. [116], orange peel hydrochar modified in CO_2, air, and H_3PO_4 at a different temperature range shows a 1.5%, 3%, and 4% increase in BET surface area, respectively, after the modification that

influences the adsorption of diclofenac, salicylic acid, and flurbiprofen though mesoporosity and hydrogen bonding. Hydrochar modified in H_3PO_4 is the most effective at removing toxins due to its greater BET area and mesopore volume making it easier for the aromatic molecule to approach the adsorption site and form a hydrogen bond [116]. Finally, a study conducted on a paper board mill to remove diclofenac reported having around a 2.7-times greater BET surface area that increases the toxin intake by up to 10% after the activation in KOH [117]. Both physisorption and chemisorption control the toxin removal mechanism via electrostatic interaction with the positively charged surface, hydrophobic effect of the toxin, Van der Waals force, and higher oxygen rich functional groups after the activation [117].

The review on toxin removal demonstrates the adsorption efficiency of hydrochar which can be further improved after certain modification or activation. Without the modification, the adsorption of toxins on the hydrochar surface is mostly regulated by physical attraction and texture of the surface area [104,106,107] along with Van der Waals force, π-π interaction, and hydrogen bonding [108,110], whereas modification and activation show an increase in the surface area along with a greater amount of the oxygen-containing functional group in the surface, resulting in a higher adsorption of toxins [103,113–117]. It is motivating to observe that much of the research is focusing more on the HTC activation instead of HTC alone for better toxin removal.

Table 4. Toxin removal by hydrochars.

Feedstock	Toxins	Chemical Modifier (Ratio) Production Temperature and Time	Adsorption Condition	BET (m^2/g)	Q_e (mg/g)	Adsorption Isotherm, Thermodynamics and Mechanism	Ref.
Brewer's spent grain	Acetaminophen	S/W = 1:8 * KOH(1:4) ** 220 °C, 16 h * 800 °C, 1 h **	150 rpm, 30 °C, 24 h	9.65 1512.83	- 318.003	Langmuir Hydrogen bond interaction between -O-H of AHC and N-H groups of acetaminophens Π-π interaction between aromatic rings of AHC and acetaminophen	[113]
Flax shives Oat hull	Carbamazepine	H_3PO_4, NaOH * Steam ** 220 °C, 16 h * 850 °C, 1 h **	220 rpm, 20–40 °C	2–793 2.41–602	47–97 50–99	Endothermic Presence of hydroxyl and carboxyl functional groups Interconnections between electron donors and acceptors Hydrogen bonding	[115]
Sucrose	Paracetamol, Iopamidol	DI water * Steam, KOH, K_2CO_3 ** 190 °C, 5 h * 800 °C, 1 h **	700 rpm, 30 °C, 24 h	814–2431	471.8–513.5 150.9–1049.6	Langmuir Larger micropores of KOH-treated HC improved removal efficiency	[103]
Olive mill waste	Triclosan, Ibuprofen, Diclofenac	S/W = 3:7 * 190–240 °C, 6 h *	20 ± 1 °C, 24 h	7.470–7.624	10–13.8	Freundlich Higher oxygen containing functional groups forming bonding with pharmaceutical toxins	[105]
Fruit powder of *Zizipus mautitiana*	Diclofenac, Ibuprofen	S/W = 2:5 * 200 °C, 20 h *	120 rpm, 30 °C, 2 h	1160	752.21 206.96	Dubinin–Raduskevich (physisorption) High surface area and presence of polar functional group Physical attraction by pore filling mechanism in a monolayer and multilayer adsorption	[106]

Table 4. *Cont.*

Feedstock	Toxins	Chemical Modifier (Ratio) Production Temperature and Time	Adsorption Condition	BET (m^2/g)	Q_e (mg/g)	Adsorption Isotherm, Thermodynamics and Mechanism	Ref.
Palm kernel shell	Diclofenac	S:W = 1:5 * Nitrogen ** 200 °C, 4 h * 400 °C, 4 h **	200 rpm, 25 °C, 1.5 h	22 131	13.16	Langmuir Hydrogen bond formation with diarylamine and carboxyl groups; Van der Waals attraction with non-polar groups; π-π interaction with aromatic rings.	[102]
Orange peel	Diclofenac Salicylic acid Flurbiprofen	S/W = 1:10 * CO_2, Air, H_3PO_4 ** 200 °C, 20 h * 300–750 °C, 1.5 h ** 600 °C, 1 h **	500 rpm, 25 ± 1 °C, 1.5 h	117 301–618	5.33–62.46 12.43–91.16 148.99–202.73	- Higher surface area and mesoporosity Hydrogen bonding	[116]
Olive stones	Diclofenac	10% H_2SO_4 (1:1) * 550 °C, 1 h *	500 rpm, 23 ± 2 °C, 3 h	83.72	3.10	Brunauer–Emmett–Teller (BET) Film diffusion and intraparticle diffusion Availability of functional group	[104]
Leaves of *Saccarum ravnnae* and *Saccarum officinarum*	Diclofenac Ibuprofen Naproxen	S/W = 1:8 * 220 °C, 9 h *	180 rpm, Room temperature,12 h	26.21–27.26	62.02–230.04	Langmuir Hydrophobic, Van der Waals force, Surface interaction (π-π interaction) and hydrogen bonding The presence of oxygen rich functional groups (hydroxyl and carboxyl groups)	[108]
Poplar sawdust	Tetracycline	S/W = 1:10 * Air, Pure N_2 ** 220 °C, 8 h * 300–700 °C, 3 h **	25 °C, 72 h	7.5 314.4–358.6 557.6–618.02	6.25 33.32–196.71 6.22–22.21	Freundlich Micropore filling, π-π interaction, electrostatic interaction and hydrogen bonding	[112]
Lettuce Taro Watermelon peel	2,4-Dichlorophenoxy	S/W = 1:25 * 180–240 °C, 2 h *	180 rpm, 25 ± 1 °C, 72 h	3.67–6.90 9.23–0.86 3.29–8.45	80–88.4 35.5–90.2 59.7–88.4	- Mesoporous structure, greater C-O functional group Partitioning and chemisorption	[109]
Pine fruit shell	Bisphenol	S/W = 5:37 * NaOH (1: 3) ** 190 °C, 24–72 h * 700 °C, 1.5 h **	150 rpm, 25 °C, 24 h	90–2220	332.52–378.77	Monolayer adsorption Physical adsorption, electrostatic attraction, hydrogen bond and π-π interaction	[111]
Avocado seed	2-Nitrophenol	S/W = 1:1 * 200 °C, 12 h *	120 rpm, 25 °C, 48 h	18.40	562.37	Henry isotherm Greater cavity in the adsorbent surface Electrostatic interaction	[107]
Rice husk	Berberine chloride Tetracycline	S/W = 1:6 * KOH, NH_4OH, H_2SO_4, HNO_3, H_3PO_4 ** 200 °C, 3.5 h * 170 rpm, 25 °C, 3 h **	170 rpm, 25 °C, 8 h	1.74–12.18	281–352 294–419	Langmuir isotherm Oxygen rich functional groups initiates chemical adsorption Physical adsorption dominant	[114]
tomato- and olive-press wastes, rice husks, and horse manure	Octhilinone, Triclosan, Trimethoprim, Sulfamethoxazole, Ciprofloxacin, Diclofenac, Paracetamol, Diphenhydramine, Fluconazole, and Bisphenol A	Ultrapure water * 220 °C, 2 h *	20 °C, 25 min	0.65–16.92	0.0001-0.002	Hydrophobic molecules get adsorbed via hydrophobic attraction Hydrophilic molecules get adsorbed through electrostatic interaction The polar surface of the char improves adsorption of polar molecules through H-bonding	[110]

Table 4. *Cont.*

Feedstock	Toxins	Chemical Modifier (Ratio) Production Temperature and Time	Adsorption Condition	BET (m^2/g)	Q_e (mg/g)	Adsorption Isotherm, Thermodynamics and Mechanism	Ref.
Paper board mill sludge	Diclofenac	KOH (1:2) ** 200 °C, 10 h * 600 °C, 1 h **	50 rpm, 15 h	19.59 53.32	28.818 31.746	Langmuir Physisorption and chemisorption Electrostatic interaction with positively charged surface, hydrophobic effect, Van der Waals force Greater amount of oxygen rich functional group	[117]

* HTC; ** activation; S/W = solid-to-water ratio.

2.3. Greenhouse Gas Adsorption by Activated Hydrochar

Figure 3 shows the application of hydrochar for greenhouse gas adsorption. Incessant anthropogenic emission of greenhouse gas (GHG), primarily constituted by carbon dioxide and methane, has resulted in global climate change with the grave consequence of threatening species extinction. This has motivated the scientific community to develop inexpensive adsorbents, to reduce the levels of CH_4 and CO_2 with capture technologies, based on sustainable biomass sources. Hence, in the process of developing functional adsorbents, hydrochars have successfully provided an avenue, as activation of such hydrochars have resulted in superior porosity and functionality, owing to the excellent capability of hydrochars to offer pore initiation while having a surface rich in surface functionalities. Pioneered by Fuertes and Sevilla [118], chemical activation of hydrochars resulted in a higher surface area than their conventionally activated counterparts, while hydrochars were demonstrated to be highly functional with a large amount of oxygen-containing groups [119]. Hence, the favorable characteristics of deriving porous activated hydrochars to be employed in GHG emission is extensively reviewed in the following subsections.

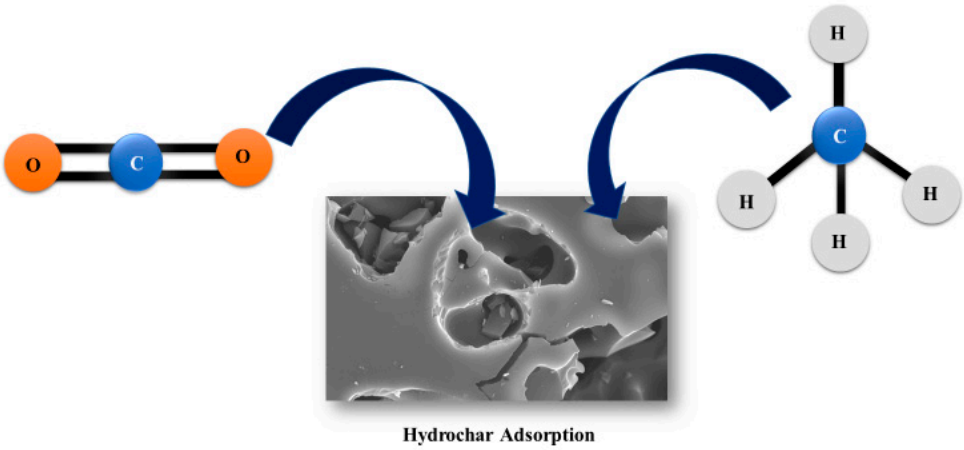

Figure 3. Greenhouse gas adsorption by porous hydrochar.

2.3.1. CO_2 Adsorption

As kinetic diameter, an indication of the size of the molecule, is unique for each adsorbate, in the case of CO_2, a literature review corresponding to the activated hydrochars used as CO_2 adsorbents, as listed in Table 5 with the dominating factor highlighted, summarizes the adsorption of the acidic gas CO_2 as being closely associated with surface porosity as well as surface chemistry, where the latter factor has more driving influence in adsorption at a higher temperature (for example, 50 °C) than at a lower temperature [120].

On the other hand, adsorption of CO_2 at a low pressure is governed by the pore-filling mechanism. In this mechanism, the pore walls interact with the adsorbate molecules and

drive the adsorption process. This signifies the importance of small micropores for enhancing the interactions of the overlapping potential fields from the neighboring pore walls and hence, results in higher CO_2 capture. Hence, pores lower than 1 nm in size present in activated hydrochars demonstrate substantially higher CO_2 capture at sub-atmospheric to ambient-atmospheric pressure, as observed in literature [121–125]. The importance of pore size distribution is imperative where, for example, Matabosch Coromina et al. [121] derived the optimum pore size of 0.5–0.7 nm, Liu et al. [126] derived the optimum pore size of 0.37–0.53 nm, where Guo et al. [122] concluded optimum micropore size distribution to be 0.5–1.0 nm, indicating the research gap of statistically correlating the effect of different pore size ranges on the CO_2 uptake capacity. Moreover, micropore proportion, also termed microporosity, is a crucial metric, concluded in the literature [121–123,127–130] and available in Table 5, as that can signify the fraction of pores that are capable of capturing CO_2 successfully, instead of the traditionally believed surface porosity metric of specific surface area (SSA) and pore volume. For example, Huang et al. [129] demonstrated one of the highest CO_2 uptakes, recorded in Table 5, as 4.83 mmol/g at 1 bar and 298 K, which was primarily attributed to the narrow micropore's volume. Conversely, the role of surface area has a discrepancy in the literature, as reviewed by Rouzitalab et al. [131]. Although a high surface area provides high adsorption sites [132,133], which might facilitate the physical adsorption process, Guo et al. [122] derived a 16.7% reduction of CO_2 uptake, from 4.2 mmol/g to 3.5 mmol/g, despite achieving a higher surface area in the latter. It can be therefore be hypothesized that with the increase of surface area, if the pore size is enlarged, the interaction of CO_2 with the pore walls is reduced, which might result in lower CO_2 uptake. Hence, it might be pivotal to have a sufficiently high surface area consisting of appropriately sized pores. On the other hand, for CO_2 adsorption at elevated pressure, the likely mechanism of CO_2 adsorption is surface coverage and a combination of large micropores/small mesopores–macropores benefit the CO_2 captured, as meso/macro pores improve the CO_2 mass transportation within the porous carbon skeleton [134–138]. For example, Sevilla et al. [118] also demonstrated the necessity of pores in the micro–mesopore range, termed as the bimodal porosity, that helped in achieving the highest ever reported CO_2 adsorption capacity of 21 mmol/g in porous carbons at 25 °C and at a high pressure of 20 bar.

On the other hand, despite sufficient studies emphasizing the role of surface porosity, the additional influence of surface chemistry on CO_2 adsorption is scarcely studied and correlated to its uptake capacity. For example, Ghuangzhi et al. [139] studied the effect of HTC on the surface functionality of the derived porous carbons and investigated its performance as CO_2 adsorbent, but there was no obvious correlation between the variables found. However, Sarwar et al. [140] indicated superior CO_2 adsorption in KOH-activated porous carbons due to the 'basic nature' of the porous activated hydrochar. In light of that, functional groups such as pyridinic-N could enhance the adsorption performance of CO_2, as it has the ability to donate a lone pair of electrons, resulting in the alkalinity of the adsorbent surface, whereas richness with other nitrogen-containing functional groups such as amine- or imine-N, pyrrolic-N, quaternary-N, and graphitic-N can benefit by a stronger chemisorption effect for CO_2 adsorption [141]. To augment the quantity of such functional groups, the introduction of nitridizing agents (for example, melamine, ethylenediamine, or urea) is a novel approach where this can be incorporated in the step of the HTC [129,130] or during the step of activation of hydrochar [127]. As a result, the microporous activated hydrochars' relative percentage of pyrrolic-N was significant where urea-nitridized tobacco stalk-derived activated hydrochar exhibited the highest atmospheric CO_2 uptakes of 4.83 mmol/g at 25 °C and 7.35 mmol/g at 0 °C [129]. The same nitridizing agent, while hydrothermally carbonizing glucose, upon activation, demonstrated a CO_2 adsorption ability of 4.26 and 6.70 mmol/g at 25 °C and 0 °C, respectively [130]. While both the research studies highlighted the significance of nitrogen functionality, the simultaneous high N content of the porous activated hydrochars were also attributed to superior CO_2 uptake in addition to the synthetic effect of narrow micropores being emphasized equally.

Moreover, despite the significance of surface porosity and functionality in activated hydrochars, augmented by the utilization of hydrochar as a precursor of activation, only a couple of studies highlighted the role of HTC conditions on CO_2 uptakes. For example, both Parshetti et al. [142] and Guangzhi et al. [139] concluded the favorability of an HTC temperature of 240–250 °C as those hydrochars resulted in surface roughness, high C content, and C-groups that resulted in superior activated hydrochar properties (diverse functionalities and largest microporosity). However, despite preliminary research of different activated hydrochars as adsorbent materials revealing different adsorption capacities, which mostly stemmed from the combined effect of the different quantity and type of functional groups present in the adsorbent as well as the favorable surface porosity discussed above, it also consolidates the existing research gap of assessing the effect of other HTC conditions on porosity and functionality and determining the true dominating factor, either surface porosity or chemistry, for the performance of CO_2 adsorption.

The fitting of adsorption isotherms to various models demonstrated the Toth isotherm model to describe adsorption accurately at lower and higher pressure [140] where Freundlich was demonstrated to be a great fit for adsorption isotherms in the low to high temperature range (0, 25, and 50 °C) at atmospheric pressure [120,140,142]. The Toth model factor lay between $0.5 < n_t \leq 1.5$ whereas the value of 'n_F' in the Freundlich model was higher than 1 and lying in the range of $1 < n_F < 10$ [120,138,142]. A greater fit to these models can be combinedly said to hint at the possibility of the favorable multilayer physical adsorption mechanism of CO_2 within the surface of the activated hydrochar along with interaction between adsorbed CO_2 molecules. However, similarly, the mechanism of adsorption due to surface doping is hence warranted. Moreover, from the thermodynamic perspective, the nature of the interplay of CO_2 as the adsorbate and porous activated hydrochar as adsorbent is reflected in the heat of adsorption where the relatively lower range of 19–24 kJ/mol [128,131,142,143] signifies the promising possibility of such porous activated hydrochars as competitive adsorbents in CCS (Carbon Capture and Storage) applications. Moreover, the heat of adsorption is also affected by N-doping where a higher heat of adsorption 30.7–44 kJ/mol [129,130] has been reported, which highlights employing such N-rich adsorbents for CO_2 removal from a dilute stream, whereas the values are way below the energy of covalent bonds for chemisorption which makes an energy penalty during desorption.

Table 5. Greenhouse gas adsorption by hydrochar.

CO_2									
Precursor	**Activation/ Modification**	**Carbonization Condition (Temp/Time)**	**Activation Condition (Temp/Time)**	**BET SSA (m^2/g)**	**V_T (cm^3/g)**	**V_u (cm^3/g)**	**Gas Uptake (mmol/g)**	**Favorable Feature**	**Ref.**
Sawdust	KOH Activation	250/2	600/1	1260	0.62	0.52	4.8	Bimodal pores in micro–mesopore range	[118]
Empty Fruit Branch from Oil Palm	KOH Activation	150–350/0.33	800/0.5	2510	1.05	0.55	3.71	High and diverse distribution of functional groups, large specific surface area and micropore volume	[142]
Jujun Grass	KOH Activation	250/2	700/1	3144	1.56	1.23	4.1	High surface area, highly microporous (95% of surface area and 84% of pore volume)	[121]
Camellia Japonica	KOH Activation	250/2	700/1	1353	0.67	0.56	5.0		
Potato Starch	MelamineandKOH Activation	250/2	800/1	3000	1.41	1.09	2.8	Narrow microporosity in the microporous carbons	[127]
Cellulose	Melamine and KOH Activation	250/2	800/1	3100	1.46	1.05	2.8		
Eucalyptus Sawdust	Melamine and KOH Activation	250/2	800/1	3420	2.30	1.16	2.2		

Table 5. *Cont.*

CO_2									
Camphor Leaves	KOH Activation	180–300/5	800/1	1633	0.98	0.58	0.8	Large specific surface area	[139]
Micro Algae	K_2CO_3 Activation	180/10	700/2	1396	0.75	0.59	4.2	Ultra-micropores and a polar surface of heteroatom-containing (e.g., O, N) species	[122]
			800/4	1904	1.08	0.46	3.5		
Lotus Stem	KOH Activation	180/24	800/1	2091	0.87	0.65	3.85	Microporosity and micropore size distribution.	[123]
Garlic Peel	KOH Activation	200/2 (4)	700/1	1248	0.68	0.52	4.2	High microporosity (up to 98%)	[128, 144]
Rice Husk	KOH Activation	200/6	700/1	1190	0.77	0.42	4.48	Ultra-micropores (centered at 0.37 nm and 0.53 nm)	[124]
Pineapple Waste	$K_2C_2O_4$ $Na_2C_2O_4$ $Li_2C_2O_4$	210/10	700/2	1076	0.49	-	1.59–4.25	High surface area and micropores, pyrrolic-/pyridinic-N functional groups	[145]
Tobacco Stalk	N_2 pyrolysis	220/6	700/1	2145	1.00	0.683	4.83	Nitrogen content and micropore volume	[129]
Glucose	KOH activation	180/12	700/1	2659	1.40	1.21	4.24	Narrow micropores volume	[130]
Corn Cob	KOH/$ZnCl_2$/H_3PO_4 activation	230/8	600/1	1222	0.711	0.620	4.5 #	High surface area and pore volume	[140]
CH_4									
Precursor	**Activation/ Modification**	**Carbonization Condition**	**Adsorption Condition**	**BET SSA (m^2/g)**	**V_T (cm^3/g)**	**V_u (cm^3/g)**	**Gas Uptake (mmol/g)**	**Favorable Feature**	**Ref.**
Cellulose	Agent: 50 wt% $ZnCl_2$ solution	250 °C, 3 h,	298 K, 36.5 bar	383–1293	0.27–0.87	0.24–0.43	6.42	High V_{micro}/V_{total} ratio, suitable average pore diameter, specific surface area	[146]
	N_2 flow of 250 mL/min for 1 h	200 °C, 24 h	273 K, 1 bar	416	-	-	1.25	Unfavored by Si and Fe doping	[147]
Sucrose	Temperature: 500, 600, 700, 800°C	190 °C, 5 h	298 K, 10 bar	1375–2431	0.63–1.14	0.58–0.90	90 * (v/v)	High packing densities (~0.9 g cm^{-3}), high surface area and micropore sizes (0.8 nm)	[148]
Starch	Agent/Precursor: 0.5, 1, 1.5	190 °C, 6 h	298 K, 20 bar	3350	1.75	1.10	10.7	Large specific surface area and micropore volume	[149]
Glucose	Agent: K_2CO_3 and KOH	In situ doping with 5 wt% Fe_2O_3 or 5 wt% SiO_2	273 K, 1 bar	576–1549	0.23–0.62	0.20–0.55	3.38	Largest ultra-micropore volume and pore size distributed within 0.4–0.7 nm.	[126]

adsorption at 15 °C; * volumetric CH_4 uptake capacity (v/v); SSA: Specific surface area; V_T: Total pore volume; V_u: Micropore volume.

2.3.2. CH_4 Adsorption

As tabulated in Table 5, CH_4 uptake is reviewed to be demonstrated at 273–298 K both at low (1 bar) and high pressure (up to 36.5 bar) in model compound derived hydrochars which underwent varied post-HTC treatment, ranging from activation with $ZnCl_2$, K_2CO_3, and KOH to pyrolysis using N_2, CO_2, and NH_3. Considering the critical molecular size of CH_4 to be 0.38 nm, it can be speculated that CH_4 is more prone to be adsorbed in a double layer fashion [148]. In terms of surface porosity, CH_4 uptake at low pressure is favored by narrow micropore size distribution where monomodal size distribution centered below 0.8 nm (0.4–0.7 nm) enhances CH_4 adsorption [126,148]. It is also supported by simulation of CH_4 adsorption on an ideal porous graphite, which revealed the optimum pore size to be 0.8 nm for the highest density of CH_4 adsorbed where theoretically 7 mmol g^{-1} could be adsorbed at 1000 kPa [150]. On the other hand, a large surface area in addition to considerable micropore volume favors methane uptake at high pressure [147,151,152].

For example, Correa et al. [153] similarly derived a high adsorption capacity of methane 4.5 mmol/g at 16 bar in the produced activated hydrochars with the increased BET surface area of 1351 m^2/g and a micropore volume of 0.42 cm^3/g. Moreover, high packing density is also a considerable factor to enhance the volumetric uptake of CH_4 [148].

Adsorption isotherm modelling by Pourebrahimi et al. [146] highlighted the possibility of methane adsorption to be cooperative adsorption with the heterogeneity of such activated hydrochars' surface expressed through the isotherm fitting of the Freundlich model. However, the three-parameter Sips model, a combination of Langmuir and Freundlich models, was demonstrated to be a better fit ($R^2 > 0.99$) in the same study, possibly reflecting both mono and multi-layer adsorption. Unfortunately, in another study of F. Liu et al. [126], the authors only applied a Sips model to fit adsorption isotherms without the correlation coefficient mentioned, and rather compared the affinity constant b (kPa^{-1}) for adsorbate–adsorbent interaction in cases of CH_4 and N_2 to establish superior selectivity of methane in the activated hydrochars. From the thermodynamics perspective, the heat of adsorption ranges from 11 to 17 kJ/mol, implying the occurrence of physisorption [149]. Additionally, the adsorption heat typically decreases with the increase in CH_4 uptake, revealing that such activated hydrochars' surface is energetically heterogeneous for adsorption of CH_4 [153–155]. Liu et al. [126] revealed the heat of adsorption to be 26–30 kJ/mol which could be ascribed to the phenomenon of both physisorption and some chemisorption occurring, where during the synthesis process, utilization of NH_3 introduced N corresponding to favorable pyrrole-N as the major functional groups on the surface of the activated and $KMNO_4$ treated hydrochars. Conversely, the detrimental effect of mineral doping was revealed by Wedler et al. [147] where Fe doping resulted in the increase of the structural order during subsequent pyrolysis of the doped hydrochars, leading to less accessible adsorption sites on the surface of the char and hence, decreased methane adsorption capacity. However, more investigation on the role of surface porosity and functionality, heteroatom, and mineral constituents' composition in methane uptake capacity for activated hydrochars is thus warranted, with the necessity of assessing the effect of various HTC process conditions on its derived activated hydrochars' characteristics.

2.4. Hydrochar as Catalyst Support

Research has highlighted the potential use of a biomass-derived carbon-catalyst reaction where the carbon can be synthesized via HTC technique, resulting in hydrochar with active polar oxygenated functionalities [156]. Hydrochars are hence observed to be employed as a catalyst support in the heterogeneous catalysts, as listed in Table 6. However, for its role as an acidic catalyst, the key step to improve the acidic sites on carbon is achieved when the carbon is treated with a chemical agent, such as H_3PO_4, H_2SO_4, HCl, or $HClSO_3$ to improve its acidic sites [157,158]. Konwar et al. [159] shed light on the desired characteristics of a solid-acid catalyst which comprise high concentration of acidic sites, stability, and resistance to variations in pressures and temperatures. Hydrochar-derived carbon materials belong to a small group that have at least two of those traits, as is the case for sulfonic groups (–SO_3H) functionalized hydrochar catalysts [160]. Sulfonated amorphous carbon, where the structure consists of -SO_3H groups, presents much higher catalytic activity than other solid acid catalysts, providing feasibility in applications, such as biodiesel production [161]. Similarly, sulfonated catalysts derived via HTC have also been utilized for isomerization and hydrolysis, as referenced in the Table 6.

In the case of sulfonated catalysts, surface porosity, including surface area, influences the catalytic activity as it indicates the number of active sites for an active group to anchor onto the carbon structure [162]. From the study [163], they found a large quantity of the SO_3H group were able to be incorporated into the carbon lattice due to the meso- and macroporous structure of the catalyst. Although the sulfonation process decreases pore volume and pore size from 0.57 cm^3/g to 0.51 cm^3/g and 53–44 nm, respectively, higher than normal sulfonated glucose acid density can be obtained due to the bimodal porosity of the catalyst [164]. The porosity of the carbon material plays a significant role in anchoring

the sulfonic group, thus affecting the catalytic activity of the sulfonated catalyst [165]. Therefore, in order to produce an excellent catalyst, the porosity of the carbon catalyst must not be taken for granted as it has a momentous impact on the catalytic performance. On the other hand, the stability of such catalysts can be controlled by tuning the carbon particle size of the catalyst. Decreasing the carbon particle size of the catalyst could increase the effectiveness of the sulfonation process and stability by improving contact between carbon particle surfaces with H_2SO_4 [165].

Apart from the sulfonated catalysts, carbonaceous catalysts consisting of transition metals (Cu, Co, Ni, Fe, etc.) and N coordination sites (N-doping) have also attracted attention as a substitute for Pt catalysts in the oxygen reduction reaction (ORR), oxidation, and desulfurization process. The utilization of Fe is advantageous, as standalone hydrochars show poor catalytic activity, whereas carbon-based materials prepared with $FeCl_3$ show the highest catalytic activity [166]. Hydrochar's applicability as a support for such heterogenous catalysts is also attributed to its enhanced metal dispersion ability, and the mutual reaction of metal with the carbon owing to its various surface oxygen-containing functionalities like hydroxyl, carboxyl, carbonyl, and lactone [167]. Such functionalities help enhance access of metal solutions into the hydrochar's carbonaceous matrix as well as providing anchorage sites for the metal that can act as the active centers while functioning as catalysts [168]. In addition, hydrochar's hydrophobicity provides excellent stability while confirming uniform metal dispersion, as observed by Ge at al. [169]. From Table 6, Chen et al. [170] derived thiourea-Fe$(NO_3)_3$-activated hydrochar and found that it offered a large surface area, pore volume, and other favorable surface functionalities (N and S functional groups) which improve complexation and electrostatic interaction for effective As(V) removal. Ma et al. [171] demonstrated that lignin-derived Fe-hydrochar could completely degrade phenol via its catalytic oxidation and exhibited stability upon three runs of regeneration. Moreover, as the hydrochar surface presents a higher degree of aromatization with plentiful oxygen-containing groups, it was conclusive to favor adsorption and degradation of organic pollutants [172]. For example, Dang et al. [173] correlated a lower HTC temperature to result in more abundant oxygen-containing functional groups. This increase of oxygen-containing functional groups generates more free radicals due to the presence of increased reactive–active moieties (RAMs) that could enhance DDT adsorption by providing more react sites for DDT adsorption. Another non-noble based catalyst is nickel-based, which is used for dry reforming of methane. Here, the hydrochar support is advantageous because of the core-shell structure that limits active metal sintering and hence, prevents carbon deposition. Han et al. [174] utilized sugarcane bagasse and revealed that nickel-based catalysts have excellent CH_4 and CO_2 conversions at 80.3% and 90.3%, respectively, at 850 °C. On the other hand, heteroatom doping, particularly by nitrogen, has the ability to create new defects, resulting in more active sites in the carbon matrix. This consequently enhance electrocatalytic activity during cases of ORR and oxygen evolution reaction (OER) [175,176]. Specifically, N-doping results in the transfer of a charge from carbon atoms to adjacent nitrogen atoms that can lead to redistribution of the electronic and spin culture of the sp^2-hybridized carbon framework [177–179]. For example, Yu et al. [180] mediated nitrogen atoms in hydrochar that enhanced catalytic degradation of bisphenol A, bisphenol F, estrone, and 17β-estradiol where a higher surface area of hydrochar and graphitic-N species proved to be favorable. Similarly, the benefit of N-doping was demonstrated by Qiao et al. [181] where N-doping in the amorphous carbon structures could enhance ORR activity by creating nitrogenated active sites which promote electron transfer and also aid in protecting the Fe-derived active sites from catalyst poisoning by the byproducts of ORR reactions.

Another category of hydrochar-based catalyst being developed is composite photocatalysts where high charge transfer efficiency, high photocatalytic reaction, and excellent stability can be attained [182]. This is because the carbonaceous char can serve as an excellent electron bridge due to its large aromatic skeleton, abundant functional groups, good electronic conductivity, and environmental benignity [183]. The added bonus of hydrochar

is the extra oxygen-containing functional groups, as mentioned before, which can act as an electron shuttle in photocatalysts that promote electron transfer while generating a greater number of oxygen reactive species by reacting with the hydration layer that promotes interfacial catalytic reaction. For example, Li et al. [182] concluded excellent photocatalytic activity in carbamazepine removal by microsphere-like hydrochar-based photocatalyst derived from glucose. Another type of photocatalyst is carbon dots (CD) produced via hydrothermal methods, which is beyond the scope of this manuscript.

In summary, as hydrochar catalyst support emerges and demonstrates versatile application in various fields, there is an opportunity of investigating tuning hydrochar's particle size, optimizing transition metal/dopant concentration, and doping of other heteroatoms to assess the effects on surface porosity (SSA, total pore volume and pore size) and functionality, which have been successfully demonstrated to be vital in catalytic activity. It is also imperative to undermine the catalysis mechanism, to identify and reveal the role of active centers, for the applications observed in order to further improve the characteristics of the heterogenous catalyst based on hydrochars by modifying the key constituent (active center) and develop reaction models.

Table 6. Hydrochar as catalyst support.

Feedstock	HTC Process Conditions (Temperature, Time) °C, Hour	SBET (m^2/g)	Dp (nm)	Vp (cm^3/g)	Applications	Reference
Lignin	400, 1	10.7	-	-	Biodiesel production	[184]
Glucose	180, 4	189	2.6	0.19		[185]
Red liquid solid	200, 12	-	-	-		[186]
Chitosan	180, 8	164	1.3	0.35	Esterification reaction	[187]
Acai seed	130, 6	0.70	147	0.06	Esterification reaction (oleic acid and methanol)	[188]
Corncob	200, 10	8.76	29.5	0.07	Esterification (palm fatty acid distillate)	[189]
Cellulose	220,4	626	-	0.17	Glucose isomerization to fructose	[190]
Kenaf core	105, 6	-	-	-	Cellulose hydrolysis	[191]
Glucose	180, 24	-	-	-	Butanolysis of furfuryl alcohol	[192]
Chitosan	200, 12	523		0.49	Catalyst for oxygen reduction reactions	[181]
Chitosan	180, 12	-	-	-	Catalyst for methanol electrooxidation	[193]
Sugarcane, Malt and Chia seed bagasse	200, 3	447	-	0.32	Wet peroxide oxidation of micro-pollutants	[166]
Glucose	180, 10	23.4	-	-	Carbamazepine removal	[182]
Cattle manure	250, 4	33.45	10.9	0.09	As(V) removal	[170]
Gum Tragacanth	180, 2	-	-	-	Phenol removal	[194]
Feedstock	**HTC Process Conditions (Temperature, Time) °C, Hour**	**SBET (m^2/g)**	**Dp (nm)**	**Vp (cm^3/g)**	**Applications**	**Reference**
Lignin (alkali)	200, 18	-	-	-	Phenol removal	[171]
Pinewood sawdust	200, 1	373	6.5	0.25	Biomass steam reforming	[195]
Sugarcane bagasse	240, 10	278	14.7	0.28	Dry Reforming of Methane and Carbon Dioxide	[174]

Table 6. *Cont.*

Feedstock	HTC Process Conditions (Temperature, Time) °C, Hour	SBET (m^2/g)	Dp (nm)	Vp (cm^3/g)	Applications	Reference
Poplar wood	220, 2	1.79	6.59	0.0	Degradation of DDT	[173]
Corn Stalk	240, 3	4.79	1.44	0.02	Degradation of cellulose	[196]
Watermelon peel, banana peel and bay leaves	240, 1	5.15	46.9	0.009	Degradation of malachite green	[197]
Pinewood	180, 24 (annealing for N-doping: 600 °C, 1 h, N_2 atmosphere)	263	11.0	0.106	Degradation of Endocrine Disrupting Compounds (bisphenol A, bisphenol F, estrone, and 17β-estradiol)	[180]
Glucose	240, 16	343	3.85	0.169	Reductive amination of benzaldehyde	[198]
Pine sawdust	200, 4	460	3.91	0.25	Catalytic cracking of biomass tar	[199]
Chitosan	180, 10	-	-	-	Catalyst for Ullmann CeN coupling reaction	[200]

2.5. Electrochemical Applications of Hydrochar

Figure 4 shows an overview of hydrochar's application as supercapacitor. As the dependency on energy surges, the importance to resort to renewable resources to meet these demands becomes absolute [201]. Fortunately, researchers have entertained studies demonstrating hydrochar as a high value material for electrochemical devices such as supercapacitors and batteries [202]. Both supercapacitors and batteries serve the purpose in providing energy with supercapacitors providing high power density and batteries supplying high energy density [201].

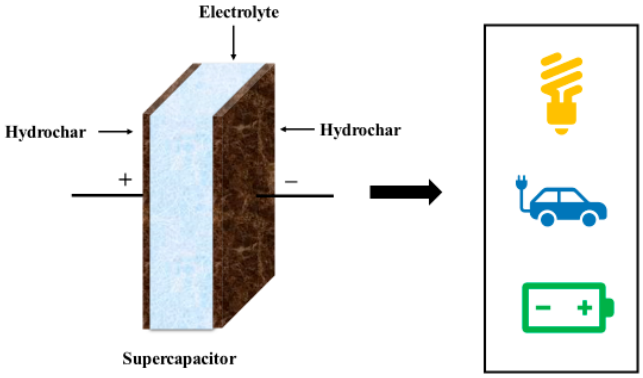

Figure 4. Hydrochar as supercapacitor.

Figure 5 shows a three-dimensional (3D) plot of BET-specific surface area and the pore size of hydrochar for supercapacitors versus the capacitance from recent articles. The 3D plot showed a positive influence of surface porosity of hydrochar as high surface area and micro-meso pore size (<2 nm, 2–50 nm) results in high electron storage. The driving force for excellent supercapacitor performance is owed to the presence of hierarchical porous carbon (micro/meso/macro) which support ionic mass transport, thus maximizing capacitance [203,204]. Fan et al. [205] investigated HTC and activation of alginic acid stable porous hollow carbon spheres (PHCSs). They observed well-balanced micro- and meso-porosity capable of maximum specific capacitance of 314 F/g and excellent electrochemical stability (5000 cycles) [205] (Figure 5). The study ascribed the superior performance to the high specific surface area (2421 m^2/g) and large pore volume (1.61 cm^3/g) [205]. Similarly, Li et al. [206] presented functional porous carbon derived from waste eucalyptus

bark synthesized by hydrothermal treatment combined with KOH activation for toluene adsorption and aqueous symmetric supercapacitors. The findings showed that maximum specific capacitance of 263.2 F/g was attainable with excellent capacitance retention after 10,000 cycles along with high energy and power densities of 10.5 Wh kg^{-1} and 159.5 W $kg^{-1,}$ respectively [206] (Figure 5).

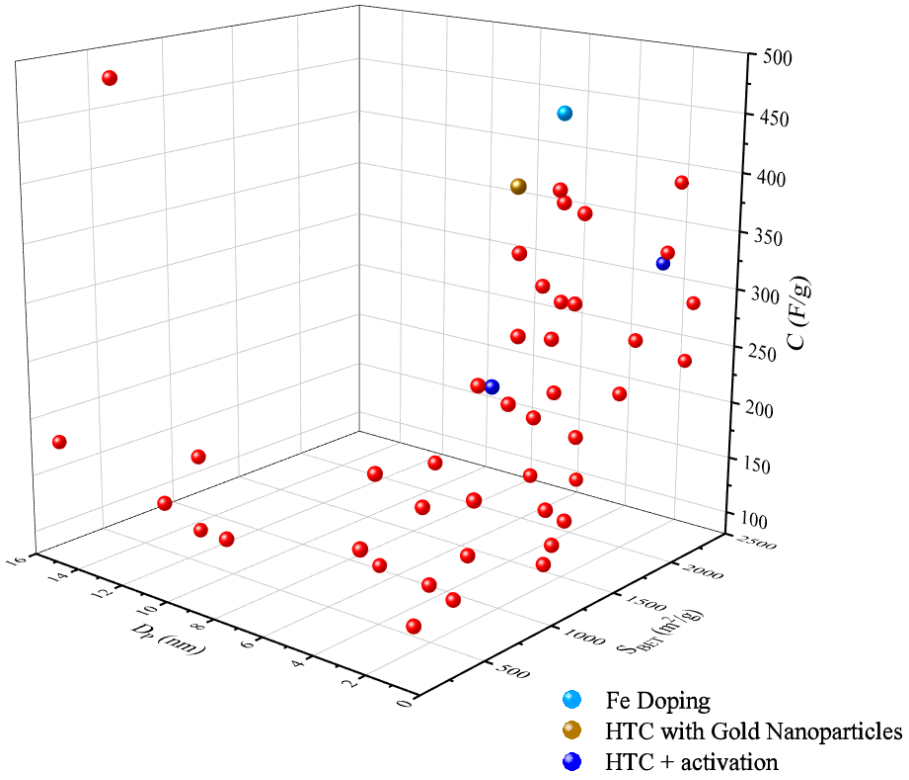

Figure 5. Distribution of the specific capacitance, C (F/g), of hydrochar for supercapacitor application with correlation to the pore size, D_p (nm), and BET-specific surface area, S_{BET} (m^2/g).

Recent studies have shown that improvement in the specific capacitance of hydrochar can be introduced by heteroatom doping the hydrochar to add pseudocapacitance [207,208]. Xu et al. [209] demonstrated the use of Fe-decorated porous carbon derived from bamboo synthesized via HTC with Fe-doping followed by mild chemical activation with $KHCO_3$ for supercapacitor application. The study shows excellent electrochemical performance with maximum specific capacitance of 467 F/g with superb cyclic performance after 5000 cycles and maximum energy density of 20.31 W h kg^{-1} [209] (Figure 5). The performance was attributed to an extra pseudocapacitance supplied from the Fe oxides, sufficient specific surface area (1509.5 m^2/g) with high electric conductivity and the carbon sphere architecture which facilitated better ion/electrolyte diffusion transportation [209]. Similarly, Esteban et al. [210] prepared tunable supercapacitor material via hydrothermal polymerization of glucose-stabilized gold nanoparticles displaying maximum specific capacitance of 436 F/g and energy and power densities of 7.2 Wh kg^{-1} and 24.9 W kg^{-1}, respectively (Figure 5). The performance was due to the synergistic effect of the pore structure after the Au nanoparticles were melted onto the hydrochar along with the well dispersed presence of the Au within the material [210]. Moreover, hydrochar has proved promising as electrode material for electrochemical devices.

2.6. Role of Hydrochar as Soil Amendment and Carbon Sequestration

Figure 6 shows an overview of the application of hydrochar as soil amendment and carbon sequestration. Hydrochar can be considered as environment friendly soil amendment as it slowly releases the nutrient and sequester carbon. Hydrochar showed

promising prospects of water and nutrient storage capacity, which enhances the microbial activity and hence, improves the soil fertility. As a result, the plant growth was positively affected due to applying the hydrochar in the soil.

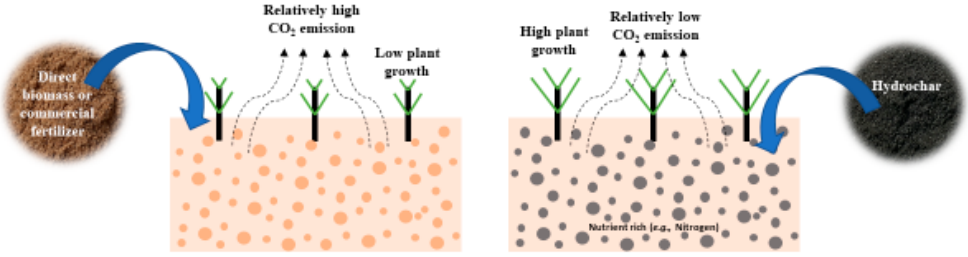

Figure 6. Hydrochar as soil amendment and carbon sequestration application.

Soil amendment on a global scale is becoming an important issue. Applying various ingredients, such as composts, mulches, manure, and organic fertilizer, could enhance soil fertility. However, only a small fraction of these organic compounds may be stabilized for the long term in soil depending on the climatic conditions [211]. On the other hand, hydrochar which contains more stable carbon can be used to promote nutrient acquisition and modify the chemical environment of soil [212,213]. It is also proven that the nitrogen present in hydrochar is not immobilized; rather, it is slowly released over time [212,214–218]. So, hydrochar can be used as soil amendment while slow-release nitrogen fertilizer is required. As the hydrochar is slow release and the organic compounds are fast release, the blends of hydrochar and organic compounds (e.g., animal manure, crop residues) may increase nutrients' availability to the plant [219]. Hydrochar can be a potential source of not only carbon and nitrogen but also humic-like substances which are important for plant growth. For example, Bento et al. [220] found that applying bagasse-derived hydrochar significantly promotes maize seed germination due to the presence of amphiphilic moieties. Now, the question is: how does hydrochar improve the soil properties?

Due to having versatile physiochemical and morphological properties, hydrochar could be a promising soil amendment substance. Table 7 shows the impact of hydrochar as a soil amendment on the solid properties and plant growth rate. For instance, adding hydrochar to the soil enhances the total porosity and water holding capacity [221,222]. Abel et al. [221] found that the water holding capacity increased due to the mixing of 2.5 wt% of corn silage-derived hydrochar with soil. The further addition of hydrochar does not improve the water holding capacity significantly because of the high organic content in hydrochar. A similar finding was observed by Kalderis et al. [223], where the authors reported that the water holding capacity increased until adding 5 wt% of orange peel-derived hydrochar; however, an insignificant change occurred after mixing additional hydrochar. Due to the hydrophobic nature of the hydrochar [220,224,225], the addition of excessive hydrochar in soil could increase the water repellency, resulting in an insignificant improvement of water holding capacity. Addition of hydrochar into the soil ultimately reduces the soil's bulk density as the hydrochar is typically lighter than the soil [221]. In addition to the bulk density, the coarseness index, which describes the particle size distribution may be influenced by the soil–hydrochar mixer. For example, 30% (v/v) of dilution of hydrochar with soil showed the highest coarseness index with the lowest bulk density of the mixer.

Soil's pH is one of the key factors to growing microbial community and plants, as it regulates the ion solubility in the soil [226]. In general, hydrochar is acidic and it becomes more acidic when it is produced at high temperatures [213,223,227,228]. Thus, applying hydrochar can make the soil alkalinity relatively low. Ren et al. [229] found a significant drop in soil pH after mixing the sewage sludge-derived hydrochar, although the hydrochar had lower pH compared to the soil's initial pH. With the initial discrepancy in the pH

between hydrochar and soil, more carboxylic functional groups formed over time due to the oxidation of the hydrochar surface resulting in a lower final pH.

Similar to the pH, electrical conductivity (which determines the level of soil salt content) is another key property of soil. When the salt content in the soil increases, it interrupts the water and nutrient balance which is detrimental to the plant. Belda et al. [230] reported the rising of electrical conductivity about 3-fold by applying 30% forest residue-derived hydrochar into the soil, while a 25% decrease was observed after using sewage sludge-derived hydrochar. The increase in electrical conductivity could be due to the higher organic matters in the forest residue-derived hydrochar compared to the soil, while the reduction could be due to the lower cation exchange capacity and oxygen-to-carbon ratio in the sewage sludge-derived hydrochar [231].

In addition to the soil's physical and chemical properties, hydrochar has the potential to ameliorate the soil's microorganisms as it could deliver essential nutrients and total organic carbons to the soil [213]. Although the potential impact of hydrochar on the microbial community is still in the initial stages, a few studies have found a positive impact of hydrochar on the growth of soil microbes [229,232,233]. For instance, Ren et al. [229] observed a substantial increase in the abundance of Archaea, Bacteria, and Bacillus in the soil after applying hydrochar. There could be several reasons for this increase in microbes. For example, hydrochar contains more organic matter and has a relatively more specific surface area compared to the soil which helps prevent the leaching of bacteria from soil. In contrast, Andert and Mumme [234] reported the adverse effect of hydrochar. For example, the application of hydrochar in soil reduced the Acidobacteria 5-to-6-fold compared to the control, whereas the abundance of Firmicutes was less than one-third. However, the excess of Bacteroidetes and Proteobacteria increased 2.4 and 1.6–1.7 times, respectively. The shift in this microbial community could be due to the easily degradable carbon and low pH of hydrochar. It also observed that the utilization of hydrochar derived from two different feedstocks had different effects on the soil microorganism community. For example, the abundance of ectomycorrhizal fungi was higher when paper mill biosludge-derived hydrochar was applied [235], whereas a negative effect was observed when spent brewer's yeast-derived hydrochar was applied [236]. The probable cause of this different behavior could not only be due to the pH but also the physical and chemical properties, nutrients, and phytotoxicity of hydrochar.

The presence of high aliphatic and less aromatic carbon accelerated microbial degradation made the hydrochar less stable in soil compared to biochar [237,238]. It was also reported that the presence of high hydrophilic (e.g., hydroxyl, carbonyl, and carboxyl) functional groups, low C/N ratio, and low lignin content in the raw material enhance the degradability of the hydrochar [239]. However, a study by Schulze et al. [240] found that instead of lignin content, the reaction temperature and time are more important in determining the hydrochar stability. It has been noticed that higher reaction temperature led to improving the hydrochar stability by increasing the carbon content. Contrariwise, Malghani et al. [22] concluded that corn silage-based hydrochar protects the soil carbon from decomposition as the carbon presence in hydrochar gradually stabilizes after initial rapid decomposition [241,242]. It has been found that applying hydrochar along with fertilizer can generate noticeable greenhouse gas (GHG) emissions [230,234,243,244]. On the other hand, Yu et al. [245] found that hydrochar can reduce GHG emissions by avoiding the composting of fresh biowaste. Similarly, Adjuik et al. [246] concluded that the utilization of hydrochar as a soil amendment did not significantly improve the crop yield; instead, it reduced the soil GHG fluxes by about 34%.

Overall, hydrochar application in soil showed a positive effect on soil aggregation, as a result, it has a good potential for carbon sequestration [236,247,248]. In addition, this potential application could be further improved by removing (washing the hydrochar before using it) the superficially adsorbed labile components (responsible for biological decomposition) from the hydrochar [249].

Table 7. Impact on solid properties and plant growth after applying the hydrohcar as soil amendment.

Hydrochar Feedstock	Usage Rate	Impact on Soil Properties	Crop Type	Crop Response	Ref.
Poultry litter	0.5%, 1.0% (*w*/*w*)	Improved soil water retention Acted as a slow-release fertilizer Decreased nitrate leaching	Lettuce	Improved plant growth up to 3-fold	[222]
Sawdust	5%, 15% (*w*/*w*)	Reduced N_2O emissions	Rice	Increased grain yield by 16.6–19.3%	[244]
Digestate	100 kg N/ha	Hydrochar treatment reduced mean CO_2 emissions	Miscanthus	No change in the crop yield	[246]
Sewage sludge	5 and 25 ton/ha	Application of low temperature derived hydrochar showed nitrogen fertilization potential	Perennial ryegrass	Improved biomass production about 70% Usages rate did not significantly alter the biomass production	[215]
Corn silage	9.2 g N/75 kg soil, 30 ton C/ha	Increased soil carbon and nitrogen	Poplar	Positive effect on the biomass productivity	[241,242]
	0.7% (*w*/*w*)	Increased biological nitrogen fixation	Soybean	Increased plant growth about 3.5 times	[217]
	20% (*v*/*v*)	Preserved more native soil C	Wheat and colza	Hydrochar limits plant growth	[22]
Biosolids	50% (*v*/*v*)	Increased porosity and water holding capacity	Perennial ryegrass	Increased production by 184%	[233]
Forest waste	10, 25, 50% (*v*/*v*)	Sequester more carbon Caused nitrogen immobilization	Myrtle and mastic	Increased seed germination up to 18% and decreased stem weight up to 75%	[230]
Miscanthus	14.5 ton/ha	Improved the carbon sequestration potential Reduced ammonia emissions	Perennial ryegrass	Reduced the growth yield about 10%	[248]
	1.45 kg/m^2	Nitrogen and potassium concentrations enriched	Grasses and forbs	Biomass yield was not affected	[216]
Beet-root chips	2% (*w*/*w*)	Reduced nitrogen concentration in soil Increased soil pH	Barley, phaseolus bean, leek	Promoted biomass production	[219]
Poplar	1, 2.5, 5% (*w*/*w*).	Decreased nitrogen availability No effect on metal concentrations	Oat	Reduced biomass production by 14–50%	[218]

2.7. Nutrient Recovery

Organic waste and biomass contain several nutrients which are essential for plants, apart from having a carbonaceous fraction. Among these nutrients, phosphorus, nitrogen, potassium, and calcium are predominantly found in waste biomass [250,251]. In some organic wastes, sodium is also found, which is considered a functional nutrient [252]. While nitrogen-, phosphorus-, and potassium-based fertilizer are manufactured through a chemical process, organic fertilizers are gaining traction for sustainable agricultural applications [250,253]. In the case of organic waste and biomass, thermochemical treatments are common methods for their scalability [4]. Among different nutrients, nitrogen is the most difficult one to recover considering its release into the atmosphere when high temperature treatment is applied [254]. On the other hand, phosphorus recovery is becoming significantly important due to the depletion of the worldwide reserve [255]. Hydrochar production from organic waste using HTC can provide a versatile solution to nutrient recovery from waste streams.

Nutrient recovery through HTC of organic waste can be achieved by two major pathways. The first pathway is to extract the minerals and nutrients from the parent feed which leaves the nutrients in the hydrochar and effluent liquid stream. Between the hydrochar and liquid effluent, hydrochar retains the major fraction of the plant nutrients [256,257]. Some of the nutrients are recovered from liquid streams (especially, most of the K and Na were found in the liquid phase) by chemical or biochemical processes [258–262]. Notably, the char which contains a major fraction of calcium (>50%), phosphorus (>91%), and nitrogen (>26%), can be utilized as soil replenishment, i.e., as biochar [256]. This is a direct method of nutrient recovery from the HTC process and hydrochar. As for the second pathway, it is achieved by using hydrochar as the mean for recovering nutrients from a waste stream (i.e., wastewater) [263]. In this way, hydrochar can be used for not only recovering nutrients but also purifying the effluent by reducing the undesired nutrient release to the atmosphere. Additional nutrient release to the atmosphere may cause eutrophication (i.e., algal bloom) [264]. The pathways for nutrient recovery from hydrochar are shown in Figure 7.

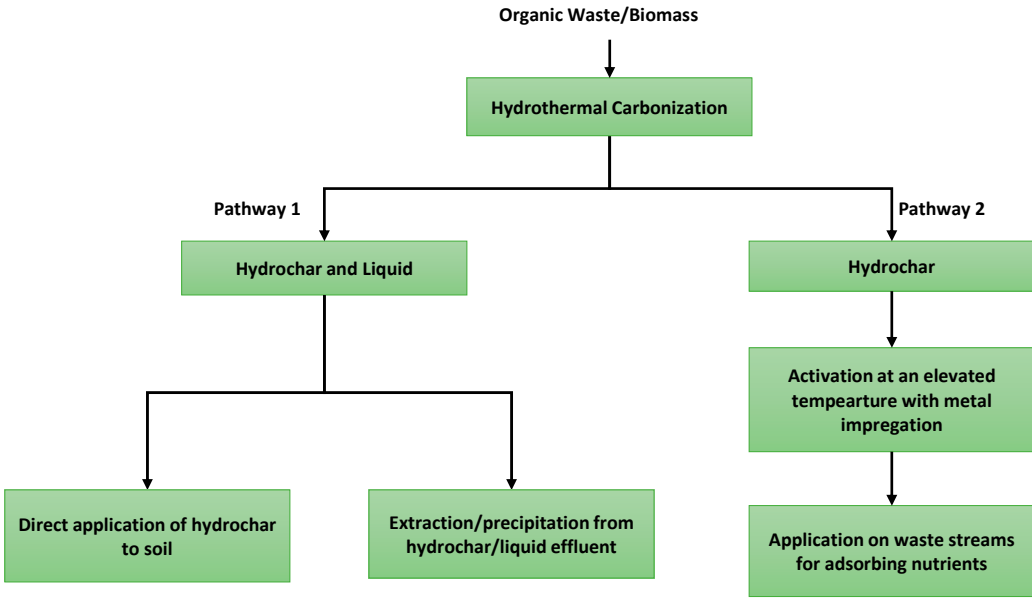

Figure 7. Pathways of nutrient recovery from hydrochar.

While both the methods are promising, the selection of a pathway is highly dependent on the feedstock and application criteria. The feedstock used in HTC may have a variable amount of nutrients and the speciation among different phases (i.e., solid, liquid, and gas) of HTC affects the amount of nutrients recovered [256,265,266]. The macro-nutrients such as nitrogen and phosphorus are usually targeted for recovery while potassium is also available in some feedstock (for pathway 1). For example, if the biochar is generated by pyrolysis (>650 °C) of organic feedstock, the recovery of nitrogen from biochar is not feasible due to its release in the gas phase [267]. As HTC uses low to moderate temperature for treatment, the resulting hydrochar can trap most of the nitrogen [254,256,267,268]. If the organic feedstock is thermochemically converted (i.e., combustion and gasification) at higher temperatures (>600 °C), most of the phosphorus ends up in ash as phosphate complex compounds [255,269]. It is to be noted that if the feedstock does not contain a significant amount of nutrient, pathway 1 would not be a feasible option.

As for pathway 2, recovering nutrients from a waste stream requires hydrochars with a large surface area, good wetting ability, and thermal stability for adsorbing nutrients [270]. In addition, the application of activated hydrochar is suitable if the phosphorus concentration is lower than 2000 mg P/g in the waste stream [271]. One method of increasing the surface is by activating the hydrochar which can increase the surface area by an order of magnitude (>2000 m^2/g of hydrochar) [272,273]. It is to be noted that the pathway 2 is not

limited by the feedstock nutrient content, however, but is dependent on the application media nutrient content and hydrochar properties. Impregnating magnesium and bismuth showed good results in adsorbing phosphorus from the wastewater with a phosphorus recovery varying from 40–125 mg/g of activated char [274,275]. While the advanced methods of hydrochar-based nutrient recovery are promising for recovering nutrients from waste streams, it is still early to determine their practical applicability in a commercial scale. Further studies are necessary for evaluating the techno-economic and environmental feasibility of these techniques.

To utilize the nutrients in the most efficient way, nutrients are to be recovered in an easily absorbable condition for plants. In the case of nitrogen, plants can uptake NO_3^- directly while some NH_4^+ ions can be slowly absorbed [276]. It is to be noted that a portion of the NH_4^+ ions can be hydrolyzed by microorganisms to NO_3^- while a part of it releases as NH_3 to the atmosphere. On the other hand, phosphorus is preferred in phosphate compounds [277]. A typical method to recover phosphorus would be through a struvite precipitation process applicable to only liquid waste streams [278]. For direct applications of hydrochars, the available (i.e., free) phosphorous and nitrogen are critical. The retention of both phosphorus (as phosphate) and nitrogen (as nitrate, which is readily available for release) in the hydrochar at once may be difficult due to their opposing pH requirements for recovery. For example, low pH during HTC favors NH_4^+ ion and free ammonia formation while high pH facilitates the phosphate and gaseous ammonia formation [279]. The gaseous ammonia can be easily released to the atmosphere during the drying of hydrochar [280]. Apart from pH, another important factor for nutrient speciation is temperature during HTC. With the temperature increase, the pH of hydrochar increases by removing the carboxyl and hydroxyl groups [281,282], which indirectly affects the nutrient retention in the char. Moreover, a higher potassium (K) release was favored at a high temperature environment for hydrochar production [281]. As there are interacting parameters affecting the nutrient speciation in hydrochar, optimization is necessary to get to a point where nutrients can be recovered efficiently. Based on HTC experiments performed on anaerobic digestate, Stutzenstein et al. [280] found that the optimum temperature for hydrochar would be 230 °C, sacrificing the nitrogen recovery for the sake of phosphorus recovery (high pH). It is to be noted that the optimum operating parameters will vary with respect to the feedstock as well. As per the study by Dima et al. [256] on municipal solid waste, principal component analysis on several operating conditions yielded a negative impact of time and slightly positive impact of temperature on nutrient recovery in hydrochar. They also reported that potassium (K) and sodium (Na) ended up mostly in the liquid phase. The alkali metals are inorganically bound (as nitrates and chlorides) in the biomass, making them readily soluble in water [283,284].

It is to be remembered that there may be adverse effects in the case of direct application of hydrochar to soil if the free phosphorus is lower than the amount of phosphorus available in the soil. In such a case, it could adsorb phosphorus from the soil on its surface. According to a study by Fei et al. [285] on several types of chars (including hydrochars), up to 417 mg/kg of free phosphorus was available out of the total phosphorus content of 27,175 mg/kg of char. The free phosphorus was still higher than the soil phosphorus content, ensuring its suitability as slow-release fertilizer for the soil. Their study also revealed that P-laden (phosphorus adsorbed on the surface of hydrochar) chars were also suitable for application on soil as well.

Apart from direct application of hydrochar as a nutrient source, there are a few studies on acid leaching of nutrients from hydrochar for application in soil [286,287]. Ekanthalu et al. [287] showed that post-treatment of hydochars after HTC process could leach higher amounts of phosphorus in the liquid phase leading to an easier release to soil. Higher acid concentration provided a better leaching performance of the phosphorus (up to 100%), as expected [286].

Other than recovering nutrients in hydrochar, they could be also used as a means to recover nutrients from wastewater. The mechanism for this process is dependent on the

physico-chemical properties of the hydrochar, which include calcium (Ca) and magnesium (Mg) content along with oxygen containing groups. The presence of Ca and Mg facilitates the capture of phosphorus while NH_4-N is captured by the oxygen functional groups [288]. Although physisorption is not the dominant mechanism in this case, a high surface area facilitates the recovery process [289].

Both hydrochar and nutrient-adsorbed hydrochar are excellent candidates for soil remedying as slow-release fertilizers. However, due to several factors affecting the recovery and application of hydrochar to soil, additional systematic studies are needed for a better understanding of the underlying mechanisms.

3. Conclusions

This review summarized the scattered articles and provided an overview of hydrochar, its modified version, and its applications. Certain observations and recommendations may be made as follows. Increasing the HTC temperature also increases the fuel quality and fuel ratio, which as a result, improves the heating value of the hydrochars towards low-rank coal. In fact, the HTC of combined feedstocks increases the degree of conversion and improves the heating value more. The combustion properties also suggest that hydrochar is more thermally stable than raw feedstocks, which can be further improved by HTC of combined feedstocks. Overall, the HTC of combined feedstocks shows more promising results than the HTC of standalone feedstock.

Hydrochar has demonstrated excellent performance as a catalyst in various applications where catalytic activity is influenced by surface porosity parameters, like surface area, whereas various surface oxygen-containing functionalities of hydrochar help providing anchorage sites to be able to act as the active centers while functioning as catalysts. On the other hand, the oxygen-containing functionalities can also act as an electron shuttle to have demonstrated hydrochar's applicability as photocatalysts. For CO_2 capture, optimum micropore size distribution can be concluded as being 0.5–1.0 nm, where certain surface functionalities seem favorable which include pyridinic-N, amine- or imine-N, pyrrolic-N, quaternary-N, and graphitic-N, which can benefit by establishing a chemisorption effect. On the other hand, monomodal size distribution centered below 0.8 nm and surface groups of pyrrole-N favor CH_4 uptake. Adsorption isotherm models like Toth and Freundlich were demonstrated to be a great fit for CO_2 adsorption isotherms where the Sips model fits CH_4 adsorption isotherms.

Even though pure hydrochar by itself exhibited promising adsorption properties for recurring heavy metals, adding acid, base, and oxidizers produced oxygen-rich functionalities, which eventually started the surface complexation reaction with the metal ions and removed them from the solution. In pristine hydrochar, the adsorption of pharmaceutical toxins is governed by physical attraction, surface area, Van der Waals force, π-π interaction, and hydrogen bonding. However, after modification, the adsorption efficiency significantly increased, with the mechanism being governed by the presence of more oxygen-containing functional groups on the surface.

Hydrochar grants the removal of dye molecules with improved adsorption capacity ranging between 47–5181 mg/g proving efficient uptake capabilities based on the available binding sites. Massive potential of hydrochar as an electrode material has been reported with specific capacitance ranging from 170–495 F/g, as there is more available mesoporous structure which enhances electron.

Hydrochar showed promising prospects of water and nutrient storage capacity. The carbon content and porous structure of hydrochar enhance the microbial activity and hence, improve the soil fertility. As a result, the plant growth was positively affected due to applying the hydrochar in the soil. In addition, as a carbon rich material, hydrochar can be used as a short-term carbon sequestration material. However, extensive studies, such as the reduction of GHG emission, on the fate of organic and inorganic in the soil are required to identity the long-term carbon sequestration potential of hydrochar.

Based on recent studies, it is evident that direct application of hydrochar on soil as a nutrient source could be considered a feasible option for practical application. However, more advanced applications such as nutrient extraction from hydrochar and nutrient recovery from waste streams using activated hydrochar require further assessment before large-scale implementation.

Funding: The material is based upon work partially supported by the United States Department of Agriculture grant number 2019-67019-31594, 2021-67022-34487, and National Science Foundation under Grant No. 2123495.

Data Availability Statement: Not applicable.

Conflicts of Interest: The authors declare no conflict of interest.

References

1. Trash in America. Available online: https://environmentamerica.org/center/resources/trash-in-america-2/ (accessed on 12 September 2022).
2. Ahmed Khan, T.; Kim, H.-J.; Gupta, A.; Jamari, S.S.; Jose, R. Synthesis and Characterization of Carbon Microspheres from Rubber Wood by Hydrothermal Carbonization. *J. Chem. Technol. Biotechnol.* **2019**, *94*, 1374–1383. [CrossRef]
3. Khan, T.A.; Saud, A.S.; Jamari, S.S.; Rahim, M.H.A.; Park, J.-W.; Kim, H.-J. Hydrothermal Carbonization of Lignocellulosic Biomass for Carbon Rich Material Preparation: A Review. *Biomass Bioenergy* **2019**, *130*, 105384. [CrossRef]
4. Kirtania, K. Chapter 4—Thermochemical Conversion Processes for Waste Biorefinery. In *Waste Biorefinery*; Bhaskar, T., Pandey, A., Mohan, S.V., Lee, D.-J., Khanal, S.K., Eds.; Elsevier: Amsterdam, The Netherlands, 2018; pp. 129–156; ISBN 978-0-444-63992-9.
5. Antero, R.V.P.; Alves, A.C.F.; de Oliveira, S.B.; Ojala, S.A.; Brum, S.S. Challenges and Alternatives for the Adequacy of Hydrothermal Carbonization of Lignocellulosic Biomass in Cleaner Production Systems: A Review. *J. Clean. Prod.* **2020**, *252*, 119899. [CrossRef]
6. Shen, Y. A Review on Hydrothermal Carbonization of Biomass and Plastic Wastes to Energy Products. *Biomass Bioenergy* **2020**, *134*, 105479. [CrossRef]
7. Reza, M.T.; Lynam, J.G.; Uddin, M.H.; Coronella, C.J. Hydrothermal Carbonization: Fate of Inorganics. *Biomass Bioenergy* **2013**, *49*, 86–94. [CrossRef]
8. Kruse, A.; Dahmen, N. Hydrothermal Biomass Conversion: Quo Vadis? *J. Supercrit. Fluids* **2018**, *134*, 114–123. [CrossRef]
9. Islam, M.T.; Sultana, A.I.; Saha, N.; Klinger, J.L.; Reza, M.T. Pretreatment of Biomass by Selected Type-III Deep Eutectic Solvents and Evaluation of the Pretreatment Effects on Hydrothermal Carbonization. *Ind. Eng. Chem. Res.* **2021**, *60*, 15479–15491. [CrossRef]
10. Wang, T.; Zhai, Y.; Zhu, Y.; Li, C.; Zeng, G. A Review of the Hydrothermal Carbonization of Biomass Waste for Hydrochar Formation: Process Conditions, Fundamentals, and Physicochemical Properties. *Renew. Sustain. Energy Rev.* **2018**, *90*, 223–247. [CrossRef]
11. Heidari, M.; Dutta, A.; Acharya, B.; Mahmud, S. A Review of the Current Knowledge and Challenges of Hydrothermal Carbonization for Biomass Conversion. *J. Energy Inst.* **2019**, *92*, 1779–1799. [CrossRef]
12. Islam, M.T.; Saha, N.; Hernandez, S.; Klinger, J.; Reza, M.T. Integration of Air Classification and Hydrothermal Carbonization to Enhance Energy Recovery of Corn Stover. *Energies* **2021**, *14*, 1397. [CrossRef]
13. Islam, M.T.; Chambers, C.; Klinger, J.L.; Reza, M.T. Blending Hydrochar Improves Hydrophobic Properties of Corn Stover Pellets. *Biomass Conv. Bioref.* **2022**, 1–12. [CrossRef]
14. Sultana, A.I.; Reza, M.T. Investigation of Hydrothermal Carbonization and Chemical Activation Process Conditions on Hydrogen Storage in Loblolly Pine-Derived Superactivated Hydrochars. *Int. J. Hydrogen Energy* **2022**, *47*, 26422–26434. [CrossRef]
15. Sevilla, M.; Fuertes, A.B.; Mokaya, R. High Density Hydrogen Storage in Superactivated Carbons from Hydrothermally Carbonized Renewable Organic Materials. *Energy Environ. Sci.* **2011**, *4*, 1400–1410. [CrossRef]
16. Islam, M.T.; Chambers, C.; Toufiq Reza, M. Effects of Process Liquid Recirculation on Material Properties of Hydrochar and Corresponding Adsorption of Cationic Dye. *J. Anal. Appl. Pyrolysis* **2022**, *161*, 105418. [CrossRef]
17. Hien Tran, T.; Le, A.H.; Pham, T.H.; Duong, L.D.; Nguyen, X.C.; Nadda, A.K.; Chang, S.W.; Chung, W.J.; Nguyen, D.D.; Nguyen, D.T. A Sustainable, Low-Cost Carbonaceous Hydrochar Adsorbent for Methylene Blue Adsorption Derived from Corncobs. *Environ. Res.* **2022**, *212*, 113178. [CrossRef]
18. Parlavecchia, M.; Carnimeo, C.; Loffredo, E. Soil Amendment with Biochar, Hydrochar and Compost Mitigates the Accumulation of Emerging Pollutants in Rocket Salad Plants. *Water Air Soil Pollut.* **2020**, *231*, 554. [CrossRef]
19. Malool, M.E.; Keshavarz Moraveji, M.; Shayegan, J. Optimized Production, Pb(II) Adsorption and Characterization of Alkali Modified Hydrochar from Sugarcane Bagasse. *Sci. Rep.* **2021**, *11*, 22328. [CrossRef] [PubMed]
20. Tien, B.; Xu, M.; Liu, J. Synthesis and Electrochemical Characterization of Carbon Spheres as Anode Material for Lithium-Ion Battery. *Mater. Lett.* **2010**, *64*, 1465–1467. [CrossRef]
21. Auer, E.; Freund, A.; Pietsch, J.; Tacke, T. Carbons as Supports for Industrial Precious Metal Catalysts. *Appl. Catal. A Gen.* **1998**, *173*, 259–271. [CrossRef]

22. Malghani, S.; Jüschke, E.; Baumert, J.; Thuille, A.; Antonietti, M.; Trumbore, S.; Gleixner, G. Carbon Sequestration Potential of Hydrothermal Carbonization Char (Hydrochar) in Two Contrasting Soils; Results of a 1-Year Field Study. *Biol. Fertil. Soils* **2015**, *51*, 123–134. [CrossRef]
23. Sultana, A.I.; Saha, N.; Reza, M.T. Synopsis of Factors Affecting Hydrogen Storage in Biomass-Derived Activated Carbons. *Sustainability* **2021**, *13*, 1947. [CrossRef]
24. Liu, J.-L.; Qian, W.-C.; Guo, J.-Z.; Shen, Y.; Li, B. Selective Removal of Anionic and Cationic Dyes by Magnetic Fe_3O_4-Loaded Amine-Modified Hydrochar. *Bioresour. Technol.* **2021**, *320*, 124374. [CrossRef] [PubMed]
25. Islam, M.A.; Ahmed, M.J.; Khanday, W.A.; Asif, M.; Hameed, B.H. Mesoporous Activated Coconut Shell-Derived Hydrochar Prepared via Hydrothermal Carbonization-NaOH Activation for Methylene Blue Adsorption. *J. Environ. Manag.* **2017**, *203*, 237–244. [CrossRef] [PubMed]
26. Hou, Z.; Tao, Y.; Bai, T.; Liang, Y.; Huang, S.; Cai, J. Efficient Rhodamine B Removal by N-Doped Hierarchical Carbons Obtained from KOH Activation and Urea-Oxidation of Glucose Hydrochar. *J. Environ. Chem. Eng.* **2021**, *9*, 105757. [CrossRef]
27. Sultana, A.I.; Saha, N.; Reza, M.T. Upcycling Simulated Food Wastes into Superactivated Hydrochar for Remarkable Hydrogen Storage. *J. Anal. Appl. Pyrolysis* **2021**, *159*, 105322. [CrossRef]
28. Sultana, A.I.; Chambers, C.; Ahmed, M.M.N.; Pathirathna, P.; Reza, T. Multifunctional Loblolly Pine-Derived Superactivated Hydrochar: Effect of Hydrothermal Carbonization on Hydrogen and Electron Storage with Carbon Dioxide and Dye Removal. *Nanomaterials* **2022**, *12*, 3575. [CrossRef]
29. Document Search—Web of Science Core Collection. Available online: https://www.webofscience.com/wos/woscc/basic-search (accessed on 22 September 2022).
30. Hoekman, S.K.; Broch, A.; Warren, A.; Felix, L.; Irvin, J. Laboratory Pelletization of Hydrochar from Woody Biomass. *Biofuels* **2014**, *5*, 651–666. [CrossRef]
31. Kambo, H.S.; Dutta, A. Strength, Storage, and Combustion Characteristics of Densified Lignocellulosic Biomass Produced via Torrefaction and Hydrothermal Carbonization. *Appl. Energy* **2014**, *135*, 182–191. [CrossRef]
32. Sadjadi, S.; Karimi, B. Chapter 2—Heteroatom-Doped Carbon Materials Derived from Ionic Liquids for Catalytic Applications. In *Emerging Carbon Materials for Catalysis*; Sadjadi, S., Ed.; Elsevier: Amsterdam, The Netherlands, 2021; pp. 33–72. ISBN 978-0-12-817561-3.
33. Hoekman, S.K.; Broch, A.; Robbins, C. Hydrothermal Carbonization (HTC) of Lignocellulosic Biomass. *Energy Fuels* **2011**, *25*, 1802–1810. [CrossRef]
34. Nizamuddin, S.; Baloch, H.A.; Griffin, G.J.; Mubarak, N.M.; Bhutto, A.W.; Abro, R.; Mazari, S.A.; Ali, B.S. An Overview of Effect of Process Parameters on Hydrothermal Carbonization of Biomass. *Renew. Sustain. Energy Rev.* **2017**, *73*, 1289–1299. [CrossRef]
35. Lynam, J.G.; Reza, M.T.; Yan, W.; Vásquez, V.R.; Coronella, C.J. Hydrothermal Carbonization of Various Lignocellulosic Biomass. *Biomass Conv. Bioref.* **2015**, *5*, 173–181. [CrossRef]
36. Bardhan, M.; Novera, T.M.; Tabassum, M.; Islam, M.A.; Islam, M.A.; Hameed, B.H. Co-Hydrothermal Carbonization of Different Feedstocks to Hydrochar as Potential Energy for the Future World: A Review. *J. Clean. Prod.* **2021**, *298*, 126734. [CrossRef]
37. Saba, A.; Saha, P.; Reza, M.T. Co-Hydrothermal Carbonization of Coal-Biomass Blend: Influence of Temperature on Solid Fuel Properties. *Fuel Process. Technol.* **2017**, *167*, 711–720. [CrossRef]
38. Mumme, J.; Titirici, M.-M.; Pfeiffer, A.; Lüder, U.; Reza, M.T.; Mašek, O. Hydrothermal Carbonization of Digestate in the Presence of Zeolite: Process Efficiency and Composite Properties. *ACS Sustain. Chem. Eng.* **2015**, *3*, 2967–2974. [CrossRef]
39. Xu, Z.; Qi, R.; Zhang, D.; Gao, Y.; Xiong, M.; Chen, W. Co-Hydrothermal Carbonization of Cotton Textile Waste and Polyvinyl Chloride Waste for the Production of Solid Fuel: Interaction Mechanisms and Combustion Behaviors. *J. Clean. Prod.* **2021**, *316*, 128306. [CrossRef]
40. Tekin, K.; Karagöz, S.; Bektaş, S. A Review of Hydrothermal Biomass Processing. *Renew. Sustain. Energy Rev.* **2014**, *40*, 673–687. [CrossRef]
41. Van Krevelen, D.W. *Coal, 3rd ed*; Elsevier: Amsterdam, The Netherlands, 1993; Available online: https://www.elsevier.com/books/coal/van-krevelen/978-0-444-89586-8 (accessed on 13 September 2022).
42. Trif-Tordai, G.; Ionel, I. *Waste Biomass as Alternative Bio-Fuel—Co-Firing versus Direct Combustion*; IntechOpen: Rijeka, Croatia, 2011; ISBN 978-953-307-372-9.
43. Islam, M.T.; Klinger, J.L.; Toufiq Reza, M. Evaluating Combustion Characteristics and Combustion Kinetics of Corn Stover-Derived Hydrochars by Cone Calorimeter. *Chem. Eng. J.* **2022**, *452*, 139419. [CrossRef]
44. Liu, W.; Zheng, X.; Ying, Z.; Feng, Y.; Wang, B.; Dou, B. Hydrochar Prepared from Municipal Sewage Sludge as Renewable Fuels: Evaluation of Its Devolatilization Performance, Reaction Mechanism, and Thermodynamic Property. *J. Environ. Chem. Eng.* **2022**, *10*, 108339. [CrossRef]
45. He, C.; Zhang, Z.; Ge, C.; Liu, W.; Tang, Y.; Zhuang, X.; Qiu, R. Synergistic Effect of Hydrothermal Co-Carbonization of Sewage Sludge with Fruit and Agricultural Wastes on Hydrochar Fuel Quality and Combustion Behavior. *Waste Manag.* **2019**, *100*, 171–181. [CrossRef]
46. Suryaningsih, S.; Nurhilal, O.; Yuliah, Y.; Mulyana, C. Combustion Quality Analysis of Briquettes from Variety of Agricultural Waste as Source of Alternative Fuels. *IOP Conf. Ser. Earth Environ. Sci.* **2017**, *65*, 012012. [CrossRef]
47. Burning of Wood. Available online: http://virtual.vtt.fi/virtual/innofirewood/stateoftheart/database/burning/burning.html (accessed on 25 February 2022).

48. Liu, Z.; Quek, A.; Kent Hoekman, S.; Srinivasan, M.P.; Balasubramanian, R. Thermogravimetric Investigation of Hydrochar-Lignite Co-Combustion. *Bioresour. Technol.* **2012**, *123*, 646–652. [CrossRef] [PubMed]
49. Haykırı-Açma, H. Combustion Characteristics of Different Biomass Materials. *Energy Convers. Manag.* **2003**, *44*, 155–162. [CrossRef]
50. Islam, M.T.; Reza, M.T. Evaluation of Fuel and Combustion Properties of Hydrochar Derived from Co-Hydrothermal Carbonization of Biomass and Plastic. *Biomass Bioenergy*, 2022; *under review*.
51. Lin, Y.; Ge, Y.; Xiao, H.; He, Q.; Wang, W.; Chen, B. Investigation of Hydrothermal Co-Carbonization of Waste Textile with Waste Wood, Waste Paper and Waste Food from Typical Municipal Solid Wastes. *Energy* **2020**, *210*, 118606. [CrossRef]
52. Naderi, M.; Vesali-Naseh, M. Hydrochar-Derived Fuels from Waste Walnut Shell through Hydrothermal Carbonization: Characterization and Effect of Processing Parameters. *Biomass Convers. Bioref.* **2021**, *11*, 1443–1451. [CrossRef]
53. Garrido, R.A.; Lagos, C.; Luna, C.; Sánchez, J.; Díaz, G. Study of the Potential Uses of Hydrochar from Grape Pomace and Walnut Shells Generated from Hydrothermal Carbonization as an Alternative for the Revalorization of Agri-Waste in Chile. *Sustainability* **2021**, *13*, 12600. [CrossRef]
54. Mariuzza, D.; Lin, J.-C.; Volpe, M.; Fiori, L.; Ceylan, S.; Goldfarb, J.L. Impact of Co-Hydrothermal Carbonization of Animal and Agricultural Waste on Hydrochars' Soil Amendment and Solid Fuel Properties. *Biomass Bioenergy* **2022**, *157*, 106329. [CrossRef]
55. Zhang, D.; Wang, F.; Shen, X.; Yi, W.; Li, Z.; Li, Y.; Tian, C. Comparison Study on Fuel Properties of Hydrochars Produced from Corn Stalk and Corn Stalk Digestate. *Energy* **2018**, *165*, 527–536. [CrossRef]
56. Lang, Q.; Guo, Y.; Zheng, Q.; Liu, Z.; Gai, C. Co-Hydrothermal Carbonization of Lignocellulosic Biomass and Swine Manure: Hydrochar Properties and Heavy Metal Transformation Behavior. *Bioresour. Technol.* **2018**, *266*, 242–248. [CrossRef] [PubMed]
57. Nguyen, D.; Zhao, W.; Mäkelä, M.; Alwahabi, Z.T.; Kwong, C.W. Effect of Hydrothermal Carbonisation Temperature on the Ignition Properties of Grape Marc Hydrochar Fuels. *Fuel* **2021**, *313*, 122668. [CrossRef]
58. Basso, D.; Weiss-Hortala, E.; Patuzzi, F.; Baratieri, M.; Fiori, L. In Deep Analysis on the Behavior of Grape Marc Constituents during Hydrothermal Carbonization. *Energies* **2018**, *11*, 1379. [CrossRef]
59. Xue, Y.; Bai, L.; Chi, M.; Xu, X.; Chen, Z.; Yu, K.; Liu, Z. Co-Hydrothermal Carbonization of Pretreatment Lignocellulose Biomass and Polyvinyl Chloride for Clean Solid Fuel Production: Hydrochar Properties and Its Formation Mechanism. *J. Environ. Chem. Eng.* **2022**, *10*, 106975. [CrossRef]
60. Cai, J.; Li, B.; Chen, C.; Wang, J.; Zhao, M.; Zhang, K. Hydrothermal Carbonization of Tobacco Stalk for Fuel Application. *Bioresour. Technol.* **2016**, *220*, 305–311. [CrossRef] [PubMed]
61. Sharma, H.B.; Panigrahi, S.; Dubey, B.K. Hydrothermal Carbonization of Yard Waste for Solid Bio-Fuel Production: Study on Combustion Kinetic, Energy Properties, Grindability and Flowability of Hydrochar. *Waste Manag.* **2019**, *91*, 108–119. [CrossRef] [PubMed]
62. Chen, X.; Ma, X.; Peng, X.; Lin, Y.; Yao, Z. Conversion of Sweet Potato Waste to Solid Fuel via Hydrothermal Carbonization. *Bioresour. Technol.* **2018**, *249*, 900–907. [CrossRef]
63. Areeprasert, C.; Zhao, P.; Ma, D.; Shen, Y.; Yoshikawa, K. Alternative Solid Fuel Production from Paper Sludge Employing Hydrothermal Treatment. *Energy Fuels* **2014**, *28*, 1198–1206. [CrossRef]
64. Maniscalco, M.P.; Volpe, M.; Messineo, A. Hydrothermal Carbonization as a Valuable Tool for Energy and Environmental Applications: A Review. *Energies* **2020**, *13*, 4098. [CrossRef]
65. Tran, H.N.; Huang, F.-C.; Lee, C.-K.; Chao, H.-P. Activated Carbon Derived from Spherical Hydrochar Functionalized with Triethylenetetramine: Synthesis, Characterizations, and Adsorption Application. *Green Process. Synth.* **2017**, *6*, 565–576. [CrossRef]
66. Saha, N.; Volpe, M.; Fiori, L.; Volpe, R.; Messineo, A.; Reza, M.T. Cationic Dye Adsorption on Hydrochars of Winery and Citrus Juice Industries Residues: Performance, Mechanism, and Thermodynamics. *Energies* **2020**, *13*, 4686. [CrossRef]
67. Ferrentino, R.; Ceccato, R.; Marchetti, V.; Andreottola, G.; Fiori, L. Sewage Sludge Hydrochar: An Option for Removal of Methylene Blue from Wastewater. *Appl. Sci.* **2020**, *10*, 3445. [CrossRef]
68. Azzaz, A.A.; Khiari, B.; Jellali, S.; Ghimbeu, C.M.; Jeguirim, M. Hydrochars Production, Characterization and Application for Wastewater Treatment: A Review. *Renew. Sustain. Energy Rev.* **2020**, *127*, 109882. [CrossRef]
69. Zhou, F.; Li, K.; Hang, F.; Zhang, Z.; Chen, P.; Wei, L.; Xie, C. Efficient Removal of Methylene Blue by Activated Hydrochar Prepared by Hydrothermal Carbonization and NaOH Activation of Sugarcane Bagasse and Phosphoric Acid. *RSC Adv.* **2022**, *12*, 1885–1896. [CrossRef] [PubMed]
70. Xu, Q.; Liu, T.; Li, L.; Liu, B.; Wang, X.; Zhang, S.; Li, L.; Wang, B.; Zimmerman, A.R.; Gao, B. Hydrothermal Carbonization of Distillers Grains with Clay Minerals for Enhanced Adsorption of Phosphate and Methylene Blue. *Bioresour. Technol.* **2021**, *340*, 125725. [CrossRef]
71. Tran, T.H.; Le, H.H.; Pham, T.H.; Nguyen, D.T.; La, D.D.; Chang, S.W.; Lee, S.M.; Chung, W.J.; Nguyen, D.D. Comparative Study on Methylene Blue Adsorption Behavior of Coffee Husk-Derived Activated Carbon Materials Prepared Using Hydrothermal and Soaking Methods. *J. Environ. Chem. Eng.* **2021**, *9*, 105362. [CrossRef]
72. Tran, H.N.; You, S.-J.; Chao, H.-P. Fast and Efficient Adsorption of Methylene Green 5 on Activated Carbon Prepared from New Chemical Activation Method. *J. Environ. Manag.* **2017**, *188*, 322–336. [CrossRef] [PubMed]
73. Tabassum, M.; Bardhan, M.; Novera, T.M.; Islam, M.A.; Hadi Jawad, A.; Islam, M.A. NaOH-Activated Betel Nut Husk Hydrochar for Efficient Adsorption of Methylene Blue Dye. *Water Air Soil Pollut.* **2020**, *231*, 398. [CrossRef]

74. Qian, W.-C.; Luo, X.-P.; Wang, X.; Guo, M.; Li, B. Removal of Methylene Blue from Aqueous Solution by Modified Bamboo Hydrochar. *Ecotoxicol. Environ. Saf.* **2018**, *157*, 300–306. [CrossRef]
75. Peng, X.; Yan, Z.; Cheng, X.; Li, Y.; Wang, A.; Chen, L. Quaternary Ammonium-Functionalized Rice Straw Hydrochar as Efficient Adsorbents for Methyl Orange Removal from Aqueous Solution. *Clean Technol. Environ. Policy* **2019**, *21*, 1269–1279. [CrossRef]
76. Madduri, S.; Elsayed, I.; Hassan, E.B. Novel Oxone Treated Hydrochar for the Removal of Pb(II) and Methylene Blue (MB) Dye from Aqueous Solutions. *Chemosphere* **2020**, *260*, 127683. [CrossRef]
77. Lv, B.-W.; Xu, H.; Guo, J.-Z.; Bai, L.-Q.; Li, B. Efficient Adsorption of Methylene Blue on Carboxylate-Rich Hydrochar Prepared by One-Step Hydrothermal Carbonization of Bamboo and Acrylic Acid with Ammonium Persulphate. *J. Hazard. Mater.* **2022**, *421*, 126741. [CrossRef]
78. Liang, Y.; Huang, G.; Zhang, Q.; Yang, Y.; Zhou, J.; Cai, J. Hierarchical Porous Carbons from Biowaste: Hydrothermal Carbonization and High-Performance for Rhodamine B Adsorptive Removal. *J. Mol. Liq.* **2021**, *330*, 115580. [CrossRef]
79. Li, H.-Z.; Zhang, Y.-N.; Guo, J.-Z.; Lv, J.-Q.; Huan, W.-W.; Li, B. Preparation of Hydrochar with High Adsorption Performance for Methylene Blue by Co-Hydrothermal Carbonization of Polyvinyl Chloride and Bamboo. *Bioresour. Technol.* **2021**, *337*, 125442. [CrossRef] [PubMed]
80. Li, F.; Zimmerman, A.R.; Hu, X.; Yu, Z.; Huang, J.; Gao, B. One-Pot Synthesis and Characterization of Engineered Hydrochar by Hydrothermal Carbonization of Biomass with $ZnCl_2$. *Chemosphere* **2020**, *254*, 126866. [CrossRef]
81. Li, B.; Wang, Q.; Guo, J.-Z.; Huan, W.-W.; Liu, L. Sorption of Methyl Orange from Aqueous Solution by Protonated Amine Modified Hydrochar. *Bioresour. Technol.* **2018**, *268*, 454–459. [CrossRef]
82. Li, B.; Lv, J.-Q.; Guo, J.-Z.; Fu, S.-Y.; Guo, M.; Yang, P. The Polyaminocarboxylated Modified Hydrochar for Efficient Capturing Methylene Blue and Cu(II) from Water. *Bioresour. Technol.* **2019**, *275*, 360–367. [CrossRef] [PubMed]
83. Li, B.; Guo, J.; Lv, K.; Fan, J. Adsorption of Methylene Blue and Cd(II) onto Maleylated Modified Hydrochar from Water. *Environ. Pollut.* **2019**, *254*, 113014. [CrossRef]
84. Krishna Murthy, T.P.; Gowrishankar, B.S.; Krishna, R.H.; Chandraprabha, M.N.; Mathew, B.B. Magnetic Modification of Coffee Husk Hydrochar for Adsorptive Removal of Methylene Blue: Isotherms, Kinetics and Thermodynamic Studies. *Environ. Chem. Ecotoxicol.* **2020**, *2*, 205–212. [CrossRef]
85. Hou, Y.; Huang, G.; Li, J.; Yang, Q.; Huang, S.; Cai, J. Hydrothermal Conversion of Bamboo Shoot Shell to Biochar: Preliminary Studies of Adsorption Equilibrium and Kinetics for Rhodamine B Removal. *J. Anal. Appl. Pyrolysis* **2019**, *143*, 104694. [CrossRef]
86. He, C.; Lin, H.; Dai, L.; Qiu, R.; Tang, Y.; Wang, Y.; Duan, P.-G.; Ok, Y.S. Waste Shrimp Shell-Derived Hydrochar as an Emergent Material for Methyl Orange Removal in Aqueous Solutions. *Environ. Int.* **2020**, *134*, 105340. [CrossRef]
87. Duy Nguyen, H.; Nguyen Tran, H.; Chao, H.-P.; Lin, C.-C. Activated Carbons Derived from Teak Sawdust-Hydrochars for Efficient Removal of Methylene Blue, Copper, and Cadmium from Aqueous Solution. *Water* **2019**, *11*, 2581. [CrossRef]
88. Alshareef, S.A.; Otero, M.; Alanazi, H.S.; Siddiqui, M.R.; Khan, M.A.; Alothman, Z.A. Upcycling Olive Oil Cake through Wet Torrefaction to Produce Hydrochar for Water Decontamination. *Chem. Eng. Res. Des.* **2021**, *170*, 13–22. [CrossRef]
89. WHO. *Exposure to Lead: A Major Public Health Concern*, 2nd ed.; WHO: Geneva, Switzerland, 2021. Available online: https://www.who.int/publications-detail-redirect/9789240037656 (accessed on 23 September 2022).
90. Dhaouadi, F.; Sellaoui, L.; Hernández-Hernández, L.E.; Bonilla-Petriciolet, A.; Mendoza-Castillo, D.I.; Reynel-Ávila, H.E.; González-Ponce, H.A.; Taamalli, S.; Louis, F.; Lamine, A.B. Preparation of an Avocado Seed Hydrochar and Its Application as Heavy Metal Adsorbent: Properties and Advanced Statistical Physics Modeling. *Chem. Eng. J.* **2021**, *419*, 129472. [CrossRef]
91. Li, Y.; Tsend, N.; Li, T.; Liu, H.; Yang, R.; Gai, X.; Wang, H.; Shan, S. Microwave Assisted Hydrothermal Preparation of Rice Straw Hydrochars for Adsorption of Organics and Heavy Metals. *Bioresour. Technol.* **2019**, *273*, 136–143. [CrossRef] [PubMed]
92. Xue, Y.; Gao, B.; Yao, Y.; Inyang, M.; Zhang, M.; Zimmerman, A.R.; Ro, K.S. Hydrogen Peroxide Modification Enhances the Ability of Biochar (Hydrochar) Produced from Hydrothermal Carbonization of Peanut Hull to Remove Aqueous Heavy Metals: Batch and Column Tests. *Chem. Eng. J.* **2012**, *200–202*, 673–680. [CrossRef]
93. He, X.; Zhang, T.; Xue, Q.; Zhou, Y.; Wang, H.; Bolan, N.S.; Jiang, R.; Tsang, D.C.W. Enhanced Adsorption of Cu(II) and Zn(II) from Aqueous Solution by Polyethyleneimine Modified Straw Hydrochar. *Sci. Total Environ.* **2021**, *778*, 146116. [CrossRef]
94. Ghanim, B.; Leahy, J.J.; O'Dwyer, T.F.; Kwapinski, W.; Pembroke, J.T.; Murnane, J.G. Removal of Hexavalent Chromium (Cr(VI)) from Aqueous Solution Using Acid-modified Poultry Litter-derived Hydrochar: Adsorption, Regeneration and Reuse. *J. Chem. Technol. Biotechnol.* **2021**, *97*, 55–66. [CrossRef]
95. Luo, X.; Huang, Z.; Lin, J.; Li, X.; Qiu, J.; Liu, J.; Mao, X. Hydrothermal Carbonization of Sewage Sludge and In-Situ Preparation of Hydrochar/MgAl-Layered Double Hydroxides Composites for Adsorption of Pb(II). *J. Clean. Prod.* **2020**, *258*, 120991. [CrossRef]
96. Nadarajah, K.; Bandala, E.R.; Zhang, Z.; Mundree, S.; Goonetilleke, A. Removal of Heavy Metals from Water Using Engineered Hydrochar: Kinetics and Mechanistic Approach. *J. Water Process Eng.* **2021**, *40*, 101929. [CrossRef]
97. Jiang, Q.; Xie, W.; Han, S.; Wang, Y.; Zhang, Y. Enhanced Adsorption of Pb(II) onto Modified Hydrochar by Polyethyleneimine or H3PO4: An Analysis of Surface Property and Interface Mechanism. *Colloids Surf. A Physicochem. Eng. Asp.* **2019**, *583*, 123962. [CrossRef]
98. Khushk, S.; Zhang, L.; Pirzada, A.M.; Irfan, M.; Li, A. *Cr(VI) Heavy Metal Adsorption from Aqueous Solution by KOH Treated Hydrochar Derived from Agricultural Wastes*; AIP Publishing: New York, NY, USA, 2019.
99. Xia, Y.; Yang, T.; Zhu, N.; Li, D.; Chen, Z.; Lang, Q.; Liu, Z.; Jiao, W. Enhanced Adsorption of Pb(II) onto Modified Hydrochar: Modeling and Mechanism Analysis. *Bioresour. Technol.* **2019**, *288*, 121593. [CrossRef]

100. Rocha, L.S.; Pereira, D.; Sousa, É.; Otero, M.; Esteves, V.I.; Calisto, V. Recent Advances on the Development and Application of Magnetic Activated Carbon and Char for the Removal of Pharmaceutical Compounds from Waters: A Review. *Sci. Total Environ.* **2020**, *718*, 137272. [CrossRef] [PubMed]
101. Zenker, A.; Cicero, M.R.; Prestinaci, F.; Bottoni, P.; Carere, M. Bioaccumulation and Biomagnification Potential of Pharmaceuticals with a Focus to the Aquatic Environment. *J. Environ. Manag.* **2014**, *133*, 378–387. [CrossRef] [PubMed]
102. Kimbi Yaah, V.B.; Zbair, M.; Botelho de Oliveira, S.; Ojala, S. Hydrochar-Derived Adsorbent for the Removal of Diclofenac from Aqueous Solution. *Nanotechnol. Environ. Eng.* **2021**, *6*, 3. [CrossRef]
103. Mestre, A.S.; Tyszko, E.; Andrade, M.A.; Galhetas, M.; Freire, C.; Carvalho, A.P. Sustainable Activated Carbons Prepared from a Sucrose-Derived Hydrochar: Remarkable Adsorbents for Pharmaceutical Compounds. *RSC Adv.* **2015**, *5*, 19696–19707. [CrossRef]
104. Larous, S.; Meniai, A.-H. Adsorption of Diclofenac from Aqueous Solution Using Activated Carbon Prepared from Olive Stones. *Int. J. Hydrogen Energy* **2016**, *41*, 10380–10390. [CrossRef]
105. Delgado-Moreno, L.; Bazhari, S.; Gasco, G.; Méndez, A.; El Azzouzi, M.; Romero, E. New Insights into the Efficient Removal of Emerging Contaminants by Biochars and Hydrochars Derived from Olive Oil Wastes. *Sci. Total Environ.* **2021**, *752*, 141838. [CrossRef]
106. Qureshi, T.; Memon, N.; Memon, S.Q.; Yavuz, H.; Lachgar, A.; Denizli, A. Evaluation of Hydrochar Efficiency for Simultaneous Removal of Diclofenac and Ibuprofen from Aqueous System Using Surface Response Methodology. *Environ. Sci. Pollut. Res.* **2019**, *26*, 9796–9804. [CrossRef]
107. Pauletto, P.S.; Moreno-Pérez, J.; Hernández-Hernández, L.E.; Bonilla-Petriciolet, A.; Dotto, G.L.; Salau, N.P.G. Novel Biochar and Hydrochar for the Adsorption of 2-Nitrophenol from Aqueous Solutions: An Approach Using the PVSDM Model. *Chemosphere* **2021**, *269*, 128748. [CrossRef]
108. Sachan, D.; Das, G. Selective Adsorption of Drug Micropollutants from Synthetic Wastewater Using Hydrochar Derived from Carbonisation of Unused Leaves. *Int. J. Environ. Anal. Chem.* **2022**, 1–20. [CrossRef]
109. Liu, Y.; Sun, Y.; Wan, Z.; Jing, F.; Li, Z.; Chen, J.; Tsang, D.C.W. Tailored Design of Food Waste Hydrochar for Efficient Adsorption and Catalytic Degradation of Refractory Organic Contaminant. *J. Clean. Prod.* **2021**, *310*, 127482. [CrossRef]
110. Weidemann, E.; Niinipuu, M.; Fick, J.; Jansson, S. Using Carbonized Low-Cost Materials for Removal of Chemicals of Environmental Concern from Water. *Environ. Sci. Pollut. Res. Int.* **2018**, *25*, 15793–15801. [CrossRef] [PubMed]
111. De Lima, H.H.C.; Llop, M.E.G.; dos Santos Maniezzo, R.; Moisés, M.P.; Janeiro, V.; Arroyo, P.A.; Guilherme, M.R.; Rinaldi, A.W. Enhanced Removal of Bisphenol A Using Pine-Fruit Shell-Derived Hydrochars: Adsorption Mechanisms and Reusability. *J. Hazard. Mater.* **2021**, *416*, 126167. [CrossRef] [PubMed]
112. Huang, H.; Niu, Z.; Shi, R.; Tang, J.; Lv, L.; Wang, J.; Fan, Y. Thermal Oxidation Activation of Hydrochar for Tetracycline Adsorption: The Role of Oxygen Concentration and Temperature. *Bioresour. Technol.* **2020**, *306*, 123096. [CrossRef] [PubMed]
113. De Araújo, T.P.; Quesada, H.B.; Bergamasco, R.; Vareschini, D.T.; de Barros, M.A.S.D. Activated Hydrochar Produced from Brewer's Spent Grain and Its Application in the Removal of Acetaminophen. *Bioresour. Technol.* **2020**, *310*, 123399. [CrossRef] [PubMed]
114. Hagos, F.M.; Qian, H.; Di, J.; Shan, S.; Yang, R.; Li, Y.; Gai, X. Rice Husk Hydrochars Prepared with Different Post-Treatment Methods for the Adsorption of Dyes and Antibiotics. *BioResources* **2021**, *17*, 725–749. [CrossRef]
115. Aghababaei, A.; Azargohar, R.; Dalai, A.K.; Soltan, J.; Niu, C.H. Effective Adsorption of Carbamazepine from Water by Adsorbents Developed from Flax Shives and Oat Hulls: Key Factors and Characterization. *Ind. Crops Prod.* **2021**, *170*, 113721. [CrossRef]
116. Fernandez, M.E.; Ledesma, B.; Román, S.; Bonelli, P.R.; Cukierman, A.L. Development and Characterization of Activated Hydrochars from Orange Peels as Potential Adsorbents for Emerging Organic Contaminants. *Bioresour. Technol.* **2015**, *183*, 221–228. [CrossRef]
117. Oumabady, S.; Selvaraj, P.S.; Periasamy, K.; Veeraswamy, D.; Ramesh, P.T.; Palanisami, T.; Ramasamy, S.P. Kinetic and Isotherm Insights of Diclofenac Removal by Sludge Derived Hydrochar. *Sci. Rep.* **2022**, *12*, 2184. [CrossRef]
118. Sevilla, M.; Fuertes, A.B. Sustainable Porous Carbons with a Superior Performance for CO_2 Capture. *Energy Environ. Sci.* **2011**, *4*, 1765–1771. [CrossRef]
119. Sevilla, M.; Maciá-Agulló, J.A.; Fuertes, A.B. Hydrothermal Carbonization of Biomass as a Route for the Sequestration of CO_2: Chemical and Structural Properties of the Carbonized Products. *Biomass Bioenergy* **2011**, *35*, 3152–3159. [CrossRef]
120. Goel, C.; Mohan, S.; Dinesha, P. CO_2 Capture by Adsorption on Biomass-Derived Activated Char: A Review. *Sci. Total Environ.* **2021**, *798*, 149296. [CrossRef]
121. Matabosch Coromina, H.; Walsh, D.A.; Mokaya, R. Biomass-Derived Activated Carbon with Simultaneously Enhanced CO_2 Uptake for Both Pre and Post Combustion Capture Applications. *J. Mater. Chem. A* **2016**, *4*, 280–289. [CrossRef]
122. Guo, L.-P.; Zhang, Y.; Li, W.-C. Sustainable Microalgae for the Simultaneous Synthesis of Carbon Quantum Dots for Cellular Imaging and Porous Carbon for CO_2 Capture. *J. Colloid Interface Sci.* **2017**, *493*, 257–264. [CrossRef] [PubMed]
123. Wu, X.; Zhang, C.; Tian, Z.; Cai, J. Large-Surface-Area Carbons Derived from Lotus Stem Waste for Efficient CO_2 Capture. *New Carbon Mater.* **2018**, *33*, 252–261. [CrossRef]
124. Liu, X.; Sun, C.; Liu, H.; Tan, W.H.; Wang, W.; Snape, C. Developing Hierarchically Ultra-Micro/Mesoporous Biocarbons for Highly Selective Carbon Dioxide Adsorption. *Chem. Eng. J.* **2019**, *361*, 199–208. [CrossRef]
125. Hong, S.-H.; Chung, K.; Bang, G.; Kim, K.-M.; Lee, C.-H. Adsorption Equilibria and Kinetics of CO2, CH4, CO, N2, and H2 on KOH-Treated Activated Carbon Pellets up to 1000 KPa. *Chem. Eng. J.* **2022**, *431*, 133396. [CrossRef]

126. Liu, F.; Lin, Q.; Fu, C.; Wang, M.; Han, M.; Huang, C.; Pan, H.; Liu, F. Alkaline $KMnO_4$ Solution Pretreat Hydrochar to Prepare High Ultra-Micropore Volume Carbon for CH_4 Enrichment from Low-Concentration Coalbed Methane. *Fuel* **2021**, *303*, 121301. [CrossRef]
127. Sevilla, M.; Sangchoom, W.; Balahmar, N.; Fuertes, A.B.; Mokaya, R. Highly Porous Renewable Carbons for Enhanced Storage of Energy-Related Gases (H_2 and CO_2) at High Pressures. *ACS Sustain. Chem. Eng.* **2016**, *4*, 4710–4716. [CrossRef]
128. Huang, G.; Wu, X.; Hou, Y.; Cai, J. Sustainable Porous Carbons from Garlic Peel Biowaste and KOH Activation with an Excellent CO_2 Adsorption Performance. *Biomass Conv. Bioref.* **2020**, *10*, 267–276. [CrossRef]
129. Huang, F.; Li, D.; Wang, L.; Zhang, K.; Fu, L.; Guo, Z.; Liang, M.; Wang, B.; Luo, D.; Li, B. Rational Introduction of Nitridizing Agent to Hydrothermal Carbonization for Enhancing CO_2 Capture Performance of Tobacco Stalk-Based Porous Carbons. *J. Anal. Appl. Pyrolysis* **2021**, *157*, 105047. [CrossRef]
130. Rao, L.; Ma, R.; Liu, S.; Wang, L.; Wu, Z.; Yang, J.; Hu, X. Nitrogen Enriched Porous Carbons from D-Glucose with Excellent CO_2 Capture Performance. *Chem. Eng. J.* **2019**, *362*, 794–801. [CrossRef]
131. Rouzitalab, Z.; Maklavany, D.M.; Jafarinejad, S.; Rashidi, A. Lignocellulose-Based Adsorbents: A Spotlight Review of the Effective Parameters on Carbon Dioxide Capture Process. *Chemosphere* **2020**, *246*, 125756. [CrossRef]
132. Yang, J.; Yue, L.; Hu, X.; Wang, L.; Zhao, Y.; Lin, Y.; Sun, Y.; DaCosta, H.; Guo, L. Efficient CO_2 Capture by Porous Carbons Derived from Coconut Shell. *Energy Fuels* **2017**, *31*, 4287–4293. [CrossRef]
133. Serafin, J.; Narkiewicz, U.; Morawski, A.W.; Wróbel, R.J.; Michalkiewicz, B. Highly Microporous Activated Carbons from Biomass for CO_2 Capture and Effective Micropores at Different Conditions. *J. CO2 Util.* **2017**, *18*, 73–79. [CrossRef]
134. Bae, J.-S.; Su, S. Macadamia Nut Shell-Derived Carbon Composites for Post Combustion CO_2 Capture. *Int. J. Greenh. Gas Control* **2013**, *19*, 174–182. [CrossRef]
135. Rashidi, A.M.; Kazemi, D.; Izadi, N.; Pourkhalil, M.; Jorsaraei, A.; Ganji, E.; Lotfi, R. Preparation of Nanoporous Activated Carbon and Its Application as Nano Adsorbent for CO_2 Storage. *Korean J. Chem. Eng.* **2016**, *33*, 616–622. [CrossRef]
136. Gopalan, J.; Buthiyappan, A.; Abdul Raman, A.A. Insight into Metal-Impregnated Biomass Based Activated Carbon for Enhanced Carbon Dioxide Adsorption: A Review. *J. Ind. Eng. Chem.* **2022**, *113*, 72–95. [CrossRef]
137. Guo, T.; Tian, W.; Wang, Y. Effect of Pore Structure on CO_2 Adsorption Performance for $ZnCl_2/FeCl_3/H_2O$(g) Co-Activated Walnut Shell-Based Biochar. *Atmosphere* **2022**, *13*, 1110. [CrossRef]
138. Yan, H.; Zhang, G.; Xu, Y.; Zhang, Q.; Liu, J.; Li, G.; Zhao, Y.; Wang, Y.; Zhang, Y. High CO2 Adsorption on Amine-Functionalized Improved Macro-/Mesoporous Multimodal Pore Silica. *Fuel* **2022**, *315*, 123195. [CrossRef]
139. Yang, G.; Ye, J.; Yan, Y.; Tang, Z.; Yu, D.; Yang, J. Preparation and CO_2 Adsorption Properties of Porous Carbon from Camphor Leaves by Hydrothermal Carbonization and Sequential Potassium Hydroxide Activation. *RSC Adv.* **2017**, *7*, 4152–4160. [CrossRef]
140. Sarwar, A.; Ali, M.; Khoja, A.H.; Nawar, A.; Waqas, A.; Liaquat, R.; Naqvi, S.R.; Asjid, M. Synthesis and Characterization of Biomass-Derived Surface-Modified Activated Carbon for Enhanced CO_2 Adsorption. *J. CO2 Util.* **2021**, *46*, 101476. [CrossRef]
141. Jiang, E.; Cheng, S.; Tu, R.; He, Z.; Jia, Z.; Long, X.; Wu, Y.; Sun, Y.; Xu, X. High Yield Self-Nitrogen-Oxygen Doped Hydrochar Derived from Microalgae Carbonization in Bio-Oil: Properties and Potential Applications. *Bioresour. Technol.* **2020**, *314*, 123735. [CrossRef] [PubMed]
142. Parshetti, G.K.; Chowdhury, S.; Balasubramanian, R. Biomass Derived Low-Cost Microporous Adsorbents for Efficient CO_2 Capture. *Fuel* **2015**, *148*, 246–254. [CrossRef]
143. Creamer, A.E.; Gao, B. Carbon-Based Adsorbents for Postcombustion CO_2 Capture: A Critical Review. *Environ. Sci. Technol.* **2016**, *50*, 7276–7289. [CrossRef] [PubMed]
144. Huang, G.; Liu, Y.; Wu, X.; Cai, J. Activated Carbons Prepared by the KOH Activation of a Hydrochar from Garlic Peel and Their CO_2 Adsorption Performance. *New Carbon Mater.* **2019**, *34*, 247–257. [CrossRef]
145. Zhu, M.; Cai, W.; Verpoort, F.; Zhou, J. Preparation of Pineapple Waste-Derived Porous Carbons with Enhanced CO_2 Capture Performance by Hydrothermal Carbonation-Alkali Metal Oxalates Assisted Thermal Activation Process. *Chem. Eng. Res. Des.* **2019**, *146*, 130–140. [CrossRef]
146. Pourebrahimi, S.; Kazemeini, M.; Zaroudi, M.; Bozorgzadeh, H. Methane Adsorption on Carbonaceous Microporous Materials Prepared from Cellulose and Lignin: Equilibrium and Kinetic Studies. *Sci. Iran.* **2018**, *25*, 3368–3380. [CrossRef]
147. Wedler, C.; Lotz, K.; Arami-Niya, A.; Xiao, G.; Span, R.; Muhler, M.; May, E.F.; Richter, M. Influence of Mineral Composition of Chars Derived by Hydrothermal Carbonization on Sorption Behavior of CO_2, CH_4, and O_2. *ACS Omega* **2020**, *5*, 10704–10714. [CrossRef]
148. Mestre, A.S.; Freire, C.; Pires, J.; Carvalho, A.P.; Pinto, M.L. High Performance Microspherical Activated Carbons for Methane Storage and Landfill Gas or Biogas Upgrade. *J. Mater. Chem. A* **2014**, *2*, 15337–15344. [CrossRef]
149. Li, Y.; Li, D.; Rao, Y.; Zhao, X.; Wu, M. Superior CO_2, CH_4, and H_2 Uptakes over Ultrahigh-Surface-Area Carbon Spheres Prepared from Sustainable Biomass-Derived Char by CO_2 Activation. *Carbon* **2016**, *105*, 454–462. [CrossRef]
150. Qiu, D.; Guo, N.; Gao, A.; Zheng, L.; Xu, W.; Li, M.; Wang, F.; Yang, R. Preparation of Oxygen-Enriched Hierarchically Porous Carbon by $KMnO_4$ One-Pot Oxidation and Activation: Mechanism and Capacitive Energy Storage. *Electrochim. Acta* **2019**, *294*, 398–405. [CrossRef]
151. Feng, Y.-Y.; Yang, W.; Chu, W. K_2S-Activated Carbons Developed from Coal and Their Methane Adsorption Behaviors. *Chin. Phys. B* **2014**, *23*, 108201. [CrossRef]

152. Cai, J.; Qi, J.; Yang, C.; Zhao, X. Poly(Vinylidene Chloride)-Based Carbon with Ultrahigh Microporosity and Outstanding Performance for CH_4 and H_2 Storage and CO_2 Capture. *ACS Appl. Mater. Interfaces* **2014**, *6*, 3703–3711. [CrossRef] [PubMed]
153. Rodriguez Correa, C.; Bernardo, M.; Ribeiro, R.P.P.L.; Esteves, I.A.A.C.; Kruse, A. Evaluation of Hydrothermal Carbonization as a Preliminary Step for the Production of Functional Materials from Biogas Digestate. *J. Anal. Appl. Pyrolysis* **2017**, *124*, 461–474. [CrossRef]
154. Physisorption and Chemisorption—Definition, Mechanism, Differences. Available online: https://byjus.com/jee/physisorption-and-chemisorption/ (accessed on 6 December 2022).
155. De Oliveira, L.H.; Meneguin, J.G.; Pereira, M.V.; do Nascimento, J.F.; Arroyo, P.A. Adsorption of Hydrogen Sulfide, Carbon Dioxide, Methane, and Their Mixtures on Activated Carbon. *Chem. Eng. Commun.* **2019**, *206*, 1533–1553. [CrossRef]
156. Titirici, M.-M.; Antonietti, M. Chemistry and Materials Options of Sustainable Carbon Materials Made by Hydrothermal Carbonization. *Chem. Soc. Rev.* **2010**, *39*, 103–116. [CrossRef]
157. Abdulkareem-Alsultan, G.; Asikin-Mijan, N.; Lee, H.V.; Taufiq-Yap, Y.H. A New Route for the Synthesis of La-Ca Oxide Supported on Nano Activated Carbon via Vacuum Impregnation Method for One Pot Esterification-Transesterification Reaction. *Chem. Eng. J.* **2016**, *304*, 61–71. [CrossRef]
158. Soltani, S.; Rashid, U.; Yunus, R.; Taufiq-Yap, Y.H. Biodiesel Production in the Presence of Sulfonated Mesoporous $ZnAl_2O_4$ Catalyst via Esterification of Palm Fatty Acid Distillate (PFAD). *Fuel* **2016**, *178*, 253–262. [CrossRef]
159. Konwar, L.J.; Mäki-Arvela, P.; Mikkola, J.-P. SO_3H-Containing Functional Carbon Materials: Synthesis, Structure, and Acid Catalysis. *Chem. Rev.* **2019**, *119*, 11576–11630. [CrossRef]
160. Zailan, Z.; Tahir, M.; Jusoh, M.; Zakaria, Z.Y. A Review of Sulfonic Group Bearing Porous Carbon Catalyst for Biodiesel Production. *Renew. Energy* **2021**, *175*, 430–452. [CrossRef]
161. Chen, G.; Fang, B. Preparation of Solid Acid Catalyst from Glucose–Starch Mixture for Biodiesel Production. *Bioresour. Technol.* **2011**, *102*, 2635–2640. [CrossRef] [PubMed]
162. Ning, Y.; Niu, S. Preparation and Catalytic Performance in Esterification of a Bamboo-Based Heterogeneous Acid Catalyst with Microwave Assistance. *Energy Convers. Manag.* **2017**, *153*, 446–454. [CrossRef]
163. Lokman, I.M.; Rashid, U.; Taufiq-Yap, Y.H. Meso- and Macroporous Sulfonated Starch Solid Acid Catalyst for Esterification of Palm Fatty Acid Distillate. *Arab. J. Chem.* **2016**, *9*, 179–189. [CrossRef]
164. Okamura, M.; Takagaki, A.; Toda, M.; Kondo, J.N.; Domen, K.; Tatsumi, T.; Hara, M.; Hayashi, S. Acid-Catalyzed Reactions on Flexible Polycyclic Aromatic Carbon in Amorphous Carbon. *Chem. Mater.* **2006**, *18*, 3039–3045. [CrossRef]
165. Tamborini, L.H.; Casco, M.E.; Militello, M.P.; Silvestre-Albero, J.; Barbero, C.A.; Acevedo, D.F. Sulfonated Porous Carbon Catalysts for Biodiesel Production: Clear Effect of the Carbon Particle Size on the Catalyst Synthesis and Properties. *Fuel Process. Technol.* **2016**, *149*, 209–217. [CrossRef]
166. Diaz de Tuesta, J.L.; Saviotti, M.C.; Roman, F.F.; Pantuzza, G.F.; Sartori, H.J.F.; Shinibekova, A.; Kalmakhanova, M.S.; Massalimova, B.K.; Pietrobelli, J.M.T.A.; Lenzi, G.G.; et al. Assisted Hydrothermal Carbonization of Agroindustrial Byproducts as Effective Step in the Production of Activated Carbon Catalysts for Wet Peroxide Oxidation of Micro-Pollutants. *J. Environ. Chem. Eng.* **2021**, *9*, 105004. [CrossRef]
167. Liu, Z.; Zhang, F.-S.; Wu, J. Characterization and Application of Chars Produced from Pinewood Pyrolysis and Hydrothermal Treatment. *Fuel* **2010**, *89*, 510–514. [CrossRef]
168. Román-Martínez, M.C.; Cazorla-Amorós, D.; Linares-Solano, A.; De Lecea, C.S.-M.; Yamashita, H.; Anpo, M. Metal-Support Interaction in Pt/C Catalysts. Influence of the Support Surface Chemistry and the Metal Precursor. *Carbon* **1995**, *33*, 3–13. [CrossRef]
169. Ge, X.; Ge, M.; Chen, X.; Qian, C.; Liu, X.; Zhou, S. Facile Synthesis of Hydrochar Supported Copper Nanocatalyst for Ullmann CN Coupling Reaction in Water. *Mol. Catal.* **2020**, *484*, 110726. [CrossRef]
170. Chen, H.; Xu, J.; Lin, H.; Zhao, X.; Shang, J.; Liu, Z. Arsenic Removal via a Novel Hydrochar from Livestock Waste Co-Activated with Thiourea and γ-Fe_2O_3 Nanoparticles. *J. Hazard. Mater.* **2021**, *419*, 126457. [CrossRef]
171. Ma, Q.; Cui, L.; Zhou, S.; Li, Y.; Shi, W.; Ai, S. Iron Nanoparticles in Situ Encapsulated in Lignin-Derived Hydrochar as an Effective Catalyst for Phenol Removal. *Environ. Sci. Pollut. Res.* **2018**, *25*, 20833–20840. [CrossRef] [PubMed]
172. Deng, Y.; Zhang, T.; Sharma, B.K.; Nie, H. Optimization and Mechanism Studies on Cell Disruption and Phosphorus Recovery from Microalgae with Magnesium Modified Hydrochar in Assisted Hydrothermal System. *Sci. Total Environ.* **2019**, *646*, 1140–1154. [CrossRef] [PubMed]
173. Dang, M.; Chen, D.; Lu, P.; Xu, G. Enhanced Degradation of DDT Using a Novel Iron-Assisted Hydrochar Catalyst Combined with Peroxymonosulfate: Experiment and Mechanism Analysis. *Chemosphere* **2022**, *307*, 135893. [CrossRef] [PubMed]
174. Han, J.; Liang, Y.; Qin, L.; Zhao, B.; Wang, H.; Wang, Y. Ni@HC Core–Shell Structured Catalysts for Dry Reforming of Methane and Carbon Dioxide. *Catal. Lett.* **2019**, *149*, 3224–3237. [CrossRef]
175. Hu, C.; Dai, L. Doping of Carbon Materials for Metal-free Electrocatalysis. *Adv. Mater.* **2019**, *31*, 1804672. [CrossRef]
176. Yang, H.B.; Miao, J.; Hung, S.-F.; Chen, J.; Tao, H.B.; Wang, X.; Zhang, L.; Chen, R.; Gao, J.; Chen, H.M. Identification of Catalytic Sites for Oxygen Reduction and Oxygen Evolution in N-Doped Graphene Materials: Development of Highly Efficient Metal-Free Bifunctional Electrocatalyst. *Sci. Adv.* **2016**, *2*, e1501122. [CrossRef]

177. Hu, X.; Long, Y.; Fan, M.; Yuan, M.; Zhao, H.; Ma, J.; Dong, Z. Two-Dimensional Covalent Organic Frameworks as Self-Template Derived Nitrogen-Doped Carbon Nanosheets for Eco-Friendly Metal-Free Catalysis. *Appl. Catal. B Environ.* **2019**, *244*, 25–35. [CrossRef]
178. Duan, X.; Ao, Z.; Sun, H.; Indrawirawan, S.; Wang, Y.; Kang, J.; Liang, F.; Zhu, Z.H.; Wang, S. Nitrogen-Doped Graphene for Generation and Evolution of Reactive Radicals by Metal-Free Catalysis. *ACS Appl. Mater. Interfaces* **2015**, *7*, 4169–4178. [CrossRef]
179. Chen, H.; Carroll, K.C. Metal-Free Catalysis of Persulfate Activation and Organic-Pollutant Degradation by Nitrogen-Doped Graphene and Aminated Graphene. *Environ. Pollut.* **2016**, *215*, 96–102. [CrossRef]
180. Yu, J.; Zhu, Z.; Zhang, H.; Shen, X.; Qiu, Y.; Yin, D.; Wang, S. Persistent Free Radicals on N-Doped Hydrochar for Degradation of Endocrine Disrupting Compounds. *Chem. Eng. J.* **2020**, *398*, 125538. [CrossRef]
181. Qiao, M.; Meysami, S.S.; Ferrero, G.A.; Xie, F.; Meng, H.; Grobert, N.; Titirici, M.-M. Low-Cost Chitosan-Derived N-Doped Carbons Boost Electrocatalytic Activity of Multiwall Carbon Nanotubes. *Adv. Funct. Mater.* **2018**, *28*, 1707284. [CrossRef]
182. Li, S.; Ma, Q.; Chen, L.; Yang, Z.; Aqeel Kamran, M.; Chen, B. Hydrochar-Mediated Photocatalyst Fe3O4/BiOBr@HC for Highly Efficient Carbamazepine Degradation under Visible LED Light Irradiation. *Chem. Eng. J.* **2022**, *433*, 134492. [CrossRef]
183. Zhu, X.; Mao, L.; Chen, B. Driving Forces Linking Microbial Community Structure and Functions to Enhanced Carbon Stability in Biochar-Amended Soil. *Environ. Int.* **2019**, *133*, 105211. [CrossRef]
184. Sandouqa, A.; Al-Hamamre, Z.; Asfar, J. Preparation and Performance Investigation of a Lignin-Based Solid Acid Catalyst Manufactured from Olive Cake for Biodiesel Production. *Renew. Energy* **2019**, *132*, 667–682. [CrossRef]
185. Li, Y.; Zeng, D. Synthesis and Characterization of Flower-like Carbon Spheres Solid Acid from Glucose for Esterification. *Mater. Lett.* **2017**, *193*, 172–175. [CrossRef]
186. Shimin, K.; Chang, J.; Juan, F.A.N. One Step Preparation of Sulfonated Solid Catalyst and Its Effect in Esterification Reaction. *Chin. J. Chem. Eng.* **2014**, *22*, 392–397.
187. Qin, L.; Mao, H.; Lei, C.; Wang, Q.; Gao, Z. The SO_3H-Functionalized Carbonaceous@montmorillonite Efficient Heterogeneous Catalyst for Synthesis of Trimethylolpropane from Long-Chain Fatty Acid. *Microporous Mesoporous Mater.* **2019**, *289*, 109623. [CrossRef]
188. Araujo, R.O.; Santos, V.O.; Ribeiro, F.C.P.; Chaar, J. da S.; Falcão, N.P.S.; de Souza, L.K.C. One-Step Synthesis of a Heterogeneous Catalyst by the Hydrothermal Carbonization of Acai Seed. *Reac Kinet Mech Cat* **2021**, *134*, 199–220. [CrossRef]
189. Ibrahim, S.F.; Asikin-Mijan, N.; Ibrahim, M.L.; Abdulkareem-Alsultan, G.; Izham, S.M.; Taufiq-Yap, Y.H. Sulfonated Functionalization of Carbon Derived Corncob Residue via Hydrothermal Synthesis Route for Esterification of Palm Fatty Acid Distillate. *Energy Convers. Manag.* **2020**, *210*, 112698. [CrossRef]
190. Zhang, S.; Sheng, K.; Liang, Y.; Liu, J.; E, S.; Zhang, X. Green Synthesis of Aluminum-Hydrochar for the Selective Isomerization of Glucose to Fructose. *Sci. Total Environ.* **2020**, *727*, 138743. [CrossRef]
191. Chen, Y.; Ai, X.; Huang, B.; Huang, M.; Huang, Y.; Lu, Y. Consecutive Preparation of Hydrochar Catalyst Functionalized in Situ with Sulfonic Groups for Efficient Cellulose Hydrolysis. *Cellulose* **2017**, *24*, 2743–2752. [CrossRef]
192. Yang, J.; Zhang, H.; Ao, Z.; Zhang, S. Hydrothermal Carbon Enriched with Sulfonic and Carboxyl Groups as an Efficient Solid Acid Catalyst for Butanolysis of Furfuryl Alcohol. *Catal. Commun.* **2019**, *123*, 109–113. [CrossRef]
193. Zhang, Y.-L.; Li, J.-L.; Zhao, L.; Sui, X.-L.; Zhou, Q.-Y.; Gong, X.-F.; Cai, J.-J.; Li, J.-Z.; Gu, D.-M.; Wang, Z.-B. Nitrogen Doped Carbon Coated Mo Modified TiO_2 Nanowires (NC@MTNWs-FI) with Functionalized Interfacial as Advanced PtRu Catalyst Support for Methanol Electrooxidation. *Electrochim. Acta* **2020**, *331*, 135410. [CrossRef]
194. Pirsaheb, M.; Moradi, S.; Shahlaei, M.; Farhadian, N. Application of Carbon Dots as Efficient Catalyst for the Green Oxidation of Phenol: Kinetic Study of the Degradation and Optimization Using Response Surface Methodology. *J. Hazard. Mater.* **2018**, *353*, 444–453. [CrossRef]
195. Gai, C.; Zhang, F.; Yang, T.; Liu, Z.; Jiao, W.; Peng, N.; Liu, T.; Lang, Q.; Xia, Y. Hydrochar Supported Bimetallic Ni–Fe Nanocatalysts with Tailored Composition, Size and Shape for Improved Biomass Steam Reforming Performance. *Green Chem.* **2018**, *20*, 2788–2800. [CrossRef]
196. Liu, Z.; Liu, Z. Comparison of Hydrochar- and Pyrochar-Based Solid Acid Catalysts from Cornstalk: Physiochemical Properties, Catalytic Activity and Deactivation Behavior. *Bioresour. Technol.* **2020**, *297*, 122477. [CrossRef] [PubMed]
197. Yabalak, E.; Elneccar, F. Evaluation of Watermelon Peel, Banana Peel and Bay Leaves Hydrochars as Green Catalysts in the Degradation of Malachite Green by Thermally Activated Persulfate Oxidation Method. *J. Environ. Manag.* **2022**, *304*, 114311. [CrossRef]
198. Zhuang, X.; Liu, J.; Ma, L. Facile Synthesis of Hydrochar-Supported Catalysts from Glucose and Its Catalytic Activity towards the Production of Functional Amines. *Green Energy Environ.* **2022**, *in press*. [CrossRef]
199. Lin, Q.; Zhang, S.; Wang, J.; Yin, H. Synthesis of Modified Char-Supported Ni–Fe Catalyst with Hierarchical Structure for Catalytic Cracking of Biomass Tar. *Renew. Energy* **2021**, *174*, 188–198. [CrossRef]
200. Ababneh, H.; Hameed, B.H. Chitosan-Derived Hydrothermally Carbonized Materials and Its Applications: A Review of Recent Literature. *Int. J. Biol. Macromol.* **2021**, *186*, 314–327. [CrossRef]
201. Winter, M.; Brodd, R.J. What Are Batteries, Fuel Cells, and Supercapacitors? *Chem. Rev.* **2004**, *104*, 4245–4270. [CrossRef] [PubMed]
202. Masoumi, S.; Borugadda, V.B.; Nanda, S.; Dalai, A.K. Hydrochar: A Review on Its Production Technologies and Applications. *Catalysts* **2021**, *11*, 939. [CrossRef]

203. Li, H.; Shi, F.; An, Q.; Zhai, S.; Wang, K.; Tong, Y. Three-Dimensional Hierarchical Porous Carbon Derived from Lignin for Supercapacitors: Insight into the Hydrothermal Carbonization and Activation. *Int. J. Biol. Macromol.* **2021**, *166*, 923–933. [CrossRef] [PubMed]
204. Wu, Y.; Cao, J.-P.; Zhao, X.-Y.; Zhuang, Q.-Q.; Zhou, Z.; Huang, Y.; Wei, X.-Y. High-Performance Electrode Material for Electric Double-Layer Capacitor Based on Hydrothermal Pre-Treatment of Lignin by $ZnCl_2$. *Appl. Surf. Sci.* **2020**, *508*, 144536. [CrossRef]
205. Fan, Y.; Liu, P.-F.; Huang, Z.-Y.; Jiang, T.-W.; Yao, K.-L.; Han, R. Porous Hollow Carbon Spheres for Electrode Material of Supercapacitors and Support Material of Dendritic Pt Electrocatalyst. *J. Power Sources* **2015**, *280*, 30–38. [CrossRef]
206. Li, K.; Luo, J.; Wei, M.; Yao, X.; Feng, Q.; Ma, X.; Liu, Z. Functional Porous Carbon Derived from Waste Eucalyptus Bark for Toluene Adsorption and Aqueous Symmetric Supercapacitors. *Diam. Relat. Mater.* **2022**, *127*, 109196. [CrossRef]
207. Liu, F.; Gao, Y.; Zhang, C.; Huang, H.; Yan, C.; Chu, X.; Xu, Z.; Wang, Z.; Zhang, H.; Xiao, X.; et al. Highly Microporous Carbon with Nitrogen-Doping Derived from Natural Biowaste for High-Performance Flexible Solid-State Supercapacitor. *J. Colloid Interface Sci.* **2019**, *548*, 322–332. [CrossRef]
208. Feng, C. Incorporation of MnO2 into Egg Yolk Derived P, N, O-Tridoped Carbon for Supercapacitors with Excellent Cycling Stability. *Int. J. Electrochem. Sci.* **2019**, 8284–8295. [CrossRef]
209. Xu, Z.; Zhang, X.; Li, K.; Lin, H.; Qian, X.; Sheng, K. Green Synthesis of Fe-Decorated Carbon Sphere/Nanosheet Derived from Bamboo for High-Performance Supercapacitor Application. *Energy Fuels* **2020**, *35*, 827–838. [CrossRef]
210. Arenas Esteban, D.; Guerrero Martínez, A.; Carretero González, J.; Birss, V.I.; Otero-Díaz, L.C.; Ávila Brande, D. Tunable Supercapacitor Materials Derived from Hydrochar/Gold Nanograpes. *ACS Appl. Energy Mater.* **2020**, *3*, 9348–9359. [CrossRef]
211. Agegnehu, G.; Srivastava, A.K.; Bird, M.I. The Role of Biochar and Biochar-Compost in Improving Soil Quality and Crop Performance: A Review. *Appl. Soil Ecol.* **2017**, *119*, 156–170. [CrossRef]
212. Busch, D.; Glaser, B. Stability of Co-Composted Hydrochar and Biochar under Field Conditions in a Temperate Soil. *Soil Use Manag.* **2015**, *31*, 251–258. [CrossRef]
213. Fang, J.; Zhan, L.; Ok, Y.S.; Gao, B. Minireview of Potential Applications of Hydrochar Derived from Hydrothermal Carbonization of Biomass. *J. Ind. Eng. Chem.* **2018**, *57*, 15–21. [CrossRef]
214. Fornes, F.; Belda, R.M.; Lidón, A. Analysis of Two Biochars and One Hydrochar from Different Feedstock: Focus Set on Environmental, Nutritional and Horticultural Considerations. *J. Clean. Prod.* **2015**, *86*, 40–48. [CrossRef]
215. Paneque, M.; Knicker, H.; Kern, J.; Rosa, J.M.D. la Hydrothermal Carbonization and Pyrolysis of Sewage Sludge: Effects on Lolium Perenne Germination and Growth. *Agronomy* **2019**, *9*, 363. [CrossRef]
216. Schimmelpfennig, S.; Kammann, C.; Moser, G.; Grünhage, L.; Müller, C. Changes in Macro- and Micronutrient Contents of Grasses and Forbs Following *Miscanthus* × *giganteus* feedstock, Hydrochar and Biochar Application to Temperate Grassland. *Grass Forage Sci.* **2015**, *70*, 582–599. [CrossRef]
217. Scheifele, M.; Hobi, A.; Buegger, F.; Gattinger, A.; Schulin, R.; Boller, T.; Mäder, P. Impact of Pyrochar and Hydrochar on Soybean (*Glycine max* L.) Root Nodulation and Biological Nitrogen Fixation. *J. Plant Nutr. Soil Sci.* **2017**, *180*, 199–211. [CrossRef]
218. Wagner, A.; Kaupenjohann, M. Suitability of Biochars (Pyro- and Hydrochars) for Metal Immobilization on Former Sewage-Field Soils. *Eur. J. Soil Sci.* **2013**, *65*, 139–148. [CrossRef]
219. Bargmann, I.; Rillig, M.C.; Kruse, A.; Greef, J.-M.; Kücke, M. Effects of Hydrochar Application on the Dynamics of Soluble Nitrogen in Soils and on Plant Availability. *J. Plant Nutr. Soil Sci.* **2013**, *177*, 48–58. [CrossRef]
220. Bento, L.R.; Melo, C.A.; Ferreira, O.P.; Moreira, A.B.; Mounier, S.; Piccolo, A.; Spaccini, R.; Bisinoti, M.C. Humic Extracts of Hydrochar and Amazonian Dark Earth: Molecular Characteristics and Effects on Maize Seed Germination. *Sci. Total Environ.* **2020**, *708*, 135000. [CrossRef]
221. Abel, S.; Peters, A.; Trinks, S.; Schonsky, H.; Facklam, M.; Wessolek, G. Impact of Biochar and Hydrochar Addition on Water Retention and Water Repellency of Sandy Soil. *Geoderma* **2013**, *202–203*, 183–191. [CrossRef]
222. Mau, V.; Arye, G.; Gross, A. Poultry Litter Hydrochar as an Amendment for Sandy Soils. *J. Environ. Manag.* **2020**, *271*, 110959. [CrossRef] [PubMed]
223. Kalderis, D.; Papameletiou, G.; Kayan, B. Assessment of Orange Peel Hydrochar as a Soil Amendment: Impact on Clay Soil Physical Properties and Potential Phytotoxicity. *Waste Biomass Valorization* **2018**, *10*, 3471–3484. [CrossRef]
224. He, C.; Giannis, A.; Wang, J.-Y. Conversion of Sewage Sludge to Clean Solid Fuel Using Hydrothermal Carbonization: Hydrochar Fuel Characteristics and Combustion Behavior. *Appl. Energy* **2013**, *111*, 257–266. [CrossRef]
225. Fang, Q.; Chen, B.; Lin, Y.; Guan, Y. Aromatic and Hydrophobic Surfaces of Wood-Derived Biochar Enhance Perchlorate Adsorption via Hydrogen Bonding to Oxygen-Containing Organic Groups. *Environ. Sci. Technol.* **2013**, *48*, 279–288. [CrossRef]
226. Neina, D. The Role of Soil PH in Plant Nutrition and Soil Remediation. *Appl. Environ. Soil Sci.* **2019**, *2019*, 1–9. [CrossRef]
227. Libra, J.A.; Ro, K.S.; Kammann, C.; Funke, A.; Berge, N.D.; Neubauer, Y.; Titirici, M.-M.; Fühner, C.; Bens, O.; Kern, J.; et al. Hydrothermal Carbonization of Biomass Residuals: A Comparative Review of the Chemistry, Processes and Applications of Wet and Dry Pyrolysis. *Biofuels* **2011**, *2*, 71–106. [CrossRef]
228. Saha, N.; Saba, A.; Reza, M.T. Effect of Hydrothermal Carbonization Temperature on PH, Dissociation Constants, and Acidic Functional Groups on Hydrochar from Cellulose and Wood. *J. Anal. Appl. Pyrolysis* **2019**, *137*, 138–145. [CrossRef]
229. Ren, J.; Wang, F.; Zhai, Y.; Zhu, Y.; Peng, C.; Wang, T.; Li, C.; Zeng, G. Effect of Sewage Sludge Hydrochar on Soil Properties and Cd Immobilization in a Contaminated Soil. *Chemosphere* **2017**, *189*, 627–633. [CrossRef]

230. Belda, R.M.; Lidón, A.; Fornes, F. Biochars and Hydrochars as Substrate Constituents for Soilless Growth of Myrtle and Mastic. *Ind. Crops Prod.* **2016**, *94*, 132–142. [CrossRef]
231. Röhrdanz, M.; Rebling, T.; Ohlert, J.; Jasper, J.; Greve, T.; Buchwald, R.; von Frieling, P.; Wark, M. Hydrothermal Carbonization of Biomass from Landscape Management – Influence of Process Parameters on Soil Properties of Hydrochars. *J. Environ. Manag.* **2016**, *173*, 72–78. [CrossRef] [PubMed]
232. Rillig, M.C.; Wagner, M.; Salem, M.; Antunes, P.M.; George, C.; Ramke, H.-G.; Titirici, M.-M.; Antonietti, M. Material Derived from Hydrothermal Carbonization: Effects on Plant Growth and Arbuscular Mycorrhiza. *Appl. Soil Ecol.* **2010**, *45*, 238–242. [CrossRef]
233. Álvarez, M.L.; Gascó, G.; Plaza, C.; Paz-Ferreiro, J.; Méndez, A. Hydrochars from Biosolids and Urban Wastes as Substitute Materials for Peat. *Land Degrad. Dev.* **2017**, *28*, 2268–2276. [CrossRef]
234. Andert, J.; Mumme, J. Impact of Pyrolysis and Hydrothermal Biochar on Gas-Emitting Activity of Soil Microorganisms and Bacterial and Archaeal Community Composition. *Appl. Soil Ecol.* **2015**, *96*, 225–239. [CrossRef]
235. Eskandari, S.; Mohammadi, A.; Sandberg, M.; Eckstein, R.L.; Hedberg, K.; Granström, K. Hydrochar-Amended Substrates for Production of Containerized Pine Tree Seedlings under Different Fertilization Regimes. *Agronomy* **2019**, *9*, 350. [CrossRef]
236. George, C.; Wagner, M.; Kücke, M.; Rillig, M.C. Divergent Consequences of Hydrochar in the Plant–Soil System: Arbuscular Mycorrhiza, Nodulation, Plant Growth and Soil Aggregation Effects. *Appl. Soil Ecol.* **2012**, *59*, 68–72. [CrossRef]
237. Fuertes, A.B.; Arbestain, M.C.; Sevilla, M.; Maciá-Agulló, J.A.; Fiol, S.; López, R.; Smernik, R.J.; Aitkenhead, W.P.; Arce, F.; Macías, F. Chemical and Structural Properties of Carbonaceous Products Obtained by Pyrolysis and Hydrothermal Carbonisation of Corn Stover. *Soil Res.* **2010**, *48*, 618. [CrossRef]
238. Hu, B.; Wang, K.; Wu, L.; Yu, S.-H.; Antonietti, M.; Titirici, M.-M. Engineering Carbon Materials from the Hydrothermal Carbonization Process of Biomass. *Adv. Mater.* **2010**, *22*, 813–828. [CrossRef]
239. Eibisch, N.; Helfrich, M.; Don, A.; Mikutta, R.; Kruse, A.; Ellerbrock, R.; Flessa, H. Properties and Degradability of Hydrothermal Carbonization Products. *J. Environ. Qual.* **2013**, *42*, 1565–1573. [CrossRef]
240. Schulze, M.; Mumme, J.; Funke, A.; Kern, J. Effects of Selected Process Conditions on the Stability of Hydrochar in Low-Carbon Sandy Soil. *Geoderma* **2016**, *267*, 137–145. [CrossRef]
241. George, E.; Ventura, M.; Panzacchi, P.; Scandellari, F.; Tonon, G. Can Hydrochar and Pyrochar Affect Nitrogen Uptake and Biomass Allocation in Poplars? *J. Plant Nutr. Soil Sci.* **2017**, *180*, 178–186. [CrossRef]
242. Baronti, S.; Alberti, G.; Camin, F.; Criscuoli, I.; Genesio, L.; Mass, R.; Vaccari, F.P.; Ziller, L.; Miglietta, F. Hydrochar Enhances Growth of Poplar for Bioenergy While Marginally Contributing to Direct Soil Carbon Sequestration. *GCB Bioenergy* **2017**, *9*, 1618–1626. [CrossRef]
243. Kammann, C.; Ratering, S.; Eckhard, C.; Müller, C. Biochar and Hydrochar Effects on Greenhouse Gas (Carbon Dioxide, Nitrous Oxide, and Methane) Fluxes from Soils. *J. Environ. Qual.* **2012**, *41*, 1052–1066. [CrossRef]
244. Hou, P.; Feng, Y.; Wang, N.; Petropoulos, E.; Li, D.; Yu, S.; Xue, L.; Yang, L. Win-Win: Application of Sawdust-Derived Hydrochar in Low Fertility Soil Improves Rice Yield and Reduces Greenhouse Gas Emissions from Agricultural Ecosystems. *Sci. Total Environ.* **2020**, *748*, 142457. [CrossRef] [PubMed]
245. Yu, S.; Feng, Y.; Xue, L.; Sun, H.; Han, L.; Yang, L.; Sun, Q.; Chu, Q. Biowaste to Treasure: Application of Microbial-Aged Hydrochar in Rice Paddy Could Improve Nitrogen Use Efficiency and Rice Grain Free Amino Acids. *J. Clean. Prod.* **2019**, *240*, 118180. [CrossRef]
246. Adjuik, T.; Rodjom, A.M.; Miller, K.E.; Reza, M.T.M.; Davis, S.C. Application of Hydrochar, Digestate, and Synthetic Fertilizer to a Miscanthus × Giganteus Crop: Implications for Biomass and Greenhouse Gas Emissions. *Appl. Sci.* **2020**, *10*, 8953. [CrossRef]
247. Naisse, C.; Girardin, C.; Lefevre, R.; Pozzi, A.; Maas, R.; Stark, A.; Rumpel, C. Effect of Physical Weathering on the Carbon Sequestration Potential of Biochars and Hydrochars in Soil. *GCB Bioenergy* **2014**, *7*, 488–496. [CrossRef]
248. Schimmelpfennig, S.; Müller, C.; Grünhage, L.; Koch, C.; Kammann, C. Biochar, Hydrochar and Uncarbonized Feedstock Application to Permanent Grassland—Effects on Greenhouse Gas Emissions and Plant Growth. *Agric. Ecosyst. Environ.* **2014**, *191*, 39–52. [CrossRef]
249. Breulmann, M.; Kuka, K.; van Afferden, M.; Buscot, F.; Fühner, C.; Müller, R.; Schulz, E. Labile Water Soluble Components Govern the Short-Term Microbial Decay of Hydrochar from Sewage Sludge. *Arch. Agron. Soil Sci.* **2017**, *64*, 873–880. [CrossRef]
250. Edo, M. *Hydrothermal Carbonization (HTC): Valorisation of Organic Waste and Sewage Sludges for Hydrochar Production and Biofertilizers*; IEA: Paris, France, 2021.
251. WHITE, P.J. Calcium in Plants. *Ann. Bot.* **2003**, *92*, 487–511. [CrossRef]
252. Subbarao, G.V.; Ito, O.; Berry, W.L.; Wheeler, R.M. Sodium—A Functional Plant Nutrient. *Crit. Rev. Plant Sci.* **2003**, *22*, 391–416. [CrossRef]
253. Idowu, I.; Li, L.; Flora, J.R.V.; Pellechia, P.J.; Darko, S.A.; Ro, K.S.; Berge, N.D. Hydrothermal Carbonization of Food Waste for Nutrient Recovery and Reuse. *Waste Manag.* **2017**, *69*, 480–491. [CrossRef] [PubMed]
254. Aragón-Briceño, C.I.; Pozarlik, A.K.; Bramer, E.A.; Niedzwiecki, L.; Pawlak-Kruczek, H.; Brem, G. Hydrothermal Carbonization of Wet Biomass from Nitrogen and Phosphorus Approach: A Review. *Renew. Energy* **2021**, *171*, 401–415. [CrossRef]
255. Falk, J.; Skoglund, N.; Grimm, A.; Öhman, M. Fate of Phosphorus in Fixed Bed Combustion of Biomass and Sewage Sludge. *Energy Fuels* **2020**, *34*, 4587–4594. [CrossRef]
256. Dima, S.S.; Arnob, A.; Salma, U.; Kabir, K.B.; Kirtania, K. Fate of Nutrients during Hydrothermal Carbonization of Biogenic Municipal Waste. *Biomass Convers. Biorefinery* **2020**, *12*, 71–80. [CrossRef]

257. Liu, H.; Basar, I.A.; Nzihou, A.; Eskicioglu, C. Hydrochar Derived from Municipal Sludge through Hydrothermal Processing: A Critical Review on Its Formation, Characterization, and Valorization. *Water Res.* **2021**, *199*, 117186. [CrossRef]
258. Vaneeckhaute, C.; Meers, E.; Michels, E.; Christiaens, P.; Tack, F.M.G. Fate of Macronutrients in Water Treatment of Digestate Using Vibrating Reversed Osmosis. *Water Air Soil Pollut.* **2011**, *223*, 1593–1603. [CrossRef]
259. Vaneeckhaute, C.; Lebuf, V.; Michels, E.; Belia, E.; Vanrolleghem, P.A.; Tack, F.M.G.; Meers, E. Nutrient Recovery from Digestate: Systematic Technology Review and Product Classification. *Waste Biomass Valorization* **2016**, *8*, 21–40. [CrossRef]
260. Malhotra, M.; Garg, A. Hydrothermal Carbonization of Centrifuged Sewage Sludge: Determination of Resource Recovery from Liquid Fraction and Thermal Behaviour of Hydrochar. *Waste Manag.* **2020**, *117*, 114–123. [CrossRef]
261. Di Capua, F.; de Sario, S.; Ferraro, A.; Petrella, A.; Race, M.; Pirozzi, F.; Fratino, U.; Spasiano, D. Phosphorous Removal and Recovery from Urban Wastewater: Current Practices and New Directions. *Sci. Total Environ.* **2022**, *823*, 153750. [CrossRef]
262. Azam, H.M.; Alam, S.T.; Hasan, M.; Yameogo, D.D.S.; Kannan, A.D.; Rahman, A.; Kwon, M.J. Phosphorous in the Environment: Characteristics with Distribution and Effects, Removal Mechanisms, Treatment Technologies, and Factors Affecting Recovery as Minerals in Natural and Engineered Systems. *Environ. Sci. Pollut. Res.* **2019**, *26*, 20183–20207. [CrossRef] [PubMed]
263. Nobaharan, K.; Bagheri Novair, S.; Asgari Lajayer, B.; van Hullebusch, E. Phosphorus Removal from Wastewater: The Potential Use of Biochar and the Key Controlling Factors. *Water* **2021**, *13*, 517. [CrossRef]
264. Eriksson, O.; Carlsson Reich, M.; Frostell, B.; Björklund, A.; Assefa, G.; Sundqvist, J.-O.; Granath, J.; Baky, A.; Thyselius, L. Municipal Solid Waste Management from a Systems Perspective. *J. Clean. Prod.* **2005**, *13*, 241–252. [CrossRef]
265. Sarrion, A.; Diaz, E.; de la Rubia, M.A.; Mohedano, A.F. Fate of Nutrients during Hydrothermal Treatment of Food Waste. *Bioresour. Technol.* **2021**, *342*, 125954. [CrossRef] [PubMed]
266. Reza, M.T.; Freitas, A.; Yang, X.; Hiibel, S.; Lin, H.; Coronella, C.J. Hydrothermal Carbonization (HTC) of Cow Manure: Carbon and Nitrogen Distributions in HTC Products. *Environ. Prog. Sustain. Energy* **2016**, *35*, 1002–1011. [CrossRef]
267. Liu, T.; Guo, Y.; Peng, N.; Lang, Q.; Xia, Y.; Gai, C.; Liu, Z. Nitrogen Transformation among Char, Tar and Gas during Pyrolysis of Sewage Sludge and Corresponding Hydrochar. *J. Anal. Appl. Pyrolysis* **2017**, *126*, 298–306. [CrossRef]
268. Alhnidi, M.-J.; Wüst, D.; Funke, A.; Hang, L.; Kruse, A. Fate of Nitrogen, Phosphate, and Potassium during Hydrothermal Carbonization and the Potential for Nutrient Recovery. *ACS Sustain. Chem. Eng.* **2020**, *8*, 15507–15516. [CrossRef]
269. Zhang, Q.; Liu, H.; Li, W.; Xu, J.; Liang, Q. Behavior of Phosphorus during Co-Gasification of Sewage Sludge and Coal. *Energy Fuels* **2012**, *26*, 2830–2836. [CrossRef]
270. Dieguez-Alonso, A.; Funke, A.; Anca-Couce, A.; Rombolà, A.; Ojeda, G.; Bachmann, J.; Behrendt, F. Towards Biochar and Hydrochar Engineering—Influence of Process Conditions on Surface Physical and Chemical Properties, Thermal Stability, Nutrient Availability, Toxicity and Wettability. *Energies* **2018**, *11*, 496. [CrossRef]
271. Chrispim, M.C.; Scholz, M.; Nolasco, M.A. Phosphorus Recovery from Municipal Wastewater Treatment: Critical Review of Challenges and Opportunities for Developing Countries. *J. Environ. Manag.* **2019**, *248*, 109268. [CrossRef]
272. Sultana, A.I.; Reza, M.T. Techno-Economic Assessment of Superactivated Hydrochar Production by KOH Impregnation Compared to Direct Chemical Activation. *Biomass Conv. Bioref.* **2022**, 1–13. [CrossRef]
273. Zhao, X.; Becker, G.C.; Faweya, N.; Rodriguez Correa, C.; Yang, S.; Xie, X.; Kruse, A. Fertilizer and Activated Carbon Production by Hydrothermal Carbonization of Digestate. *Biomass Convers. Biorefinery* **2017**, *8*, 423–436. [CrossRef]
274. Zhu, N.; Yan, T.; Qiao, J.; Cao, H. Adsorption of Arsenic, Phosphorus and Chromium by Bismuth Impregnated Biochar: Adsorption Mechanism and Depleted Adsorbent Utilization. *Chemosphere* **2016**, *164*, 32–40. [CrossRef] [PubMed]
275. He, H.; Zhang, N.; Chen, N.; Lei, Z.; Shimizu, K.; Zhang, Z. Efficient Phosphate Removal from Wastewater by MgAl-LDHs Modified Hydrochar Derived from Tobacco Stalk. *Bioresour. Technol. Rep.* **2019**, *8*, 100348. [CrossRef]
276. Hachiya, T.; Sakakibara, H. Interactions between Nitrate and Ammonium in Their Uptake, Allocation, Assimilation, and Signaling in Plants. *J. Exp. Bot.* **2016**, erw449. [CrossRef]
277. Schachtman, D.; Reid, R.; Ayling, S. Phosphorus Uptake by Plants: From Soil to Cell. *Plant Physiol* **1998**, *116*, 447–453. [CrossRef]
278. Lorick, D.; Macura, B.; Ahlström, M.; Grimvall, A.; Harder, R. Effectiveness of Struvite Precipitation and Ammonia Stripping for Recovery of Phosphorus and Nitrogen from Anaerobic Digestate: A Systematic Review. *Environ. Evid.* **2020**, *9*. [CrossRef]
279. Siciliano, A.; Limonti, C.; Curcio, G.M.; Molinari, R. Advances in Struvite Precipitation Technologies for Nutrients Removal and Recovery from Aqueous Waste and Wastewater. *Sustainability* **2020**, *12*, 7538. [CrossRef]
280. Stutzenstein, P.; Bacher, M.; Rosenau, T.; Pfeifer, C. Optimization of Nutrient and Carbon Recovery from Anaerobic Digestate via Hydrothermal Carbonization and Investigation of the Influence of the Process Parameters. *Waste Biomass Valorization* **2017**, *9*, 1303–1318. [CrossRef]
281. Fei, Y.; Zhao, D.; Liu, Y.; Zhang, W.; Tang, Y.; Huang, X.; Wu, Q.; Wang, Y.; Xiao, T.; Liu, C. Feasibility of Sewage Sludge Derived Hydrochars for Agricultural Application: Nutrients (N, P, K) and Potentially Toxic Elements (Zn, Cu, Pb, Ni, Cd). *Chemosphere* **2019**, *236*, 124841. [CrossRef]
282. Kavitha, B.; Reddy, P.V.L.; Kim, B.; Lee, S.S.; Pandey, S.K.; Kim, K.-H. Benefits and Limitations of Biochar Amendment in Agricultural Soils: A Review. *J. Environ. Manag.* **2018**, *227*, 146–154. [CrossRef]
283. Saddawi, A.; Jones, J.M.; Williams, A.; Le Coeur, C. Commodity Fuels from Biomass through Pretreatment and Torrefaction: Effects of Mineral Content on Torrefied Fuel Characteristics and Quality. *Energy Fuels* **2012**, *26*, 6466–6474. [CrossRef]
284. Vassilev, S.V.; Baxter, D.; Andersen, L.K.; Vassileva, C.G.; Morgan, T.J. An Overview of the Organic and Inorganic Phase Composition of Biomass. *Fuel* **2012**, *94*, 1–33. [CrossRef]

285. Fei, Y.; Zhao, D.; Cao, Y.; Huot, H.; Tang, Y.; Zhang, H.; Xiao, T. Phosphorous Retention and Release by Sludge-Derived Hydrochar for Potential Use as a Soil Amendment. *J. Environ. Qual.* **2019**, *48*, 502–509. [CrossRef] [PubMed]
286. Pérez, C.; Boily, J.-F.; Jansson, S.; Gustafsson, T.; Fick, J. Acid-Induced Phosphorus Release from Hydrothermally Carbonized Sewage Sludge. *Waste Biomass Valorization* **2021**, *12*, 6555–6568. [CrossRef]
287. Shettigondahalli Ekanthalu, V.; Narra, S.; Ender, T.; Antwi, E.; Nelles, M. Influence of Post- and Pre-Acid Treatment during Hydrothermal Carbonization of Sewage Sludge on P-Transformation and the Characteristics of Hydrochar. *Processes* **2022**, *10*, 151. [CrossRef]
288. Takaya, C.A.; Fletcher, L.A.; Singh, S.; Anyikude, K.U.; Ross, A.B. Phosphate and Ammonium Sorption Capacity of Biochar and Hydrochar from Different Wastes. *Chemosphere* **2016**, *145*, 518–527. [CrossRef]
289. Wang, B.; Lehmann, J.; Hanley, K.; Hestrin, R.; Enders, A. Adsorption and Desorption of Ammonium by Maple Wood Biochar as a Function of Oxidation and PH. *Chemosphere* **2015**, *138*, 120–126. [CrossRef] [PubMed]